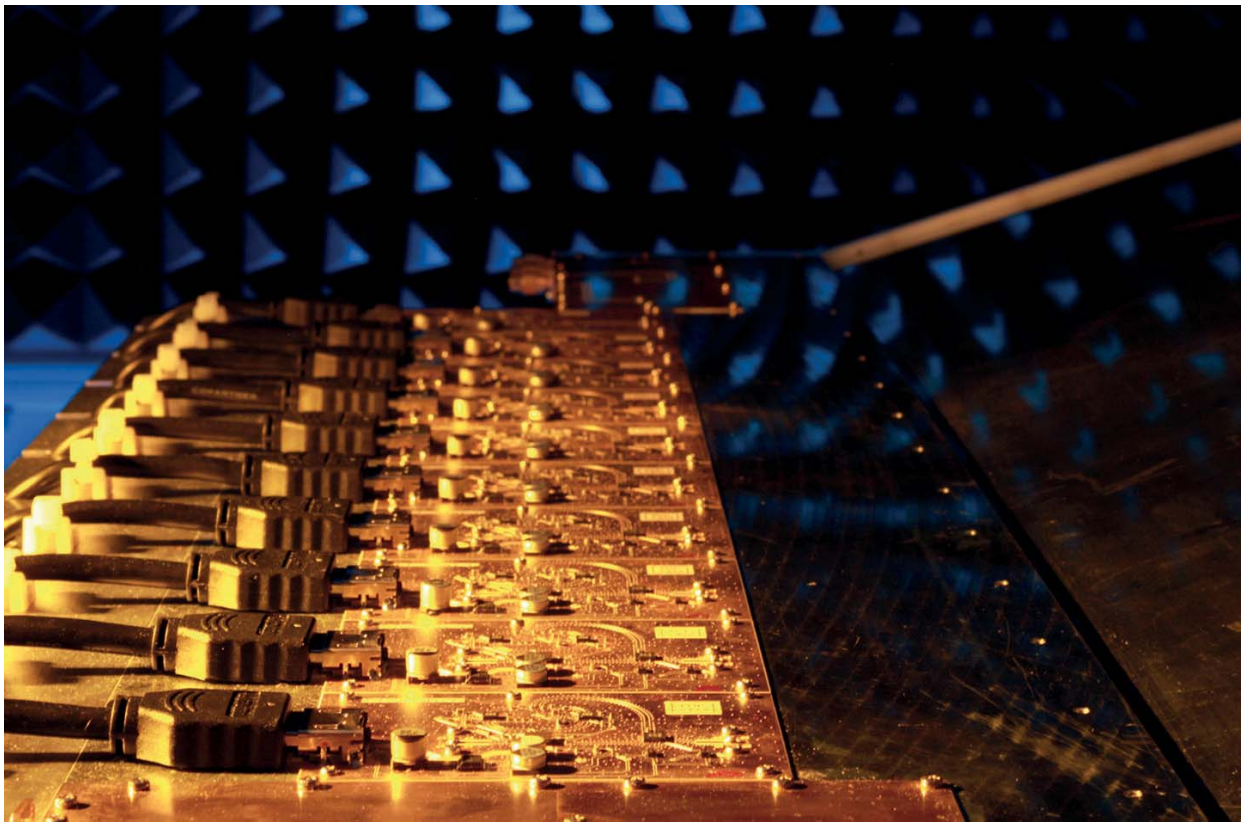
Fraunhofer FHR

FRAUNHOFER-INSTITUT FÜR HOCHFREQUENZPHYSIK UND RADARTECHNIK FHR

Mariano Pamies

An active electronically scanned Array Antenna Demonstrator with a novel RF feeding Network Concept



FRAUNHOFER VERLAG

Fraunhofer-Institut für
Hochfrequenzphysik und Radartechnik FHR

Mariano Pamies

An active electronically scanned Array Antenna Demonstrator with a novel RF feeding Network Concept

FRAUNHOFER VERLAG

Kontaktadresse:
Fraunhofer-Institut für Hochfrequenzphysik und Radartechnik FHR
Fraunhoferstraße 20
53343 Wachtberg
Telefon +49 (0)228 9435-227
Telefax +49 (0)228 9435-627
E-Mail info@fhr.fraunhofer.de
URL www.fhr.fraunhofer.de

Bibliografische Information der Deutschen Nationalbibliothek
Die Deutsche Nationalbibliothek verzeichnet diese Publikation in der Deutschen Nationalbibliografie; detaillierte bibliografische Daten sind im Internet über http://dnb.d-nb.de abrufbar.
ISBN (Print): 978-3-8396-1219-4

D 467

Zugl.: Siegen, Univ., Diss., 2016

Druck: Mediendienstleistungen des
Fraunhofer-Informationszentrum Raum und Bau IRB, Stuttgart

Für den Druck des Buches wurde chlor- und säurefreies Papier verwendet.

© by FRAUNHOFER VERLAG, 2017
Fraunhofer-Informationszentrum Raum und Bau IRB
Postfach 80 04 69, 70504 Stuttgart
Nobelstraße 12, 70569 Stuttgart
Telefon 07 11 9 70-25 00
Telefax 07 11 9 70-25 08
E-Mail verlag@fraunhofer.de
URL http://verlag.fraunhofer.de

Alle Rechte vorbehalten

Dieses Werk ist einschließlich aller seiner Teile urheberrechtlich geschützt. Jede Verwertung, die über die engen Grenzen des Urheberrechtsgesetzes hinausgeht, ist ohne schriftliche Zustimmung des Verlages unzulässig und strafbar. Dies gilt insbesondere für Vervielfältigungen, Übersetzungen, Mikroverfilmungen sowie die Speicherung in elektronischen Systemen.
Die Wiedergabe von Warenbezeichnungen und Handelsnamen in diesem Buch berechtigt nicht zu der Annahme, dass solche Bezeichnungen im Sinne der Warenzeichen- und Markenschutz-Gesetzgebung als frei zu betrachten wären und deshalb von jedermann benutzt werden dürften. Soweit in diesem Werk direkt oder indirekt auf Gesetze, Vorschriften oder Richtlinien (z.B. DIN, VDI) Bezug genommen oder aus ihnen zitiert worden ist, kann der Verlag keine Gewähr für Richtigkeit, Vollständigkeit oder Aktualität übernehmen.

An active electronically scanned array antenna demonstrator with a novel RF feeding network concept

DISSERTATION

zur Erlangung des Grades eines Doktors

der Ingenieurwissenschaften

vorgelegt von

Dipl.-Ing. M. J. Pamies Porras

eingereicht bei der Naturwissenschaftlich-Technischen Fakultät
der Universität Siegen
Siegen 2015

Erster Gutachter:	Prof. Dr.-Ing. Haring-Bolívar
Zweiter Gutachter:	Prof. Dr.-Ing. Ender
Tag der mündlichen Prüfung:	16.08.2016

a Claudia

Abstract

The main objective of this work is the development of an Active Electronically Scanned Array (AESA) antenna for civil applications. AESA technology has indeed been applied in a wide range of fields; however, it has been restricted to high-end and military markets, mostly because of its high overall costs. The technical and scientific challenges posed to the development of such antennas for civil applications are investigated in this dissertation.

The research in this work is conducted to fulfil the regulatory requirements of civil maritime radar navigation. An AESA antenna whose single active antenna element supports mixed signal operation (analogue and digital) allows the solution of the additional challenges posed by this regulation. In order to satisfy the requirements with lower costs, a full-custom mixed-signal SiGe integrated-circuit has been designed (H. Erkens et alii, 2009). Moreover, aiming at cost reductions, an innovative RF feeding network operation (T. Bertuch, 2007) and a plain antenna aperture concept (B. Tomasic et alii, 1988, M. Pamies et alii, 2010) are proposed. The aperture concept resembles existing navigation radar antennas, and it can be produced with an inexpensive extrusion process. The RF feeding networks novelty lies in the lack of isolation mechanisms between the RF ports, leading to highly coupled ports, which is accomplished by a new operating technique.

Many issues, however, remain open. The most relevant ones are the internal reflections inside the feeding network, and the highly distorted single-element patterns. Both problems come from the coupled network ports. The internal reflections inside the feeding network cannot be avoided. However, numerical models demonstrate that they have a marginal impact on the phased array radiation pattern when the reflection coefficient of the T/R (Transmit/ Receive)-modules is sufficiently low. Moreover, the feeding network design imposes a different transition on each of the T/R-modules, which have to be tested prior to installation. A new single hollow-waveguide structure is designed for this purpose.

The development of an accurate phased-array radiation pattern is possible, since the single-element pattern distortions are modelled from measured patterns. The similarity between the simulation results of the ideal beam-forming (array factor) and the measured patterns show that the ideal performance is almost achieved. In addition, the radiation pattern sensitivity to interferences is analysed, and low-cost protection solutions are proposed.

In summary, this work shows how phased-array technology can be open to further fields of application.

Zusammenfassung

In dieser Arbeit beschäftigen wir uns mit der Entwicklung einer *Active Electronically Scanning Array* (AESA) Antenne für zivile Anwendungen. Zwar gibt es schon mehrere Anwendungsfelder für AESA Antennen, aber sie waren bisher auf den Highend- und den militärischen Markt beschränkt, was im Wesentlichen auf die hohen Kosten dieser Technologie zurückzuführen ist. In der vorliegenden Dissertation werden die technischen und wissenschaftlichen Herausforderungen untersucht, welche die Entwicklung solcher Antennen für zivile Anwendungen darstellt.

Die Forschung in dieser Arbeit ist davon geleitet, die regulatorischen Anforderungen der maritimen zivilen Radarnavigation zu erfüllen. Durch eine AESA Antenne, deren Einzelantennenelement Mixed-Signal-Betrieb (analog und digital) unterstützt, ist es möglich, die zusätzlichen Herausforderungen dieser Regulation zu lösen. Um diese Anforderungen mit vertretbaren Kosten zu erfüllen, wurde eine maßgeschneiderte Mixed-Signal SiGe integrierte Schaltung entworfen (H. Erkens et alii, 2009). Mit dem Ziel, die Kosten von AESA-Antennen weiter zu reduzieren, wurden außerdem ein innovatives HF-Speisungskonzept (T. Bertuch, 2007) und ein neues Antennenaperturkonzept (B. Tomasic et al., 1988, M. Pamies et alii, 2010) vorgeschlagen. Das Antennenaperturkonzept ähnelt vorhandenen Navigationsradarantennen, und es kann mittels eines preiswerten Extrusionsverfahrens realisiert werden. Die Neuerung des HF-Speisungskonzepts ist der Verzicht auf einen Isolationsmechanismus zwischen den HF-Ports, was zu hochgekoppelten Ports führt; diese Schwierigkeit wird mit einer neuartigen Betriebstechnik überwunden.

Allerdings bleiben viele Probleme bestehen. Die wichtigsten davon sind die internen Reflexionen, die innerhalb des Netzwerks auftreten, sowie die stark verzerrten Radiationsdiagramme der Einzelelemente; beide sind eine Folge der starken Kopplung zwischen den Ports.

Die internen Reflexionen können nicht vermieden werden. Numerische Simulationen zeigen jedoch, dass ihre Auswirkungen auf das Radiationsdiagramm des Phased-Array geringfügig sind, solange der Reflexionsfaktor der T/R (Sende/ Empfang)-Module niedrig genug ist. Zudem erfordert das neue Speisungskonzept einen anderen Übergang auf alle T/R-Module, welche vor dem Einbau geprüft werden müssen. Eine neuartige Hohlleiter-Struktur wird für diesen Zweck entworfen.

Die Verzerrungen der Einzelelement-Radiationsdiagramme werden direkt von gemessenen Daten modelliert; dies erlaubt die Erstellung eines genauen Radiationsmodells der Antenne. Die Ähnlichkeit zwischen den gemessenen Diagrammen und der idealen Beamforming zeigt, dass die ideale Leistung nahezu erreicht wird. Ferner werden die Empfindlichkeit des Radiationsdiagramms auf Interferenzen untersucht und preisgünstige Schutzmaßnahmen vorgeschlagen.

Zusammenfassend zeigt diese Arbeit, wie Phased-Array-Technologie für weitere Anwendungsgebiete genutzt werden kann.

Acknowledgment - *Agradecimientos*

The Research School on Multi-Modal Sensor Systems for Environmental Exploration (MOSES, hosted by the *Zentrum für Sensorsysteme, University of Siegen*) granted the work here presented, and provided the adequate frame for it. In particular, I want to thank Prof. Dr.-Ing. Loffeld and my mentors, Prof. Dr.-Ing. Haring-Bolívar and Prof. Dr.-Ing. Ender.

The Department of Antennas and Electromagnetic Modelling (AEM), from Fraunhofer Institute for High Frequency Physics and Radar Techniques (Fraunhofer FHR), Wachtberg, Germany, created the proper scientific and technical environment. The department head, Dr.-Ing. Knott, procured that the technical resources to carry this work were available. Claudius Löcker was a fundamental support, who taught many lessons, sometimes beyond electromagnetism and antennas. Specially, I want to express my deepest gratitude to my technical supervisor and project leader, Dr.-Ing. Thomas Bertuch. Moreover, the AEM department allowed for a smooth collaboration with Prof. Dr.-Ing. Heinen, Chair of *Integrierte Analogschaltungen, Rheinisch-Westfälische Technische Hochschule Aachen*, Aachen, Germany.

The laboratory of AEM learned how to deal with my proposals, and reconnected them to reality. Michael Jäger and myself build-up, screwed, constructed, destroyed (only me) and re-constructed uncountable circuits, measurement set-ups and mechanical parts. This work is real thanks to him. Mike Hillmer and Mr. Kremring allowed me to become a better engineer, and tolerated my *Bandido* skills. Thank you guys for your support.

There are several persons in Fraunhofer FHR that improved not only my engineer and scientific side, but made a greater person of myself (alphabetically): Ángel, Anna, Carlos, Claus, Diego, Fabio, Helmut, Jose, Jesús, Karin, Manu, Marian, Stefan F., Stefan V., Stefano and Thomas *extremely* V.

Several persons, and groups of them, helped me to give my best within all these years. I will always have in my mind: Antoñico, Loli, Rubén, Vero, Luís, Cristóbal, Jesús, Eva, *mi ahijado* Mario, Humberto, Giulia, Massimo, the Kirchdauner-Dorf Musikanten, the FGAN-Lunchbreakers, the Unión Musical Horadada and Ahrtal-Tramps. I am also very thankful to the colleagues at Elettronica GmbH, that gave me room and support to present this work.

I could not have started this adventure, also called Ph.D., without the initial push of Prof. Dr. Álvarez-Melcón, who first introduced me to radar, and later pointed me towards Wachtberg.

Mi abuelo Mariano no pudo formar parte de esta aventura, pero he intentado seguir su consejo: paso corto y vista larga. La Mami ha tenido que hacer guardia doble.

The moments of joy shared with my cousins Eva, Paula, María, Irene and Javi always cheered me up, in such a way that, even in the worst moments, the only thing that mattered was to make their smiles bigger and their laughs louder.

Somehow, my uncles and aunties managed to give me strength from 1800 Km. My brother Sysco (only child born) never understood that I can not follow all his advices. At least, he can be sure that, thanks to him, my life changed for good. This is why I would like to have two children, to give them the chance to understand, as I do and live, the meaning of the word brother/sister. It is something beyond a life experience, and we have video, image, audio and physical evidence that can prove it.

Mis padres se han elevado por encima de toda frontera, y han crecido y empujado todos estos años conmigo. Espero que sigan así, todavía nos quedan muchos signos de exclamación que abrir.

Finally, I thank Claudia, she is not an scientist or an engineer, but she learnt how to deal with one. Thank you for all your infinite patience, support and love.

Bonn, June 2015

Mariano Javier Pamies Porras

List of Publications

1. M. Pamies, C. Loecker, T. Bertuch and P. Knott, "Development of a Low-Cost Coherent Radar with AESA Antenna", in *COST-ASSIST*, Wroclaw, PL, Oct. 2009

2. T. Bertuch, M. Pamies, C. Loecker, P. Knott, H. Erkens, R. Wunderlich and S. Heinen, "System aspects of a low-cost coherent radar system with AESA antenna for maritime applications", in *International Kharkov Symposium on Physics and Engineering of Microwaves, Millimeter and Submillimeter Waves*, Kharkov, Ukraine, June 2010, pp. 1−6

3. M. Pamies, C. Loecker, T. Bertuch, P. Knott, H. Erkens, R. Wunderlich and S. Heinen, "Development of an Antenna Front-End for a Low-Cost Coherent Radar Demonstrator", in *German Microwave Conference*, Berlin, GE, March 2010

4. C. Loecker, M. Pamies, T. Bertuch, P. Knott, H. Erkens, R. Wunderlich and S. Heinen, "Antenna Front-End Concepts of a Low-Cost Coherent Radar Demonstrator for S-Band Application", in *European Conference on Antennas and Propagation*, Barcelona, Spain, Apr. 2010, pp. 1 − 5

5. M. Pamies and T. Bertuch, "Maritime navigation radar with active electronically steered array antenna.", in *European Journal of Navigation*, No. 2, 2013

6. M. Pamies and T. Bertuch, "Experimental interference analysis of an S-band AESA antenna demonstrator", in *German Microwave Conference*, Aachen, GE, March 2014

7. M. Pamies, C. Loecker, T. Bertuch, R. Adams, R. Wunderlich and S. Heinen, "An AESA antenna comprising an RF feeding network with strongly coupled antenna ports", in *IEEE Transactions on Antennas and Propagation, vol. 63, pp. 182-194, Jan. 2015*

Contents

1 Introduction **1**
- 1.1 Short history of Phased Array Antennas . . . 1
- 1.2 Motivation . . . 3
- 1.3 Description and organization of the work . . . 6

2 Novel AESA antenna concept **13**
- 2.1 AESA antenna architecture . . . 13
- 2.2 AESA antenna noise figure . . . 17
- 2.3 AESA antenna dimensions . . . 25
  - 2.3.1 Radiation pattern constrains . . . 25
  - 2.3.2 Detection performance . . . 28
- 2.4 Feeding network . . . 31

3 Demonstrator of a novel AESA antenna **35**
- 3.1 Antenna aperture . . . 35
  - 3.1.1 Aperture experimental results . . . 39
- 3.2 Feeding network . . . 41
- 3.3 Solid-state T/R-module . . . 44
  - 3.3.1 T/R-module test-bed . . . 47
- 3.4 Front-end assembly summary . . . 53

4 Near-field based diagram synthesis **57**
- 4.1 Beam-forming technique introduction . . . 57
- 4.2 Near-field radiation model . . . 59
- 4.3 Near-Field to Far-field transformation . . . 64
- 4.4 Near-field based beam-forming . . . 68
- 4.5 Model limitations . . . 72
  - 4.5.1 Near-field sampling effects . . . 72

4.5.2 Predicted far-fields from extrapolated near-fields 75
4.5.3 Near-field radiation model limits 78

5 Far-field optimization and analysis 85
5.1 Near-Field based optimization 86
5.2 Far-field beam-forming and calibration 91
5.2.1 Far-field calibration 91
5.2.2 Far-field based beam-forming 94
5.3 Far-field based optimization 97
5.4 Far-field pattern optimization limits 100
5.5 Feeding network role 102
5.5.1 Feeding network impact on the SLL 103
5.5.2 Proposed feeding network and the SLL 104

6 Receiver protection 109
6.1 Introduction to receiver protection 109
6.2 Sensitivity to interferences 111
6.2.1 Interference experimental set-up 111
6.2.2 Experimental results 114
6.3 State-of-the-Art receiver protectors 118
6.4 Novel receiver protector 120
6.4.1 Protector concept 120
6.4.2 Protector performance 123

7 Conclusions 127
7.1 The novel AESA antenna concept 127
7.2 Diagram synthesis 128
7.3 Receiver protection 129
7.4 Main achievements 130
7.5 Future work 131

Chapter 1

Introduction

1.1 Short history of Phased Array Antennas

Since electromagnetic radiation was discovered by Heinrich Hertz, in 1886 [1], antennas become essential for the society. They can be found in nearly any electronic device, specially if it is related to navigation and/or communications. Actually, the first time that antennas were used with communication purposes was just a few years after H. Hertz experiments: in 1901, Guglielmo Marconi used an array of wire antennas to send information over the Atlantic Sea [2].

Until today's state-of-the-art antennas there is a long path, as a vast amount of antenna types has been developed since the first third of the XX century. Two widely used examples are the Yagi-Uda antennas or the horn antennas [3], [4], that can be found in several systems, e.g.: radio-links or DVB-T stations. Besides, the option of electronic steering has always been a strongly desired asset of antenna front-ends. Several scientific activity related to electronic steering can be found already in the 1950's and 1960's [5], [6], [7]. However, in 1944 the first electronically steered array (ESA) antenna front-end was deployed into the German radar system known as Mammut, which can be observed in Fig.1.1. Its name is probably due to the station's weight, which was said to be in the order of 25 tones. The front-end's wave front direction was steered by means of mechanical phase shifters [8].

Shortly after the first ESA antennas were developed, systems were classified into two big groups: passive electronically steered arrays (PESA) and active electronically steered arrays (AESA) antennas. The generic schemes

of these array antenna systems architectures are illustrated on Fig. 1.2. The PESA antennas steer the wave-front by changing the phase of single antennas or sub-arrays, with a central power generation. In the AESA antenna case, each individual antenna or sub-array is not only steered in phased, but also equipped with its own power generation, having early versions of what is called today Transmit/Receive-modules (T/R-module) [9].

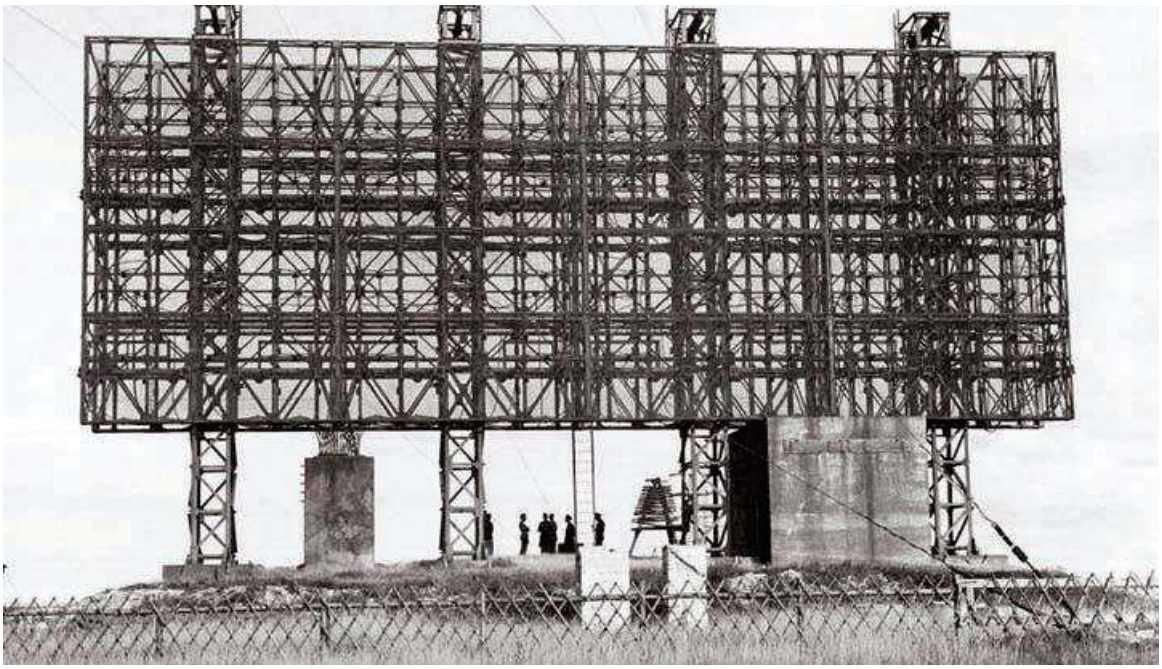


Figure 1.1: Photograph of a Mammut radar station. The main-beam steering was performed with mechanical phase shifters. Source: http://www.radartutorial.eu, Creative-Commons license.

The inherent potential of phased-array antennas is making the technology to continuously evolve since the 1960's [10]. By that time, the capabilities of the electronics to control P/A-ESA had particular focus, mostly in the direction of RF circuitry performance [11], [12] and phase shifters [13–16]. One technological big step was the introduction of digital electronics to control the beam-steering in the middle 1960's [17], [18], [19]. This lead to digital array antennas and/or digital array radars, renaming array radiation pattern synthesis (beam-forming) as digital beam-forming (DBF) [20], [21].

The introduction of digital technologies, and the technical evolution of Monolithic Microwave Integrated Circuits (MMIC), oriented array antennas towards higher system integration in the past decades. In particular, this allowed to integrate T/R-modules on a single chip [22], [23].

Mostly due to the dominant role of the T/R-module into the phased-array costs, several activity in the area of T/R-module technology is in progress since the 2000's, with special focus in lower complexity and cost-related challenges [24–27]. Nevertheless, in general ESA antennas are and were expensive systems, and therefore mostly restricted to the military market.

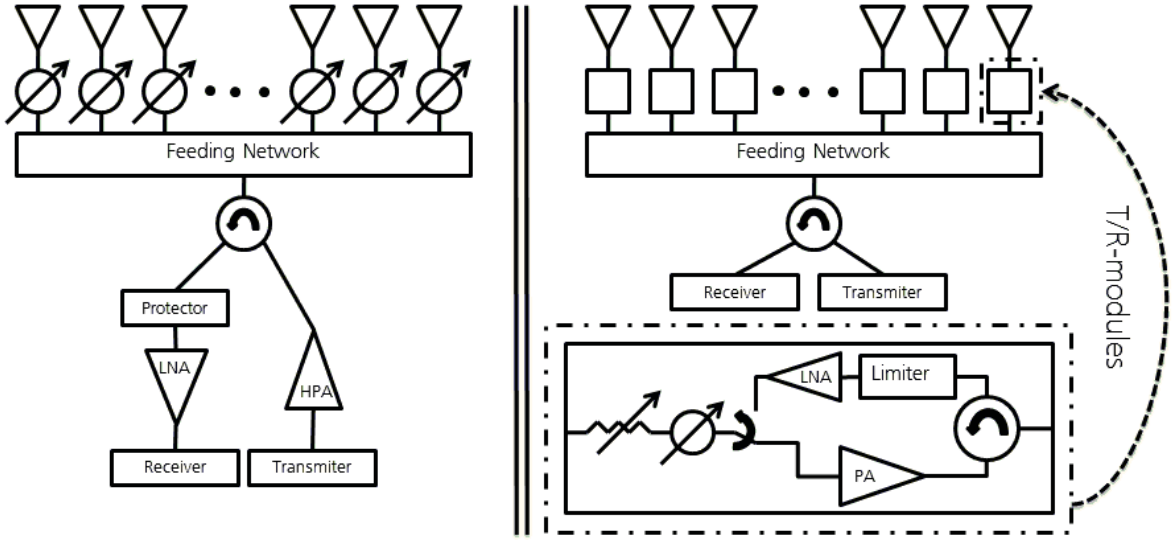


Figure 1.2: Left: sketch of PESA antenna architecture. Right: AESA antenna architecture sketch with an exemplary T/R-module concept.

1.2 Motivation

When the change of the wave-front direction of an antenna front-end is desired, it is still possible to do so without complex and costly electronic technology. An inexpensive solution is a mechanically rotated *passive* array antenna. Usually, these front-ends are refereed to as mechanically steered array (MSA) antennas. An example of this kind of antenna configuration can be observed in Fig. 1.3. Nevertheless, maintenance costs related to the presence of mechanically moving parts are introduced, among other inconveniences such as: rigid scanning with limited speed, lack of service under bad weather conditions or huge space requirements for the rotor's installation and for the rotational motion of the antenna itself.

An example of MSA antenna use is in the area of civil maritime navigation based on radar technology. Maritime radar-based navigation front-ends were required to transmit RF peak powers in the order of KW [28]. Typically,

cavity magnetron tubes are chosen as signal source, nevertheless they have to be replaced regularly. However, current maritime systems regulation [29] allows to reduce the transmit power. This means that solid-state power amplifiers, which can produce very well controlled signal shapes in the order of hundreds of watts [30], become a technology of choice. Furthermore, coherent signal processing techniques can be applied to compensate the reduction of transmitted power. A successful application example of these principles is the solid-state based navigation radar system from Kelvin Hughes [31].



Figure 1.3: Example of X-band mechanically steered array antenna. Significant resource are dedicated to the installation. Source: Wikimedia Commons.

Then, it can be said that the natural evolution is to replace not only the central power source, but also the mechanical steering by electronic steering. In other words, a complete technological change, substituting old-fashioned analogue technology by a *full* solid-state based AESA antenna front-end. The key aspect that can allow this technological change is an inexpensive phased-array front-end.

In this context, it has to be considered that, on the one hand, the design of a phased-array offers multiple architecture and technological choices [10], [32]. On the other hand, the active phased-array has to be an inexpensive (or at least a similar cost) replacement, which can offer a similar or even better performance. Due to that, the degrees of freedom, the technologies of choice and the overall system costs will be rather restricted for commercial applications.

This series of challenges motivated the development of a S-band radar by Fraunhofer FHR, in 2006 [33], [34]. The system concept is exclusively based on solid-state technology, proposing an AESA antenna with inexpensive solid-state T/R-modules and a novel RF feeding network. Up to the author's knowledge, there is no other research group developing a similar inexpensive (*low-cost*) AESA antenna concept.

One of the elements which requires most of the design effort in an AESA antenna is the T/R-module. The Radio Frequency Integrated Circuit (RFIC) technology, necessary for reproducing the required functionality of T/R-modules, demands complex and costly components. In addition, they are performing several analogue and digital functions, and are commonly build-up by MMICs [9,24,25,35,36]. This motivated the design of a full-custom designed chip-set, based on SiGe surface-mount RFIC technology [37], [38], [39]. This semiconductor is very suited for both, high frequency and digital circuits. Therefore, the module's cost can be highly reduced by using mixed-signal circuitry. A satisfying and inexpensive T/R-module demonstrator, where the RFICs are combined with commercial-of-the-shelf (COTS) components, has been built [40]. A module's prototype inspired by this development is currently used into the AESA demonstrator presented in this work.

The inexpensive SiGe semiconductor typically offers a rather limited amount of transmit power [39], [41]. In addition, the most efficient T/R-module operation is achieved when its RF power chain is driven into saturation [40]. Besides, this facilitates the module's operation, since the adjustment of its gain in transmit mode can be complicated due to the low-cost implementation approach. Therefore, all the T/R-modules are to be operated in saturation. Hence, uniform aperture illumination is to be obtained in transmit mode. On the contrary, shipborne radar system regulations imposes strict radiation pattern constrains [29], which necessarily translates into aperture tapering. Here, it is proposed to apply aperture taper exclusively in receive mode. There are several front-end architectures that allow this operation, who commonly demand complex, costly and bulky array implementations [42–45]. In addition, shipborne civil navigation radars based on MSA antennas are using slotted waveguide arrays, realized as an inexpensive, plain and compact circuit [28], [31], [46].

Similarly to a MSA front-end, in this system it is proposed a linear serially-fed AESA antenna (with a series RF feeding network). The network proposed is not inherently matched and has extremely coupled RF ports. However, by means of a novel operation [47], this kind of feeding network

can be successfully introduced into a phased-array antenna, at the price of a fixed taper in receive-mode.

Full horizontal coverage can be provided with four of the proposed AESA antennas, scanning each of them over a range of ±46° with respect to broadside. In addition, a relatively high number of single antenna elements is necessary to fulfil the radiation pattern requirements [29], besides of the necessary aperture taper and the radar performance. However, one AESA antenna with ten radiating elements is considered sufficient as a proof of concept demonstrator, which is presented in this work.

1.3 Description and organization of the work

In this dissertation, novel scientific approaches in fields related to phased-array antennas needed to be developed towards a functional S-band AESA antenna demonstrator. Consequently, in addition to the scientific challenges, many technological issues had to be solved as well. The next paragraphs sum up the scientific and technological milestones of the work in a very compact manner, by briefly describing the contents of every chapter.

Chapter 2. Novel AESA antenna concept. This chapter covers four main aspects: the novel AESA antenna architecture (which comprehends a special feeding network operation technique and inexpensive T/R-modules), the analytical calculation of the noise-figure of active phased-array antennas, the system design (including radar performance) and the novel feeding network operational concept.

Firstly, this chapter introduces a *standard* phased-array architecture, and analysis how to reduce the system's costs. Here, it is proposed to use an inexpensive semiconductor material and increase the T/R-module integration level. In addition, the use of a series feeding network is proposed. As a consequence of the compact feeding and the solid state highly integrated T/R-module operational restrictions, a novel feeding network operation is necessary.

Secondly, it is assumed ideal feeding operation and an analytical calculation of an AESA antenna noise figure is derived. The model is used to compare the noise figure of the novel front-end presented with a *standard* phased-array architecture.

Thirdly, it is shown how to obtain the number of single antenna elements, and the distance between them, as a function of the radiation pattern and the detection requirements. This is done by means of an Uniform Linear Array (ULA) antenna numerical model and the radar equation.

Finally, the novel feeding network operational concept is explained and it is analytically demonstrated the successful operation in receive-mode. The feeding network operation in transmit mode is explained as well.

Chapter 3. Demonstrator of a novel AESA antenna. The complete design and assembly of the proposed AESA antenna front-end's demonstrator is presented in this chapter, including the radiating aperture, the feeding network and the T/R-module. In addition, measurements of representative demonstrators are shown.

The T/R-module implementation represents a technological challenge, since experimental RFICs and COTS components are brought together. In addition, the development needs to consider mass production aspects, modularity and maintain a plane implementation. The activities carried out in the T/R-module development require several areas of expertise, covering circuit-design theory & practice, electromagnetic & microwave theory and self-innovation.

Moreover, every T/R-module has to be tested before deployment into the antenna front-end, in order to ensure correct transmit-mode power, receive-mode gain and overall RF matching. For this reason, an innovative hollow waveguide T/R-module test-bed is designed and produced. This is a challenging circuit, since the transition from/to the feeding network of every T/R-module has different electrical properties. However, the given solution allows to use a single test structure for all the modules. Besides, the T/R-module is controlled with an efficient custom-made FPGA controller.

As a consequence of this design and implementation process, which is using standard existing technologies, the antenna front-end is very robust from both, a technological and a scientific point of view.

Chapter 4. Near-field based diagram synthesis. In this chapter, a near-field based beam-forming principle (diagram synthesis) is shown. In addition, a near-field to far-field transformation is presented. Furthermore, the *pros and cons* of the calibration and beam-forming approaches are analysed with detail.

A successful beam-forming can be guaranteed exclusively if the antenna is reliable. With this purpose, antenna functional tests are carried out in the near-field by means of a linear scanner set-up. This demands the design and construction of a dedicated semi-anechoic space, a printed dipole acting as probe antenna, and a measurement protocol routine for the measurement itself, including an updated version of the single-element FPGA controller.

The custom-made FPGA controller, together with dedicated standard technology PCBs for signal routing, allows to control all the T/R-modules with a single FPGA-board. Furthermore, the same set-up used for the antenna's test can be employed in the calibration and beam-forming.

The beam-forming strategy of the AESA antenna is based on a numerical model of the radiation patterns (calibration), in order to obtain several electronically steered patterns in both, transmit and receive mode. The first model presented is very general, but oriented to obtain the near-fields that would produced the desired far-fields, generating the beam-forming weights by means of Least-Mean-Square algorithm.

Due to the particular AESA antenna configuration, a unique (according to the author's knowledge) antenna calibration approach is developed. On the one hand, the radiating sources are very far away from the near-field measurement plane, therefore, full-wave simulations are necessary to obtain every near-field aperture distribution, corresponding to every electronically scanned main-beam. On the other hand, there is not a straightforward solution to solve the calibration problem in this context. However, an innovative approach is successfully proposed.

Consequently, a near-field to far-field transformation is necessary in order to predict the far-field radiation pattern of the aperture. The transformation in use is proven by simulations and experimental measurements. In addition, a dedicated interpolation routine, derived from Fourier-transform properties, is used to obtain near-field values for intermediate main-beam directions. Therefore, it is not necessary to simulate every single scanned-pattern to obtain the beam-forming weights, but only a few of them.

On the one hand, the antenna radiation model implemented is rather simple and accurate, and the electronic scanning of the aperture is achieved successfully in both antenna modes, transmit and receive. On the other hand, its simplicity implies certain limitations and drawbacks, mostly related to the novel feeding network and the need of a reduced calibration time. These issues are drawn at the end of the chapter. However, in Chapter 5 is presented a post-optimization routine that counter acts the disadvantages of the model.

Chapter 5. Far-field optimization and analysis. This chapter presents a satisfactory beam-forming optimization. In addition, an improved antenna calibration and optimization, based on far-field measurements, is shown. Finally, the role of the novel feeding-network is analysed from a far-field point of view, demonstrating that the optimum antenna response has almost been achieved by the two synthesis methods, near-field and far-field based.

The calibration technique presented in Chapter 4 produces a satisfactory electronic steering of the main-beam. Nevertheless, it has practical limitations, which are previously introduced in Chapter 4. Those limitations produce unsatisfactory effects in the radiation patterns, such as a small main-beam direction errors or an increased side-lobe level (SLL). These deviations are not properly predicted by the near-field antenna radiation model, affecting specially the receive mode operation. However, a method to counteract these issues is developed, by means of on-line (actively changing T/R-module states) iterative routines in combination with optimization algorithms. The far-fields of the antenna after and before the optimization are validated by direct far-field measurements in an anechoic chamber.

Furthermore, it is shown a second antenna radiation model, based on the aperture's far-field, which enhances the previous near-field method. Therefore the prediction of the radiation patterns is much more accurate. Even tough, despite of a correct main beam direction and a significant lowering of the SLL in receive mode, the SLL of high beam-scanning angles are still problematic. However, since patterns are properly predicted by the model, radiation patterns can be enhanced by means of off-line iterative routines (simulating the changes of the T/R-module states), which are combined with optimization algorithms. In addition, accurate numerical models are used to detail the impact of the novel feeding network in the array operation. Furthermore, it is demonstrated that the optimum response (radiation pattern) of the AESA antenna is almost achieved in both operational modes.

The presented far-field based calibration has a main scientific advantage: obtain a very accurate antenna radiation model, with an optimization routine independent of measurements, for an AESA antenna with highly coupled RF ports. Besides, a technical advantage is obtained: the overall measurement time necessary to calibrate the antenna is reduced with respect to the near-field approach. In addition, the presented method can be modified to be applied into a near-field set-up. This way, the inconveniences of the far-field measurement of an electrically large aperture can be avoided, while obtaining a highly accurate pattern synthesis with a reduced measurement time.

Chapter 6. Receiver protectors. The system's immunity against interferences is still to be discussed. Firstly, this chapter introduces the topic of interference protection and sensitivity. Secondly, it is shown how an experimental analysis of interference affects on the far-field radiation pattern of the presented S-band AESA antenna. Thirdly, possible techniques to avoid or mitigate the interference influence on the radiation patterns are drawn. Finally, an innovative system protection approach is presented.

Since the T/R-modules are build up by experimental RFICs, there is a lack of knowledge of interference effects on their functionality. For this reason, the interference sensitivity of the front-end is demonstrated by experimental measurements. A second illumination emitting CW signals is placed in the anechoic chamber, representing an interferer, while radiation patterns are measured. The specifically designed set-up resembles representative CW interference frequencies, operating prominent radar and communication systems bands.

The interference experimental results allow to be aware of the qualitative interference sensitivity of the AESA antenna. Those experimental results provide useful information to address the design of an adequate receiver protector, which can allow to avoid or mitigate system's performance degradation. Therefore, the most suited State-of-the-Art receiver protector techniques for this front-end are evaluated. Unfortunately, when costs and fabrication issues are considered, there are not satisfactory solutions. This motivates the design of an innovative protector, which requires exclusively COTS circuitry, in combination with an inexpensive RF switch. The design can allow to develop radar systems without expensive protection mechanisms.

Chapter 7: Conclusions. The overall thesis outcomes are discussed with detail in this chapter. In addition, further developments towards a fully functional radar front-end and its potential fields of applications are drawn. The most relevant achievements of the thesis can be summarized as:

Achievement no. 1: The T/R-module solution developed is based on COTS components and in an inexpensive and highly integrated SiGe chipset, dramatically decreasing the module costs and complexity, in comparison to State-of-the-Art circuitry

Achievement no. 2: In general, active phased-array antennas are expensive and bulky systems, which in addition are usually complicated to model and design. The system presented in this work offers a compact, plain and

inexpensive AESA antenna, whose functionality is sufficient for civil applications. This can be achieved thanks to the special feeding network operation, in combination with the specific T/R-module technology and the plain antenna aperture concept. This complete technological solution requires the development of specific design, modelling and measurement methods, which are explained with detail

Achievement no. 3: The novel RF feeding network operation concept allows a conceptual change in the antenna architecture. The feeding network is designed to reproduce a fixed amplitude taper, while exclusively parasitic losses are present in the structure. Therefore, the network is not inherently matched and the RF ports are extremely coupled. However, the innovative calibration and beam-forming solutions developed in this work allow its successful use in a serially-feed linear AESA antenna, which is demonstrated by experimental results

Achievement no. 4: The restricted system costs impose a challenge in the system protection, since the system sensitivity to interferences demand the use of expensive existing technology. However, an innovative protection mechanism concept is presented, which can allow to mitigate interferences effects using exclusively COTS components and inexpensive RF circuitry

Chapter 2

Novel AESA antenna concept

In this chapter, a novel AESA antenna concept is presented. A conceptual change on the system's architecture is proposed, resorting to an inexpensive highly integrated T/R-module and an innovative feeding network operation. In addition, a plain and inexpensive radiating aperture is introduced. This is a consequence of several reasons, as explained in Chapter 1, but the most relevant motivations are the necessity of an inexpensive, plain and compact phased-array front-end.

The first section gives a general overview of a generic linear AESA antenna, and explains the approach proposed towards a lower cost front-end.

In the second section, the novel architecture is generally described and its noise-figure is analysed. This allows to understand in a very plain way the AESA antenna concept from a system level point of view.

The third section explains the methodology to obtain the required number of active antenna elements, in order to fulfil the radiation pattern requirements, as well as the radar detection performance [29].

Finally, a novel feeding network operational concept is presented. The optimal choice of beam-forming weights in receive mode is explained, and the operation and requirements of the transmit mode are detailed.

2.1 AESA antenna architecture

AESA antennas, and more generally, phased-array antennas, are described in a vast amount of sources with detail, examples are [32], [48], [49]. However, this section is focused on the AESA antenna architecture [42].

A generic AESA antenna concept is depicted by the block diagram of Fig. 2.1. Three main parts are shown: the single antenna elements, the T/R-modules and the feeding network. In general, the costs of such an antenna are mostly driven by the T/R-module and its components [9], [24], [44]. One extended approach in module costs reduction is the use of application-specific integrated circuits (ASIC).

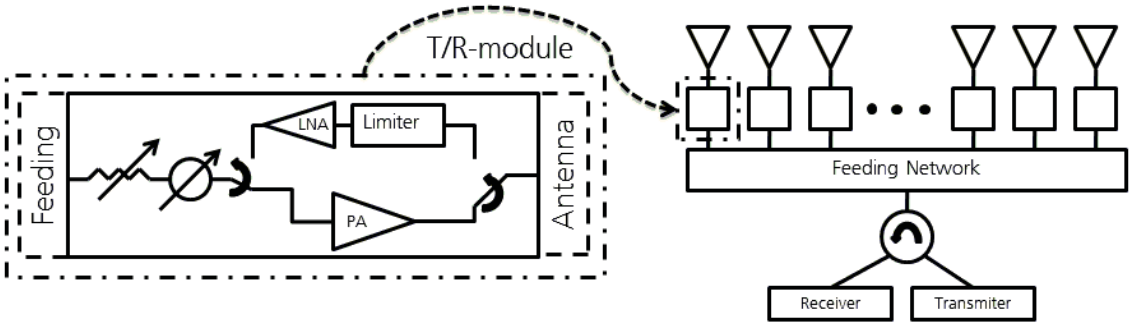


Figure 2.1: Generic AESA antenna scheme with a T/R-module example.

Furthermore, the integration of several functions into a single chip contributes as well to lower the overall module costs. Besides, sharing of functions in transmit and receive reduces the amount of circuitry, and therefore, costs can be again reduced. In addition, restricting the fabrication technology to surface-mount devices (SMD) contributes to lower the manufacturing costs as well. This motivated the development of a full-custom made mixed-signal SiGe-based RFIC chip-set. The T/R-module's concept is inspired in the module from [40]. The T/R-module prototype is described in Chapter 3.

In transmit mode, the T/R-module's output power and operation are restricted due to the module's low-cost implementation approach. Besides, a low SLL is required. This two factors lead to a contradictory situation. On the one hand, low SLL can be achieved by means of aperture taper. On the other hand, in transmit mode, the most efficient T/R-module operation is achieved when its RF power chain is driven into saturation. Besides, this facilitates the module's operation, since, as mentioned above, the adjustment of its gain in transmit mode is rather reduced due to the low-cost implementation approach.

Therefore, all the T/R-modules are to be operated in saturation in transmit mode, and aperture taper is required in receive mode. Consequently, an AESA antenna architecture that can offer different aperture tapers for transmit and receive is necessary. This operation can be achieved by hybrid array

architectures and combining series and parallel feeds [32], [44]. Nevertheless, these solutions demand a high cost and a high system complexity.

Another relevant cost of phased-array antennas is consequence of the space required for the complete front-end assembly, specially due to the electronics, such as the power supply and the feeding network [45]. A compact and plain architecture, in the case of linear array antennas, is obtained with a series feeding network. Nevertheless, the design becomes more critical as the number of antenna elements increases, since the isolation between antenna ports turns more difficult [50], [51], [52].

The combination of a series feeding with the different aperture taper in transmit and receive mode can lead to a complex and expensive phased-array implementation. Despite of that, an inexpensive and plain solution to this problem is proposed in [47]. This patent presents a novel operational principle, which allows to use a feeding network with highly RF coupled (non-isolated) ports, while the taper in transmit and receive can be different. The operational concept, and its application to this specific AESA antenna, is explained with detail in section 2.4.

In addition, since the issue of the antenna port isolation is overcome, and the required instantaneous bandwidth is relatively small [29], a series implementation can be proposed. Besides, the appearance and size of the system resemble a slotted waveguide antenna, commonly used in civil ship-borne navigation radar systems. The proposed AESA antenna concept is depicted in Fig. 2.2. Three main parts can be observed: the T/R-modules, the series RF feeding network and the antenna aperture.

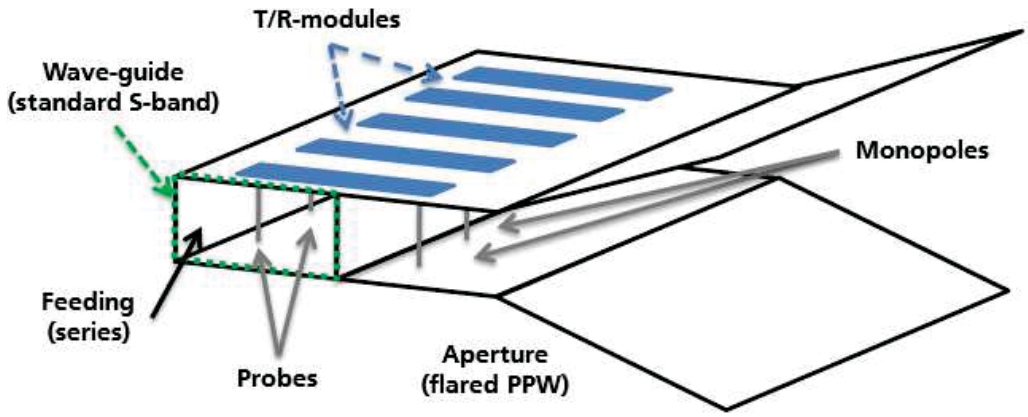


Figure 2.2: Sketch of the proposed AESA antenna. The architecture concept allows to manufacture a compact, plain and inexpensive front-end.

The antenna aperture (Fig. 2.2, right side), is connected to the feeding network (same figure, left side) via the T/R-modules. The T/R-modules feed/sample the aperture's field by means of monopoles, which are inserted into a parallel plate waveguide (PPW). In turn, the PPW is feeding the horn structure depicted in the figure. A top-view sketch of the antenna concept is depicted Fig. 2.3. The acronyms in the figure HIS and TRM-ICC refer to High Isolation Switch) and T/R-module Integrated Circuit, respectively. Those ICs are integral part of the T/R-module, which is explained with detail in Chapter 3.The design of the aperture dimensions is explained in section 2.3. Firstly, height and length of the aperture are defined. Secondly, the number of active elements of the antenna as a function of the required detection performance [29] is determined. The same amount of elements has to guarantee the required radiation pattern and detection performances.

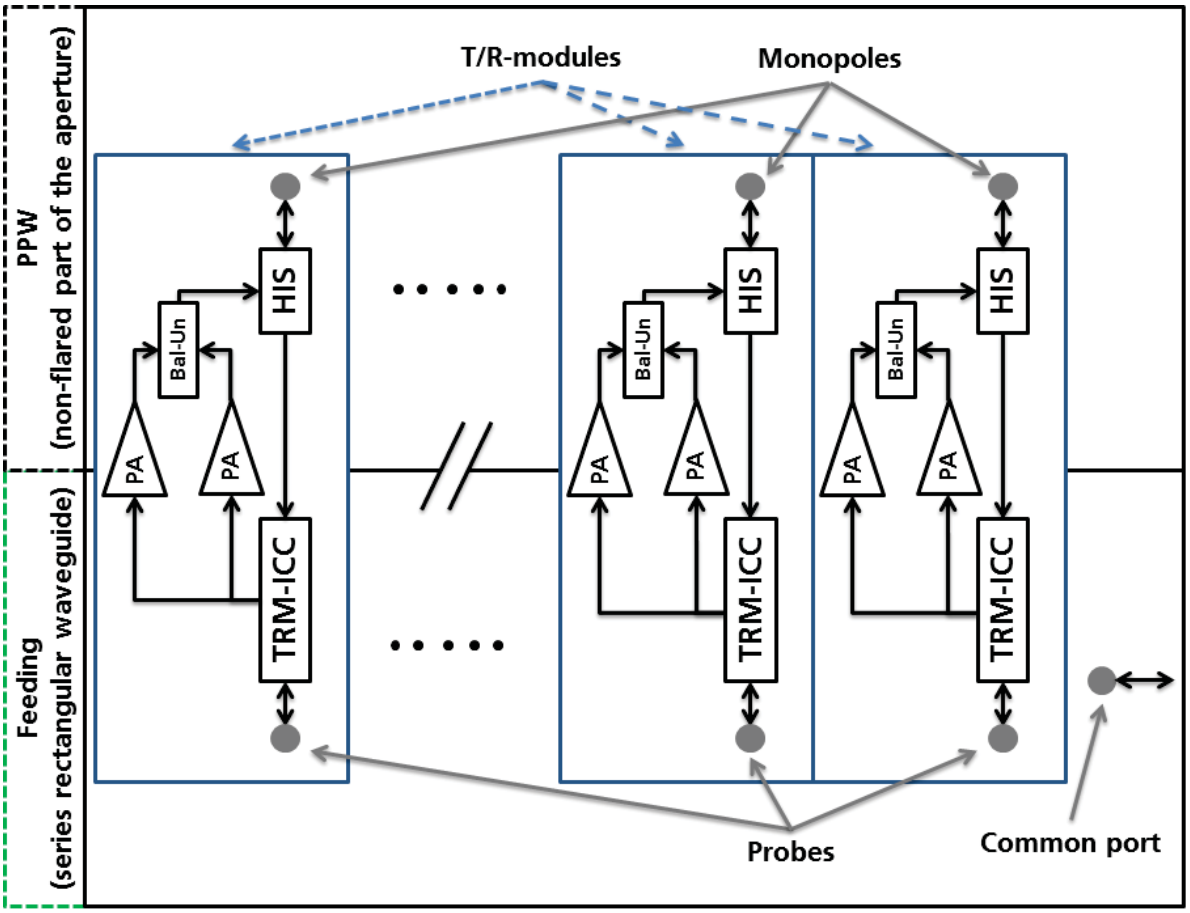


Figure 2.3: Functional sketch of the proposed AESA antenna, showing the main signal paths in transmit and receive mode.

The feeding network is interfaced by T/R-modules via probes, which are inserted parallel to the narrow walls of a standard S-band waveguide. There are no resistive mechanisms or loads to reduce coupling between the T/R-module ports. The design of the feeding network, as well as the operational principle, are explained in section 2.4. The module concept, as well as its implementation, is described with detail in Chapter 3.

The design of the presented front-end is mostly driven by costs. For this reason, the aperture and the feeding network are designed in such a way that both can be extruded at once, as it is the case in slotted waveguides. In addition, the system has to be compact and mechanically robust. We propose a series feeding network with a flared PPW to address these conditions. Furthermore, these structures can be excited with a plane and inexpensive solution: monopoles and/or probes. Moreover, monopole/probes can be used since the required bandwidth of the front-end is relatively small compared to the central frequency.

2.2 AESA antenna noise figure

The discussion at this point is restricted to the influence of the feeding network in the noise-figure. Firstly, the noise-figure of a generic AESA antenna, shown in Fig. 2.4 (left), is analytically obtained. Secondly, the expression for an AESA antenna, whose aperture taper in receive mode is partially realized by passive attenuators and partially by variable gain LNAs (hybrid taper) [53], is analytical obtained. This general case comprises the novel receive mode operation proposed. This second architecture is represented in Fig. 2.4 (right).

The analytical expressions for the noise figure follow the approach in [54]. The noise figure of the front-end is obtained as a function of the signal-to-noise-ratio (SNR) at the feeding network common port and the SNR at the antenna aperture. Besides, ideal feeding operation is assumed. This way, the noise-figure of the RF components and the feeding network of the AESA antenna is obtained. This parameter is necessary to determine the amount of radiating elements from a radar performance point of view (section 2.3.1).

The power received by the front-end can be obtained from the total power density at the aperture, multiplied by the effective area of the antenna array. However, for the sake of clarity, the received power is referred as S_{in}. Hence, the power at every antenna is S_{in}/M, where M is the number of elements.

Furthermore, in the feeding network model is assumed that every single antenna branch contributes to the common port with $1/M$ of its power if there is no aperture taper, which is a mandatory condition for a complete passive network with $M+1$ ports. For instance, with uniform aperture illumination, the taper coefficients are identical and equal to one, therefore, the power contribution of each branch is $1/M$. The magnitudes of the aperture taper weights, the attenuator values and the gains are defined in power.

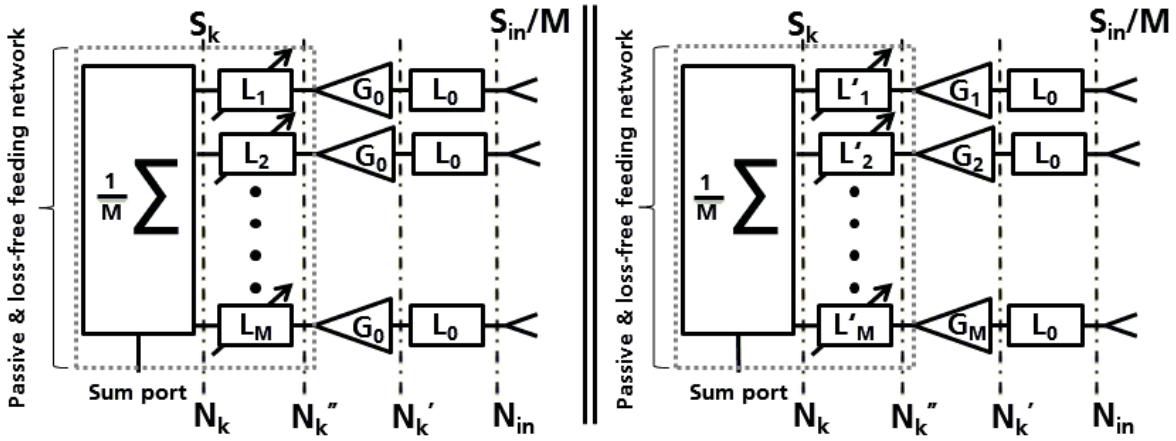


Figure 2.4: Generic front-end schematics. Taper realized by attenuators (left), and by attenuators and amplifiers (right). All the magnitudes are defined in power. The power contribution of every antenna branch to the common port is weighted by $1/M$. For the sake of clarity, the phase shifters are omitted in both sketches.

In the *standard* configuration, the aperture taper is realized only by the passive attenuators after the T/R-modules' LNAs. Therefore, since the feeding network is considered passive, the following relation is to be satisfied:

$$\sum_{k=1}^{M} L_k f = M \Rightarrow f = \frac{M}{\sum_{k=1}^{M} C_k}, \tag{2.1}$$

with $max\{C_k\} = 1$, where:

- M : Number of antenna ports (antenna elements)
- L_k : Passive attenuation of the k-th antenna branch
- C_k : Taper coefficient of the k-th antenna branch
- f : Condition for passive and loss-free feeding network

Consequently, the signal power contribution of every feeding network port from its corresponding antenna element is:

$$S_k = \frac{S_{in} L_0 G_0 L_k}{M} = \frac{S_{in} L_0 G_0 C_k f}{M}, \tag{2.2}$$

where:

- L_0 : Losses from the aperture to the module
- G_0 : LNA power gain

Then, the signal power at the summation port of the network is the coherent sum (amplitude sum) of the input signals [54]:

$$\begin{aligned} S_{out} &= \left(\sum_{k=1}^{M} \sqrt{\frac{S_k}{M}} \right)^2 = \frac{1}{M} \left(\sum_{k=1}^{M} \sqrt{\frac{S_{in}}{M} G_0 L_0 C_k f} \right)^2 = \\ &= \frac{1}{M^2} S_{in} G_0 L_0 f \left(\sum_{k=1}^{M} \sqrt{C_k} \right)^2. \end{aligned} \tag{2.3}$$

The noise power at the common port of the feeding network, N_{out}, can be obtained as the power sum (incoherent sum) of the noise power contributions of each branch, N_k. The noise power contribution of the k-th antenna branch is calculated in a step-by-step approach, applying the Friis equation for the calculation of noise power [55].

The first antenna branch stage is a passive attenuator, L_0. The input noise power, N_{in}, is assumed to be thermal noise, $N_0 = kT_0B_n$ [55]. Hence, the noise power after L_0 gives the following trivial result:

$$N'_k = L_0 \left(N_0 + N_0 \left(\frac{1}{L_0} - 1 \right) \right) = N_0. \tag{2.4}$$

The next stage in the antenna branch is an LNA, and the noise power at the input is N'_k. Applying the same principle, it can be obtained the noise power after the LNA as:

$$N''_k = G_0(N'_k + N_0(F_G - 1)) = G_0 N_0 F_G, \tag{2.5}$$

where F_G is the noise figure of the LNA, which is assumed to be constant.

Again, the same principle can be applied at the last stage of the antenna branch, which is a passive attenuator, L_k. The input noise power is N_k'', consequently, the individual noise contribution of one branch is:

$$\begin{aligned} N_k &= L_k\left(N_k'' + N_0\left(\frac{1}{L_k} - 1\right)\right) = L_k N_k'' + N_0(1 - L_k) = \\ &= N_0(L_k G_0 F_G + 1 - L_k) = N_0\left[(G_0 F_G - 1)L_k + 1\right] = \\ &= N_0\left[(G_0 F_G - 1)C_k f + 1\right] = N_0 f\left[(G_0 F_G - 1)C_k + 1/f\right]. \end{aligned} \tag{2.6}$$

Then, the noise power at the summation port of the feeding network, for the generic AESA antenna case, can be expressed as the power sum (incoherent sum) of all the individual noise (power) contributions, weighted by $1/M$:

$$\begin{aligned} N_{out} &= \sum_{k=1}^{M}\frac{N_k}{M} = \frac{N_0 f}{M}\sum_{k=1}^{M}\left[(G_0 F_G - 1)C_k + 1/f\right] = \\ &= \frac{N_0 f}{M}\left(G_0 F_G\sum_{k=1}^{M} C_k - \sum_{k=1}^{M} C_k + M/f\right) = \frac{1}{M} N_0 G_0 F_G f\sum_{k=1}^{M} C_k. \end{aligned} \tag{2.7}$$

In addition, the input noise of the system is thermal noise, N_0. Hence, the front-end's noise-figure can be defined as:

$$F_T = \frac{S_{in}/N_{in}}{S_{out}/N_{out}}. \tag{2.8}$$

By substitution of eq. (2.3) and eq. (2.7) in eq. (2.8), the front-end's noise figure can be expressed as:

$$F_T = \frac{\frac{1}{M} G_0 F_G f\sum_{k=1}^{M} C_k}{\frac{1}{M^2} G_0 L_0 f\left(\sum_{k=1}^{M}\sqrt{C_k}\right)^2} = M\frac{F_G\sum_{k=1}^{M} C_k}{L_0\left(\sum_{k=1}^{M}\sqrt{C_k}\right)^2}. \tag{2.9}$$

Finally, the front-end's noise-figure for the generic configuration, F_T, is given in a more compact way:

$$F_T = \frac{F_G}{L_0}\eta,\ where\ \eta = M\frac{\sum_{k=1}^{M} C_k}{\left(\sum_{k=1}^{M}\sqrt{C_k}\right)^2}. \tag{2.10}$$

The calculation of the front-end's noise-figure of the second architecture can be done following the same method. However, the aperture taper in receive mode is partially realized by passive attenuators and partially by variable gain LNAs (mixed/hybrid taper) [53]. The problem can be formulated in a generic way, by considering that the amount of taper which is realized by the LNAs and the network is defined in an arbitrary proportion, satisfying:

$$G_k L_k = G_0 C_k f' \Rightarrow G_k = G_0 C_k^{(1-Q)}, L_k = C_k^Q f', \tag{2.11}$$

with $Q \in [0, 1]$ and $max\{C_k\} = 1$, where:

- G_0 : LNA maximum power gain
- G_k : Variable LNA power gain of the k-th antenna branch
- L'_k : Passive attenuation of the k-th antenna branch
- C_k : Taper coefficient of the k-th antenna branch
- f' : Condition for passive and loss-free feeding network
- Q : Distribution of taper between network and amplifiers
- $Q = 1$: The taper is realized by the feeding network only
- $Q = 0$: The taper is realized by the amplifiers only

Independently of the network operational principle, the feeding is defined as a passive and loss-free circuit. Therefore, the equivalent passive attenuators, $L_k = C_k^Q$, are to accomplish the following condition:

$$\sum_{k=1}^{M} C_k^Q f' = M \Rightarrow f' = \frac{M}{\sum_{k=1}^{M} C_k^Q}. \tag{2.12}$$

Consequently, applying the same formulation as for the first front-end architecture, the signal power at the common port gives a similar result:

$$S_{out} = \frac{1}{M^2} S_{in} L_0 \left(\sum_{k=1}^{M} \sqrt{G_k L'_k} \right)^2 = \frac{1}{M^2} S_{in} G_0 L_0 f' \left(\sum_{k=1}^{M} \sqrt{C_k} \right)^2. \tag{2.13}$$

The noise power of the second architecture is obtained following the method shown above: firstly, the noise contribution of the branch is calculated based on the noise power Friis equation, and, secondly, the noise power at the common port is obtained from the power addition of every branch's noise contribution.

The branch's noise power is formulated again using the Friis equation in a stage-by-stage approach:

$$\begin{aligned} N_k &= L'_k \left(N''_k + N_0 \left(\frac{1}{L'_k} - 1 \right) \right) = L'_k N''_k + N_0(1 - L'_k) = \\ &= N_0(L'_k G_0 C_k^{(1-Q)} F_G + 1 - L'_k) = N_0 f' \left(G_0 C_k F_G + 1/f' - C_k^Q \right), \end{aligned} \tag{2.14}$$

where F_G is the LNA's noise figure, which is assumed to be independent of G_k. This corresponds to (e.g.) a LNA-block formed by a low-noise buffer and a variable gain amplifier.

Then, the noise power at the common port of the feeding network with hybrid taper is:

$$\begin{aligned} N_{out} &= \sum_{k=1}^{M} \frac{N_k}{M} = \frac{N_0 f'}{M} \sum_{k=1}^{M} \left(G_0 C_k F_G + 1/f' - C_k^Q \right) = \\ &= \frac{N_0 f'}{M} \left(G_0 F_G \sum_{k=1}^{M} C_k + M/f' - \sum_{k=1}^{M} C_k^Q \right) \end{aligned} \tag{2.15}$$

The front-end's noise power can be simplified using eq. (2.12):

$$N_{out} = \frac{N_0}{M} G_0 F_G f' \sum_{k=1}^{M} C_k. \tag{2.16}$$

Therefore, the noise power of the front-end, N_{out}, is influenced by the feeding network hybrid operation, since f' depends on Q. The value of Q (distribution of taper between network and amplifiers) defines the value of the factor f', which guarantees that the attenuators (defined as a function of the taper coefficients, $L_k = C_k^Q$) on the feeding network are consequent with a passive and loss-free network.

Hence, applying again eq. (2.8) the noise-figure of the second active antenna array configuration is expressed as:

$$\begin{aligned} F'_T &= \frac{\frac{1}{M} G_0 F_G f' \sum_{k=1}^{M} C_k}{\frac{1}{M^2} G_0 L_0 f' \left(\sum_{k=1}^{M} \sqrt{C_k} \right)^2} = M \frac{F_G \sum_{k=1}^{M} C_k}{L_0 \left(\sum_{k=1}^{M} \sqrt{C_k} \right)^2} = \\ &= \frac{F_G}{L_0} \eta, \; where \; \eta = M \frac{\sum_{k=1}^{M} C_k}{\left(\sum_{k=1}^{M} \sqrt{C_k} \right)^2}. \end{aligned} \tag{2.17}$$

The signal power is affected by the hybrid taper, as far as the overall front-end gain is reduced and less energy is summed-up at the common port, depending on the value of f'. Moreover, the noise power is affected in the same proportion by the factor f' with respect to the signal power. At the same time, Q affects exclusively the value of f'. Therefore, the front-end's noise-figure is independent of the taper distribution between the LNAs and the feeding network.

For the sake of completeness, a numerical example with the parameters listed in Table 2.1 is given. The simulation results allow to observe the quantitative impact of the value of Q for several SLL's (Taylor taper) in the dynamic range of the amplifiers (G_k). As mentioned and demonstrated above, the noise-figure of the front-end is independent on the distribution of the taper (Q), assuming ideal feeding network operation. However, the simulation results depicted in Fig. 2.5 show how the dynamic range of the front-end amplifiers can be greatly reduced when the taper realized by the feeding network is increased.

Table 2.1: Front-end parameters

Parameter	**Value**
M	96
Q	$[0, 1]$
SLL	$[20, 45]$ dB
F_G	3.75 dB
L_0	-1.25 dB
Equal side-lobes	4

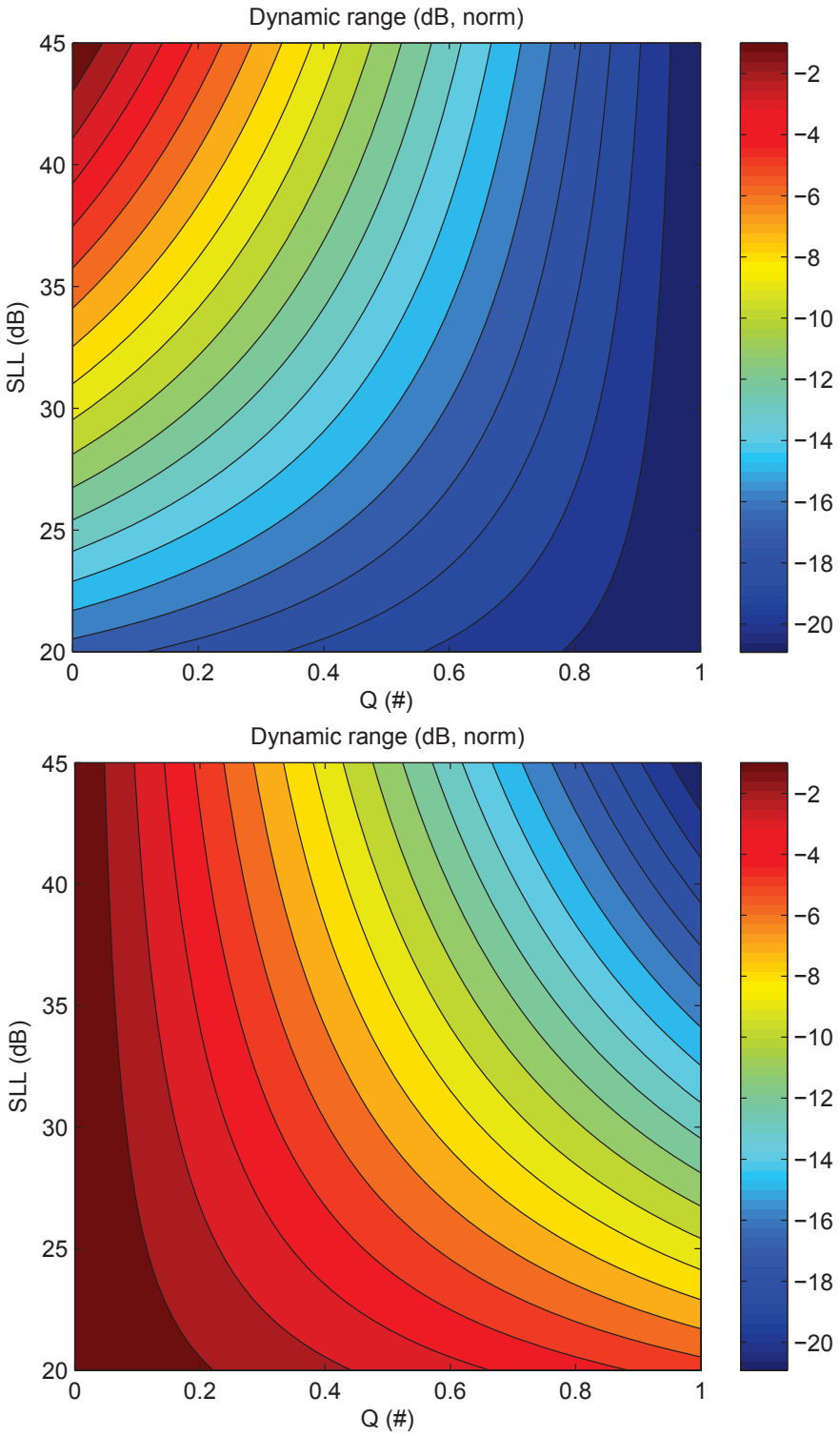


Figure 2.5: Dynamice range simulation results, for several SLLs (Taylor taper) and Q values. The results are normalized with respect to the absolute maximum (top) and the relative maximum of the SLL-row (bottom).

In addition, the analysis presented before assumes that the noise-figure of the LNA (F_G) in every antenna branch is independent of the amplifier gain (G_k). If it is not the case, the dynamic range reduction, consequence of $Q > 0$, will mitigate the variation of the LNA's noise-figure. Consequently, the front-end's noise-figure will be less affected.

On the one hand, the hybrid taper allows to reduce the required dynamic range of the T/R-module amplifiers (G_k). On the other hand, every branch's matching to its corresponding port can be questionable. The feeding network operation proposed (section 2.4) allows to overcome this issue.

2.3 AESA antenna dimensions

The same amount of elements has to guarantee the required radiation pattern and detection performances. Firstly, the aperture dimensions (height and length) are determined. Secondly, it is obtained the number of active elements of the antenna as a function of the required detection performance.

2.3.1 Radiation pattern constrains

As a navigation radar, the proposed active front-end has to provide 360° horizontal coverage. The use of four AESA antenna panels is proposed, each of them performing a one dimensional scanning (H-plane, horizontal). Hence, every AESA antenna performs a uni-dimensional electronic beam-scanning, which is achievable by means of an Uniform Linear Array (ULA) antenna. Therefore, the azimuthal radiation pattern depends on the elements phases and amplitudes, as well as the number of elements and the inter-element distance, which are uniformly displaced along the horizontal axis [48].

The desired electronic beam-steering range of the AESA antenna panels is ±46° with respect to broad-side, including an overlap of 1° between sectors. The operational frequency range is contained in the S-band slot dedicated to civil navigation shipborne radar, from 2.9 GHz to 3.1 GHz.

Besides, the maritime regulation specifies a horizontal radiation pattern with low SLL [29]. On the contrary, the proposed front-end works most efficiently in transmit mode with uniform illumination, as mentioned before. Hence, it is proposed to achieve the two-way radiation pattern low SLL by applying aperture taper exclusively in receive mode. The horizontal radiation patterns constraints given in Table 2.2 are derived.

Two suited aperture taper techniques are the Dolph-Chebyshev Synthesis and the Taylor Line Source Synthesis. Firstly, the taper Dolph-Chebyshev forces more energy in the side-lobe region, since it aims for a constant radiation pattern SLL. Therefore, it cannot be excited efficiently for large antenna arrays [32]. Secondly, the Taylor method provides a taper with good efficiency for large arrays, overcoming a major drawback of the Dolph-Chebyshev function [56]. In addition, the Taylor taper is inherently offering a higher bandwidth [32]. Therefore, a Taylor aperture taper is chosen in this case.

Table 2.2: Antenna radiation pattern constraints

Antenna mode	**BW(deg)**	**SLL(dB)**
TX	$1.5°$	-13
RX	$2.0°$	-30

An ULA's array factor model is used to determine the number of elements and their uniform spacing at the central frequency (3.0 GHz). Gain and scan-loss effects are considered by a numerical approximation of the element pattern in the horizontal plane as $\sqrt{\cos\theta}$ in amplitude. This approximation is sufficient to evaluate the scanning performance of the phased array [57].

The radiation pattern requirements are full-filled with an element distance of 5.5 cm (slightly larger than $\lambda/2$), a total of 96 single antenna elements, uniform illumination in transmit mode and Taylor aperture taper in receive-mode (SLL of -32 dB and four equal side-lobes). Simulation results for the highest main-beam direction (worst-case) are depicted in Fig. 2.6. The simulation includes quantization errors, due to the finite states of the T/R-modules, which reproduce the beam-forming weights.

In addition, in elevation the 3 dB beam-width (HPBW) should be at least $20°$ [29]. This can be accomplished with a moderate increment of the aperture's height, which produces that the radiation pattern focuses in the E-plane. Analytical formulas are used to calculate the optimum height and length of a linear E-plane horn structure [58].

This way, a rectangular antenna aperture is obtained. It is proposed to feed this kind of structure with a parallel-plate waveguide (PPW), resulting in a flared PPW, which can again be excited by a linear array of vertical monopoles. Therefore, the aperture has a rectangular shape, whose longest and shortest dimensions correspond to the extension of the defined ULA and the height of the horn structure, respectively. The apertures feed, as well as the aperture height design, are detailed in Chapter 3.

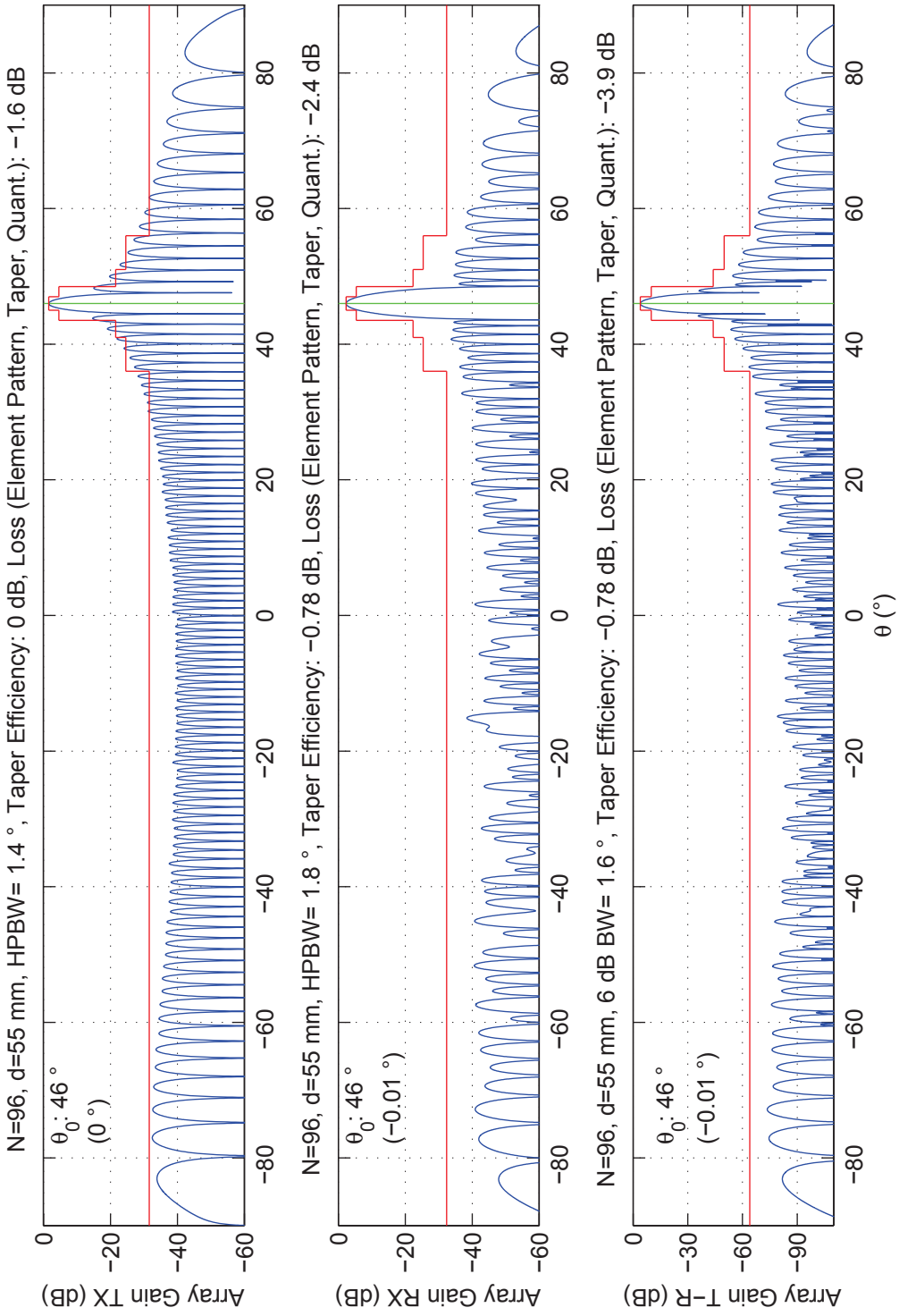


Figure 2.6: Radiation pattern simulation results. In transmit mode the SLL is −13 dB (top). In receive mode, aperture taper is applied in order to obtain a SLL of −30 dB (middle). The two-way radiation pattern meets the radiation pattern constraints (bottom).

2.3.2 Detection performance

Independently of the radiation pattern constraints, the AESA front-end has to guarantee a certain detection performance accordingly to regulation [29]. Due to the limited transmit power of the T/R-modules [40], it is necessary a high number of elements, independently of the radiation pattern constraints.

In addition, since solid-state technology is employed, advanced signal waveforms can be profited by coherent signal processing, by means of signal integration and/or signal compression. Hence, the radar performance is mainly affected by the number of antenna elements and the coherent signal processing gain.

The minimum amount of elements can be obtained from the radar equation and the minimum required signal-to-noise ratio [59]. In this case, the radar equation takes the well-known following form:

$$P_r = \frac{P_{tx} G_{tx} G_{rx} \lambda^2 \sigma L_f L_a}{(4\pi)^3 R^4} = \frac{M P_e (M D_e)^2 \lambda^2 \sigma L_f L_a}{(4\pi)^3 R^4}, \tag{2.18}$$

where:

- P_{tx} : total radiated power
- G_{tx} : antenna gain in transmit mode
- G_{rx} : antenna gain in receive mode
- λ : carrier's wavelength
- σ : target's radar cross section
- L_f : front-end losses
- L_a : atmospheric losses
- R : range of the target
- M : number of active elements
- P_e : transmit power of the single antenna element
- D_e : directivity of the single antenna element

The minimum required signal power is limited by the noise in the receiver, and considering (coherent) signal processing gain [59], the following expression is obtained:

$$P_{min} = \frac{N_0 F_T (S/N)_{out}}{G_{sp}} = \frac{k T_0 B_n F_T (S/N)_{out}}{G_{sp}}, \tag{2.19}$$

where:

- N_0 : input noise (thermal noise)
- F_T: front-end's noise-figure
- $(S/N)_{out}$: minimum required signal to noise ratio
- G_{sp} : signal processing gain
- k : Boltzmann's constant
- T_0 : standard temperature (290 K)
- B_n : signal bandwidth

Finally, the minimum required signal power, P_{min} in eq. (2.19), can be considered as the power collected by the receiver, P_r in eq. (2.18), and the required number of single antenna elements is:

$$M = \sqrt[3]{\frac{k T_0 B_n F_T (S/N)_{out} (4\pi)^3 R^4}{G_{sp} P_e D_e^2 \lambda^2 \sigma L_f L_a}}. \tag{2.20}$$

The front-end's noise-figure, F_T, is calculated following the method presented in section. 2.1, with the parameters given in Table 2.3. The element transmit power, P_e, is taken from the preliminary T/R-module design (Chapter 3), and its directivity is calculated by numerical integration of the shape obtained from the E-plane pattern of an E-plane horn (Chapter 3) and the H-plane pattern of the infinite array environment approximation ($\sqrt{\cos\theta}$) [57].

The atmospheric losses, L_a are calculated as a function of the two-way distance, $2R$, and the atmospheric loss factor, α. The estimation of the system losses, L_f, is based on the parameters listed in Table 2.4. Besides, the losses due to the presence of a target at the half-angle between two discrete scanning

directions are to be included. They are estimated as −2.6 dB, from two-way radiation pattern simulation results, based on the ULA antenna model mentioned above. The total front-end power loss is estimated as −13.4 dB.

The required number of elements is calculated to accomplish with the maritime regulation, which specifies a series of σ's (targets) which have to be detectable at different ranges, with different resolutions [29]. This translates into three different operational system modes, each of them with the parameters given in the Table 2.5. The most critical situations are targets at 2.625 nautic-miles (NM) and 3.7 NM with an RCS of 1.0 m^2 and 0.5 m^2 respectively, which requires 111 active elements.

Table 2.3: Noise figure parameters, F_T

Parameter	**Value**
F_G	4.00 dB
L_0	−1.50 dB
SLL	−32 dB
Equal side-lobes	4

Table 2.4: Front-end losses (L_f)

Cause	**Transmit path**	**Receive path**
Radom	−0.5 dB	−0.5 dB
Ohmic losses	−1.0 dB	−1.0 dB
Active Reflection Coefficient	−0.5 dB	−0.5 dB
Taylor taper with quantization	0.0 dB	−0.9 dB
Element pattern at 46°	−1.6 dB	−1.6 dB
Weighting and feeding network	0.0 dB	−2.7 dB
Total	−3.6 dB	−7.2 dB

Regarding coherent signal processing, plane wave-forms such as BPSK modulations are a good candidate for signal compression, since they can be implemented with simple circuitry. Signal integration and compression waveforms, as well as other issues restricted to civil navigation shipborne radar, are briefly evaluated in [34] for this particular front-end architecture, giving a total amount of 96 elements. A deeper analysis, which also considers other issues restricted to maritime civil navigation, is given in [60].

This preliminary calculation of the radar performance shows the potential of phased-array antenna technology based on inexpensive semiconductors, which typically provide low output powers (e.g. SiGe [39], [41]), in the field of civil applications, when combined with low system losses, as it can be expected in series architectures.

Table 2.5: System parameters

Parameter	**Mode A**	**Mode B**	**Mode C**
B_n	10 MHz	5 MHz	2.5 MHz
R (max)	3.0 NM	21.0 NM	96.0 NM
G_{sp}	20 dB	26 dB	23 dB
σ	1 m^2 (2.625 NM)	0.5 m^2 (3.7 NM)	
F_T	6.28 dB		
$(S/N)_{out}$	14.30 dB		
P_e	27.00 dBm		
D_e	11.10 dB		
λ	0.10 m		
L_f	-13.40 dB		
α	-10^{-5} dB/m		

2.4 Feeding network

Array feeding networks can be classified in three main categories: series, corporate or spatial [42], [61]. In order to reduce the losses and the size of the front-end, an exclusively series configuration has been chosen. Thereby, the complete front-end offers similar appearance and size of a common civil navigation maritime radar, based on an MSA antenna comprising a slotted waveguide.

In addition, typically, the design of AESA antennas RF feeding networks is done in such a way that the antenna ports are isolated and inherently matched. This can be achieved introducing resistive components or loads, which becomes problematic for large number of antenna ports in the case of series architectures [50], [51], [52]. Here, a structure without port isolation measures is proposed. Hence, the network ports are non-inherently matched and strongly coupled.

The operation of a feeding network with strongly coupled antenna ports can be difficult in an AESA antenna. The principle presented in [47] allows to successfully operate such a network, even with different aperture taper in transmit and receive mode. Following, the choice of the optimum weights to excite the network in received mode is explained.

The optimum response of the feeding, when it is operated in transmit mode, can be defined as:

$$\underline{b}_{tx} = \underline{\underline{S}}\ \underline{a}_{tx},\ with\ \underline{a}_{tx} = \begin{pmatrix} 1 \\ 0 \\ \dots \\ 0 \end{pmatrix}, \tag{2.21}$$

where port no. 1 is the summation/common port, $\underline{\underline{S}}$ is its scattering matrix, $\underline{a}_{tx}$ is the incident waves vector and $\underline{b}_{tx}$ is the outgoing waves vector. Therefore, in transmit mode (ideally) only the summation port of the feeding network is excited, with perfect matching at all ports:

$$\underline{a}_{tx} = \begin{pmatrix} 1 \\ 0 \\ \dots \\ 0 \end{pmatrix}, \underline{b}_{tx} = \begin{pmatrix} 0 \\ b_1 \\ b_2 \\ \dots \\ b_N \end{pmatrix}. \tag{2.22}$$

In receive mode, the reciprocal behaviour is desired, which means that the excitation of the all antenna ports of the network produces only an outgoing wave at the common port:

$$\underline{b}_{rx} = \begin{pmatrix} 1 \\ 0 \\ \dots \\ 0 \end{pmatrix}, \underline{a}_{rx} = \begin{pmatrix} 0 \\ a_1 \\ a_2 \\ \dots \\ a_N \end{pmatrix}. \tag{2.23}$$

This ideal behaviour can be achieved when the excitation is equal to the conjugate complex of the feeding network response in transmit mode: $\underline{a}_{rx} = \underline{b}^*_{tx}$ [47]. The successful excitation of the network can be demonstrated in two steps. Firstly, the ideal response for the optimum excitation is:

$$\underline{b}_{rx} = \underline{\underline{S}}\ \underline{a}_{rx} = \underline{\underline{S}}\ \underline{b}^*_{tx} = \underline{\underline{S}}\ \underline{\underline{S}}^*\ \underline{a}^*_{tx}. \tag{2.24}$$

Secondly, since $\underline{\underline{S}}$ represents a reciprocal and lossless network:

$$\underline{\underline{S}} = \underline{\underline{S}}^T \ (reciprocal) \Rightarrow \underline{\underline{S}}\ \underline{\underline{S}}^* = \underline{\underline{S}}\ \underline{\underline{S}}^{T*} = \underline{\underline{I}} \ (lossless), \tag{2.25}$$

where $\underline{\underline{I}}$ is the identity matrix. Moreover, by substitution of eq. (2.25) in eq. (2.24) it is obtained that:

$$\underline{b}_{rx} = \underline{a}^*_{tx}, \underline{a}_{tx} \in \Re \Rightarrow \underline{b}_{rx} = \underline{a}_{tx}. \tag{2.26}$$

The physical meaning is that the antenna ports of the network are perfectly matched in receive-mode when the excitation vector is the conjugate complex of the output waves' vector in transmit mode, and all the power is summed-up at the common port of the network.

In the receive mode, the desired antenna radiation pattern SLL is −30 dB. One option to achieve this is applying a Taylor aperture distribution [56], [62]. Respecting the requirement to operate the feeding network reciprocally, the desired Taylor aperture amplitude taper is generated in equal parts by the network and the T/R-modules. This means that both realize a square-root of Taylor aperture amplitude distribution. At the same time, the T/R-modules must also reproduce the conjugate phase at each antenna port with respect to the transmit case, compensating the progressive phase at the aperture.

In the transmit mode, the feeding network is operated in a slightly different manner. The most efficient T/R-module operation is achieved when its RF power chain is driven into saturation [40]. In addition, this facilitates the module's operation, which is rather reduced due to the low-cost implementation approach. This restriction automatically leads to an uniform antenna aperture distribution, and consequently the radiation pattern will have approximately −13 dB of SLL. This can be achieved even with a feeding network that inherently produces a certain taper over the input ports: the maximum input power and the minimum input power to saturate the T/R-module's power chain, has to cover the same range as the feeding's power taper.

As mentioned above, the combined transmit and receive patterns (two-way) gives a system radiation pattern which full-fills the horizontal pattern requirements, for any scanning angle. This is achieved with an element distance of 5.5 cm, and a total of 96 single antenna elements, applying uniform illumination in transmit mode and Taylor aperture taper (−32 dB, four equal side-lobes) in receive-mode.

Chapter 3

Demonstrator of a novel AESA antenna

The previous chapter presented a novel AESA antenna architecture concept. Within this chapter, the implementation of a demonstrator based on the introduced architecture, using inexpensive and standard existing technologies, is shown. This front-end approach resorts to a *low-cost* S-band AESA antenna when compared against other AESA antenna systems [63], [64], [65].

Firstly, the antenna aperture is presented; the design steps are explained and measurement results are shown. Secondly, the feeding network design and implementation is explained. Thirdly, the T/R-module is shown with detail. Finally, a summary of the implementation process milestones is given.

3.1 Antenna aperture

The number of active elements of the AESA antenna is previously determined from the radiation pattern constraints and the required performance, as shown in Chapter 2. In this case, the design is restricted to maritime system's regulation [29]. However, this methodology can be applied to any front-end design.

In addition, the mentioned regulation gives radiation pattern constrains in elevation: the 3 dB beam-width (HPBW) should be at least 20°. This can be accomplished with a moderate increment of the aperture's height, which produces that the radiation pattern focuses in the E-plane. This way, the antenna aperture proposed has a rectangular shape. This kind of structure

can be feed with a parallel-plate waveguide (PPW). Hence, the structure results to a flared PPW, which can again be excited by a linear array of vertical monopoles.

A cross sectional sketch of the front-end is shown in Fig. 3.1. The probes of the series feeding network are on the left of the figure, and they extend perpendicular to the drawing plane. The rectangular antenna aperture is on the left side of the figure, and again extends in the perpendicular plane. The aperture is feed by a flared PPW, which is excited by a linear array of vertical monopoles inserted into the non-flared part of the PPW (approximately in the middle part of the not-to-scale sketch). The array extends in the horizontal direction, perpendicular to the drawing plane. The elements are sharing the PPW. Besides, the monopoles are placed approximately a quarter of a wavelength in front of a vertical metal wall, which is short circuiting the PPW. This aperture concept is similar to one in [66], [67], but the antenna elements are fed by microstrip lines and the PPW is flared.

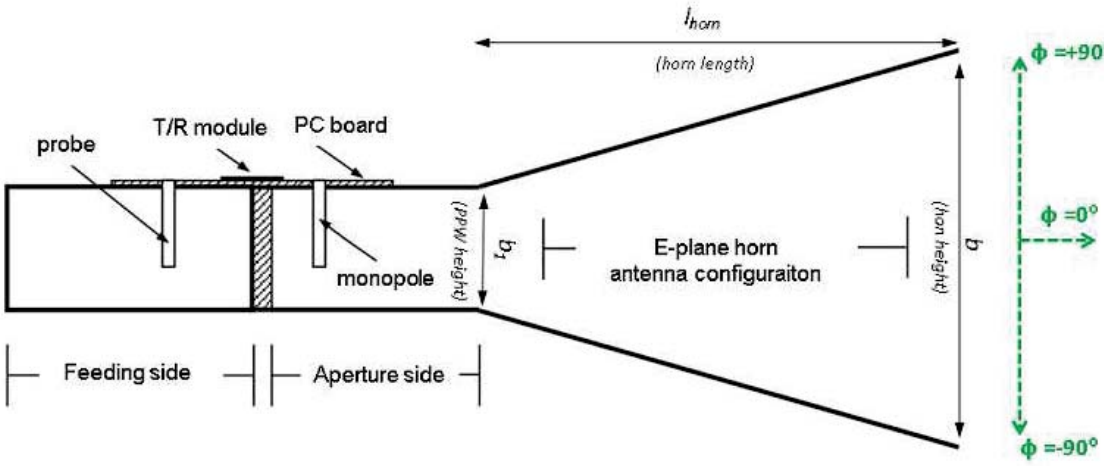


Figure 3.1: Not-to-scale front-end cross-section. It can be seen the horn configuration, the feeding network and the location of the T/R-modules.

The aim is to focus the θ component of the E-field along the vertical axis (the vertical component of the far-field radiation pattern in the vertical plane). This radiation plane corresponds with the E-plane in the considered reference system, $\theta = 0°$ along $\Phi = [-90°, +90°]$ (see Fig. 3.2).

The radiation pattern in the E-plane cut can be focused by means of an E-plane horn. In addition, for the design of the E-plane horn, we can assume that the dominant TE_{10} mode of the PPW is again the same for the aperture's field.

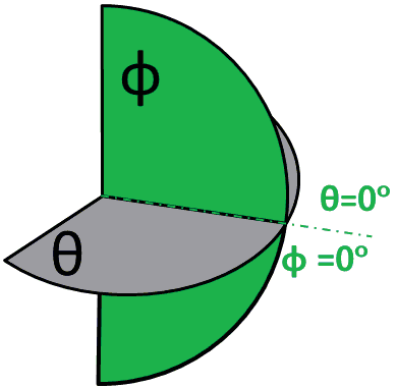


Figure 3.2: Representation of the far-field radiation planes. The E-plane is contained in $\theta = 0°$, $\Phi = [-90°, +90°]$.

Analytical formulas can be used to determine the optimum height and length of the horn structure. Following, it is summarized the procedure used to obtain the optimum aperture height, for the minimum length (detailed in [58]). The amplitude of the vertical component of the radiation pattern (in azimuth) can be expressed as follows, neglecting scaling and phase factors:

$$E_\theta(\Phi) = \sqrt{(\rho_1/\lambda)}[1 + \cos(\Phi)]F(t_1, t_2), \tag{3.1}$$

where λ is the free-space wavelength and:

$$F(t_1, t_2) = [C(t_2) - C(t_1)] - j\,[S(t_2) - S(t_1)]\,, \tag{3.2}$$

$$C(x) = \int_0^x \cos\left(\frac{\pi}{2}t^2\right) dt,\;\; S(x) = \int_0^x \sin\left(\frac{\pi}{2}t^2\right) dt, \tag{3.3}$$

$$t_1 = \sqrt{\frac{k}{\pi\rho_1}}\,[-b_1/2 - \rho_1 \sin(\Phi)]\,,\;\; t_2 = \sqrt{\frac{k}{\pi\rho_1}}\,[+b_1/2 - \rho_1 \sin(\Phi)]\,. \tag{3.4}$$

The cosine and sine Fresnel integrals, eq. (3.3), are well known and tabulated. The integration line goes along the perpendicular plane of the aperture, i.e. over its height. The parameter ρ_1 can be calculated from the aperture and the PPW heights, noted as b and b_1 respectively:

$$\rho_1 = \frac{b_1 l_{horn}}{b_1 - b} \tag{3.5}$$

Then, by calculating the directivity, D_θ, for several aperture height and length (b_1 and l_{horn} respectively) configurations, it can be selected the combination that produces the maximum directivity and the desired HPBW, but for the minimum length. The real HPBW will be slightly wider, since effects like edged diffraction are not taken into account by the model.

As mentioned above, the rectangular antenna aperture is feed by a PPW, resulting in a flared PPW. The flared PPW can be excited by an array of monopoles, which is inserted into the non-flraed PPW. Likewise, the PPW is short-circuited with a metal wall and the monopoles are sharing the PPW.

When all the elements are being operated at the same time, the mutual coupling between them dominates the active reflection coefficient (ARC) of the monopole feeds, which varies with the scanning angle of the antenna main beam [57], [68], [69]. Consequently, the element feed's ARC is different depending on the excitation of the neighbouring elements.

The ARC of the m-th element can be calculated directly from measured or simulated scattering parameters (S_{mn}), the element distance (d_e) and the desired main-beam direction ($\theta_0 \in [-46°, +46°]$) [57]:

$$\Gamma_m(\theta_0) = e^{+jkmd_e \sin\theta_0} \sum_{n=1}^{M} S_{mn} e^{-jknd_e \sin\theta_0}. \tag{3.6}$$

The complete antenna is formed by a large number of elements, therefore, periodic boundary conditions for the embedded element can be assumed in the design process, resorting to an infinite size array antenna approximation.

Assisted by full-wave simulations, the monopole distance to the short circuit wall and its length are optimized. The inter-element distance is disposed of the design parameters of the aperture fed, since it has been previously fixed (Chapter 2). The target of the optimization is an ARC smaller than -10 dB, for any beam-scanning from 0° to +46° in the required frequency range, from 2.9 GHz to 3.1 GHz.

For the sake of completeness, the active gain of an ULA antenna with a large number of elements is reproduced. Edge effects can be neglected, therefore the ARC, $\Gamma_m(\theta_0)$, is identical for all elements and the active antenna gain can be calculated as [57]:

$$G^{act}(\theta_0) = MG_0(\theta_0)\left(1 - |\Gamma(\theta_0)|^2\right), \tag{3.7}$$

where $G_0(\theta)$ is the gain of the single-element. Therefore, a low ARC guarantees a high gain of the antenna array at the desired main-beam direction.

3.1.1 Aperture experimental results

The number of single antenna elements is reduced from about 100 down to 10 for demonstration purposes. Three dummy elements are included at each side of the linear array in an attempt to minimize edge effects, resorting to a total amount of 16 antenna elements. This way, the behaviour of the inner elements of the demonstrator will be more similar to an infinite size array antenna configuration.

The scattering matrix of the aperture elements is obtained from successive reflection and transmission measurements with a two-port network analyser, when all remaining ports are terminated with matched loads. The measurements are done in an anechoic chamber to avoid environmental reflections.

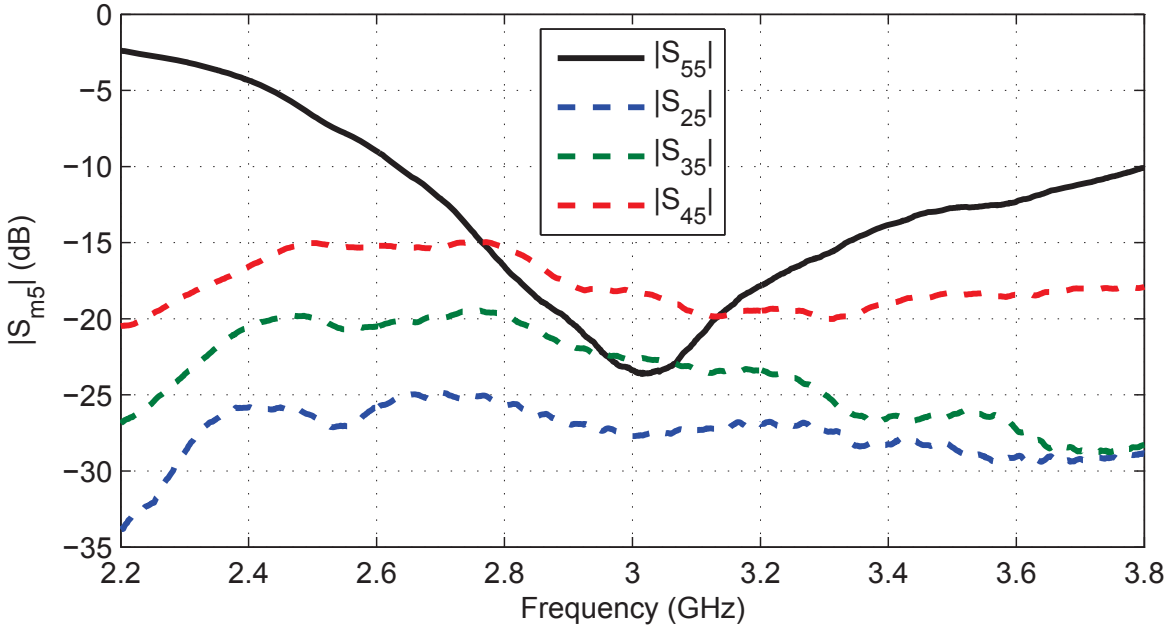


Figure 3.3: Measured reflection coefficient of the active element no. 5, including transmission to successive neighbouring elements. The antenna demonstrator is formed by 10 radiating elements and 3 dummy elements on each side.

The measured (passive) reflection coefficient of the active antenna element no. 5, which is near the centre of the array, is depicted in Fig. 3.3. The matching is -20 dB at the central frequency, and below -15 dB in the frequency band of interest. Moreover, the transmission to the near neighbouring elements is shown in the same figure. As expected, the strongest coupling is between two neighbouring elements, but it is still less than -15 dB.

As mentioned above, the ARC of the elements can be obtained from the (measured or simulated) scattering parameters, eq. (3.6). Fig. 3.4 depicts the ARC of element no. 5 (calculated from the measured scattering parameters), which is always below −12 dB in the desired frequency and scanning ranges. These results proof the plain and inexpensive aperture concept.

In addition, since the monopole is optimized for operation in an infinite size array antenna, even better performance can be expected for an AESA antenna with more elements.

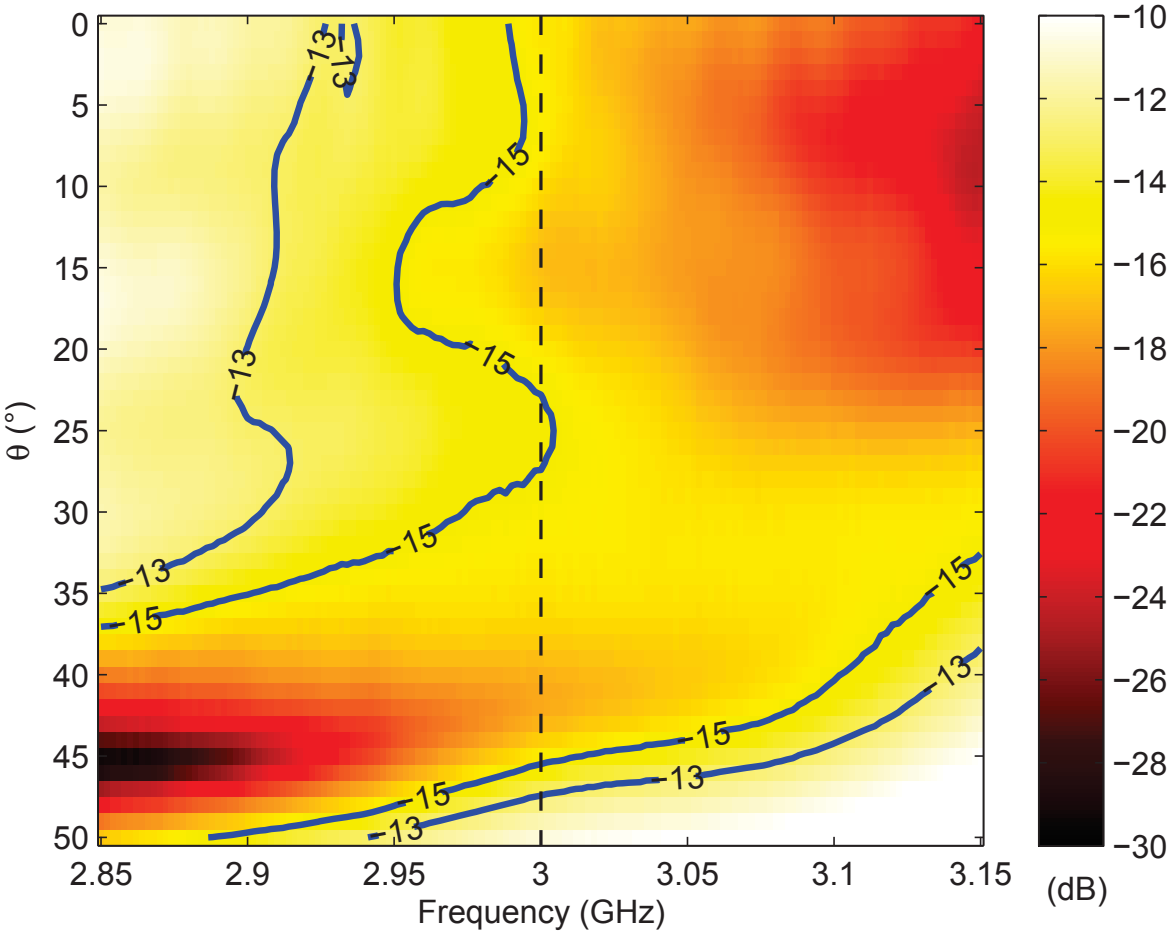


Figure 3.4: Calculated ARC of the active element no. 5 with respect to frequency and beam-scanning angle. The antenna demonstrator is formed by 10 radiating elements and 3 dummy elements on each side.

3.2 Feeding network

The proposed AESA antenna has two operational modes, transmit and receive. As explained before, in transmit mode, uniform aperture illumination is used, hence, amplitude aperture taper is applied exclusively in receive mode, in order to obtain low peak side lobes. The most suited linear array synthesis in this case is the Taylor line source method, as discussed in Chapter 2. Nevertheless, very low SLL are in general difficult to accomplish [70]. For this reason, a 3 dB margin is added in the design process, hence, the SLL in receive mode by design is -35 dB.

The main requirement of the feeding is the reciprocal operation in receive mode. Therefore, the desired Taylor aperture amplitude taper is generated in equal parts by the network and by the T/R-modules. This means that both realize a square-root of Taylor aperture amplitude distribution. At the same time, the T/R-modules must reproduce the conjugate phase at each antenna port with respect to the transmit case, compensating the reciprocal phase at the antenna aperture.

As explained in Chapter 2, the feeding is operated in a slightly different manner in the transmit mode. The T/R-modules' internal RF power chain has to be driven into saturation. This would produce the same output power at every antenna element, which automatically leads to a radiation pattern with approximately -13 dB of SLL.

The antenna's frequency range of operation is contained in the S-band. Hence, the feeding network is implemented using a standard S-band waveguide, supporting the TE_{10} mode. A plain manner to couple-out/in energy from a rectangular waveguide supporting the fundamental TE mode is using vertical probes, inserted into the waveguide and oriented parallel to the narrow lateral side wall. Thereby, all the ports in the feeding are transitions from waveguide to shielded-microstrip lines, via monopoles.

The transition of the common port of the network is a probe placed in the centre of the waveguide. The distance of the probe to a short-circuiting wall, as well as its length, are optimized to excite the mentioned TE_{10} mode and obtain a good matching to the shielded-microstrip line.

The distance to the narrow waveguide wall is the same for all antenna ports, except for the last one. The last port and the feeding's common port are centred between the narrow walls. The only difference between the transitions is the length of the probes. This way, the manufacturing process of the T/R-modules and the feeding network is simplified.

The antenna probes cannot be placed in the centre of the waveguide's broad-wall. On the one hand, this would be the best position for coupling out as much power as possible, on the other hand, this would also cause strong reflections inside the waveguide. The reflections are reduced moving the probes away from the centre. However, this way the maximum amount of power that can be coupled out of the waveguide per transition is also reduced. Thus, the perfect position of the probes is the one that just allows to couple out as much power as necessary (optimizing the probe length) with minimum reflections, i.e.: the distance to the waveguide lateral wall has to be chosen in such a way that, it creates the minimum distortion inside the waveguide, but at the same time, the required amplitude taper range can be achieved.

The probes' lengths are optimized, for a given distance to the waveguide lateral wall, as a function of the desired transmission parameter of the ports, based on tabulated results from full-wave simulations of a single transition. The element spacing (d_e) is kept constant (5.5 cm, Chapter 2). The full-wave simulation model of the complete feeding can be observed in Fig. 3.5.

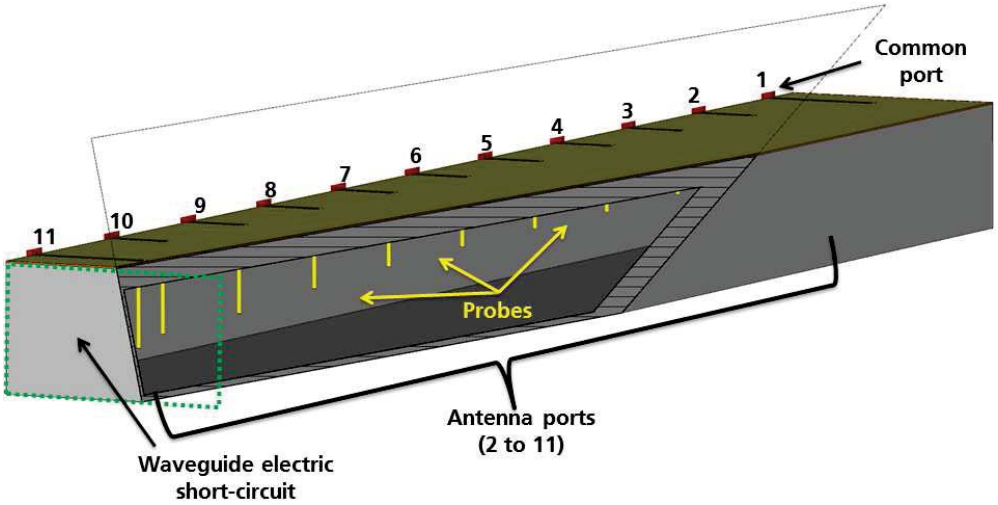


Figure 3.5: Full-wave simulation model of the realized feeding network. Port number one (right) refers to the common port. The element spacing is the same as determined in Chapter 2, which allows to full-fill the azimuth radiation constraints.

Measurement results are compared to the ideal square-root of Taylor amplitude taper in Fig. 3.6. The agreement from port number two to port number ten is rather good. Besides, the small differences can be compensated by the T/R-modules. The transmission of the last port (number eleven) is

higher than desired. This is a consequence of the limited power that can be coupled out by the last but one port. The amount of power could be increased by moving the probe more to the centre of the waveguide, but in order to limit the manufacturing costs all lateral probe positions should be identical. Hence, all the remaining power after the last but one port will reach the last port. Consequently, the last port needs to be in the waveguide's centre to minimize possible reflections, specially in such a short network.

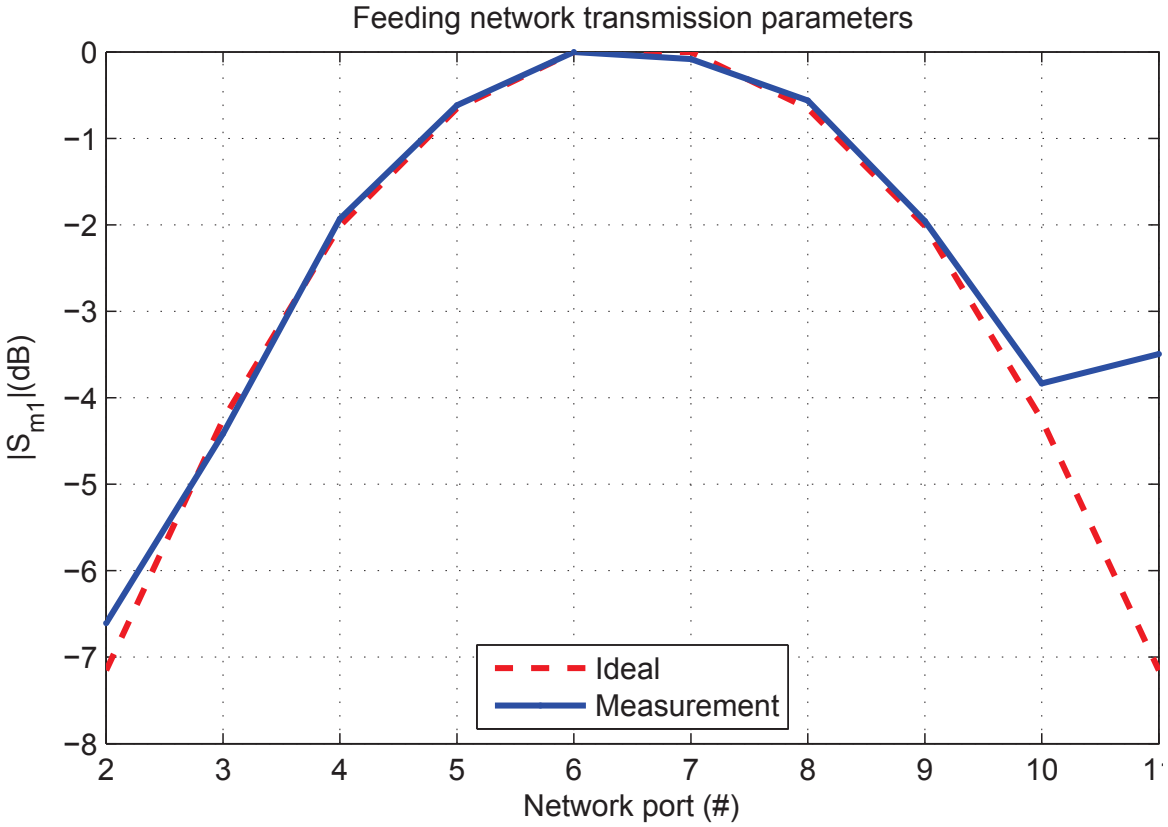


Figure 3.6: Measured taper coefficients against reference square-root of Taylor values. Maximum values are normalized to 1 (linear).

In case of a real system with approximately 100 radiating elements, the deviation on the last element can be neglected and compensated by the modules. In the case of the demonstrator with only ten elements this might be problematic. Besides, the SLL of the radiation pattern can be affected by any deviation of the taper realized by the feeding, since the network has to be operated reciprocally (Chapter 2). Deviations from the ideal taper will cause outgoing waves at the T/R-module ports in receive mode. If these reflections are sufficiently absorbed by the T/R-modules, the SLL will not

be affected. However, the measurement results shown in following chapters indicate that also in this difficult situation compensation is still possible.

3.3 Solid-state T/R-module

The AESA antenna presented is proposed as an alternative solution, with a comparable costs, to the use of MSA antennas typically seen in civil maritime radar, even though several dozens of T/R-modules are necessary to obtain the required performance and functionality. Therefore, the active element costs are to be as low as possible.

The costs reduction of T/R-module has been widely investigated [24–27]. Similarly, an inexpensive T/R-module concept is shown here, inspired by [40], featuring an output power of 27 dBm and a maximum receive gain of 30 dB.

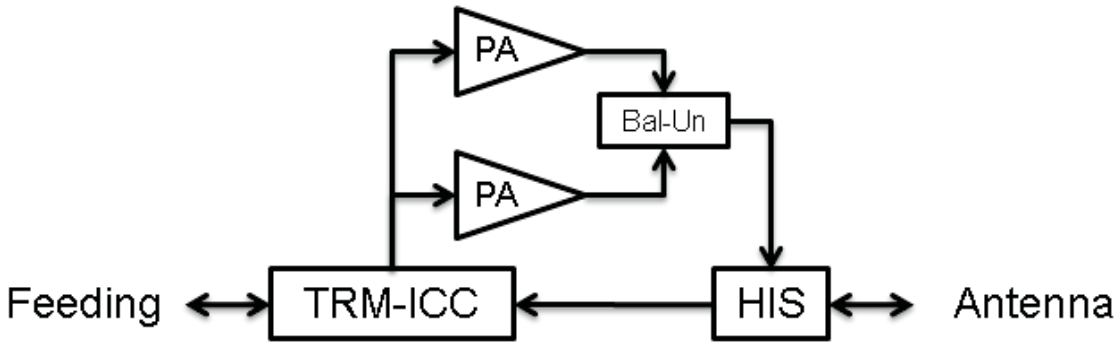


Figure 3.7: T/R-module functional block diagram. DC-supply has been omitted. The TRM-ICC works as a common-leg structure with a variable gain LNA.

The block-diagram of the T/R-module here presented is shown in Fig. 3.7. This module is based on three main ICs. The first IC is an inexpensive high isolation switch (HIS) [71], which replaces a circulator. The second one is a high-gain COTS power amplifier (PA) [72]. Two PAs are disposed in a parallel arrangement, which results to +24 dBm of output power. Several inexpensive amplifiers providing the desired output power (+27 dBm) can be considered for future developments, e.g. [39, 73–75]. The third circuit performs the most relevant and challenging tasks of the module, and it is called transmit-receive-module integrated core circuit (TRM-ICC) [38].

The TRM-ICC is a complex highly-integrated full-custom mixed-signal circuit. It contains the functional blocks that can be found in the common-leg of a T/R-module common-leg architecture [9], combined with a variable

gain LNA. All the desired digital and analogue functionality are integrated into the same (mixed-signal) circuit, thanks to the use of SiGe. Besides, it can be fully controlled via a digital bus.

As common-leg of the T/R-module, the TRM-ICC has a double function. In transmit mode operates as a pre-driver for the amplification stage, while it applies the required phase-shifting. In the receive mode, it performs a low-noise amplification, which can be controlled in the imaginary plane, in order to produce the desired amplitude weighting and phase-shifting. The operational behaviour of the T/R-module can be described as follows:

- In transmit mode, the TRM-ICC performs a relatively small and constant amplification (about 10 dB), and applies the chosen transmit phase-shift. The signal is delivered to the parallel PAs stage, which are operated in saturation. After amplification, the signal passes through the HIS to the antenna port, while keeping approximately 33 dB of isolation to the receive port of the TRM-ICC.

- In receive mode, the HIS changes the signal path to the TRM-ICC receive port. The PAs outputs are isolated from the TRM-ICC receive port and the antenna side, with about 33 dB and 50 dB, respectively. Simultaneously, the TRM-ICC amplifies the received signal (with a maximum gain of about 30 dB), performs the desired phase-shifting and amplitude weighting and minimizes the signal at the PA's inputs.

Looking for a plain, space efficient and inexpensive circuit, the module is implemented as a double layer PCB on RO4003 material (where all the RF signals are kept on the top layer), shown in Fig. 3.8. Since the PCBs are mounted on top of the S-band waveguide and the top plane of the PPW, isolation lacquer has been applied to the bottom layer, but exclusively on the top of the DC lines.

This T/R-module implementation represents a technological challenge, since experimental RFICs and COTS components are bring together. In addition, the development needs to consider mass production aspects, modularity and maintain a plain implementation. This development covers several areas of expertise: electromagnetic & microwave design, circuit-design theory & practice and self-innovation.

The first module prototype produced is fabricated with vertical SMA ports, instead of monopoles. The matching between the vertical port and the

shielded-microstip is evaluated by full-wave simulations, in order to design a well matched transition, which at the same time preserves the performance when monopoles/probes are used.

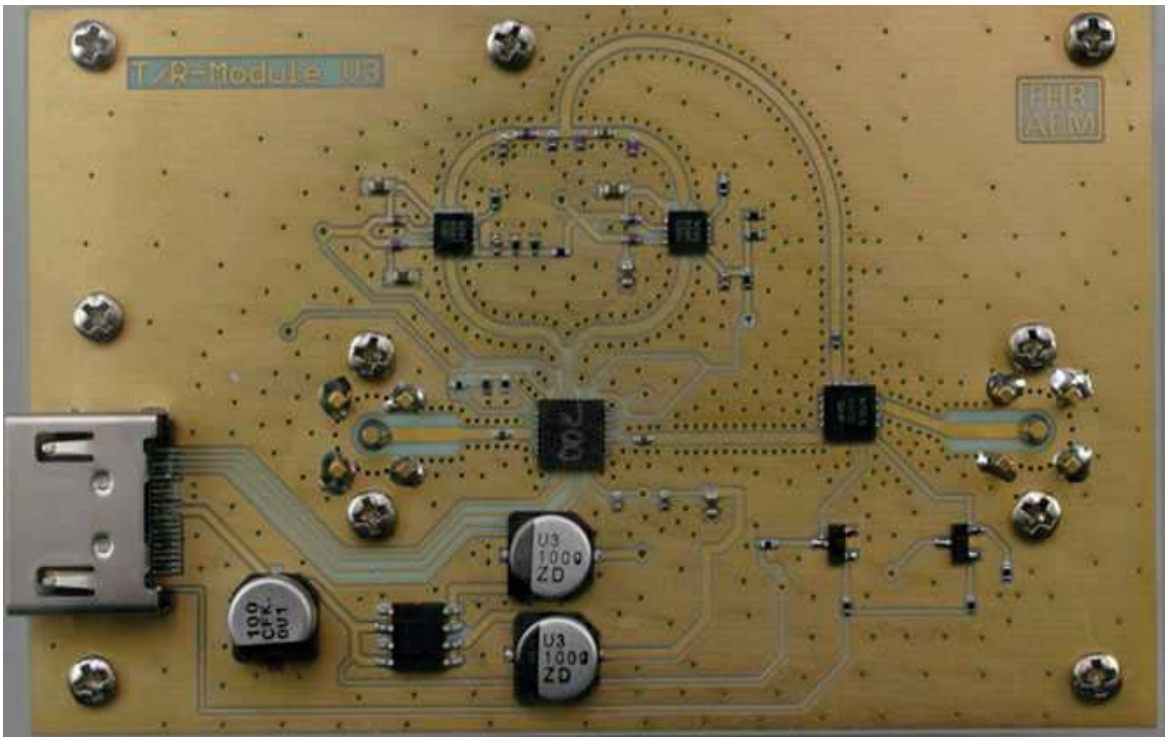


Figure 3.8: Top view photograph of the double-layer T/R-module PCB. All the RF lines are implemented in CPW or shielded microstrip. Apart from the TRM-ICC and the HIS, all the remaining elements are COTS components.

The successive modules are produced to be directly installed into the front-end, therefore, they are manufactured with monopole transitions. This way, the manipulation of the modules is reduced to a minimum from the fabrication to the front-end installation. With this purpose, a dedicated test-bed structure is designed and produced, in order to ensure the proper functionality of each individual T/R-module after fabrication (and before installation into the phased-array antenna). The structure is explained with detail in section 3.3.1.

The performance of presented prototype is satisfactory, as depicted in Fig. 3.9 by the measured phase/gain-map (PGM) of both modes. The maximum gain in receive mode is above 30 dB, and a *gain-circle* of 24.9 dB can be obtained. In transmit mode, the maximum output power, approximately 21.1 dBm, is guaranteed within an input power range of $[-10, +5]$ dBm

in almost all the states.

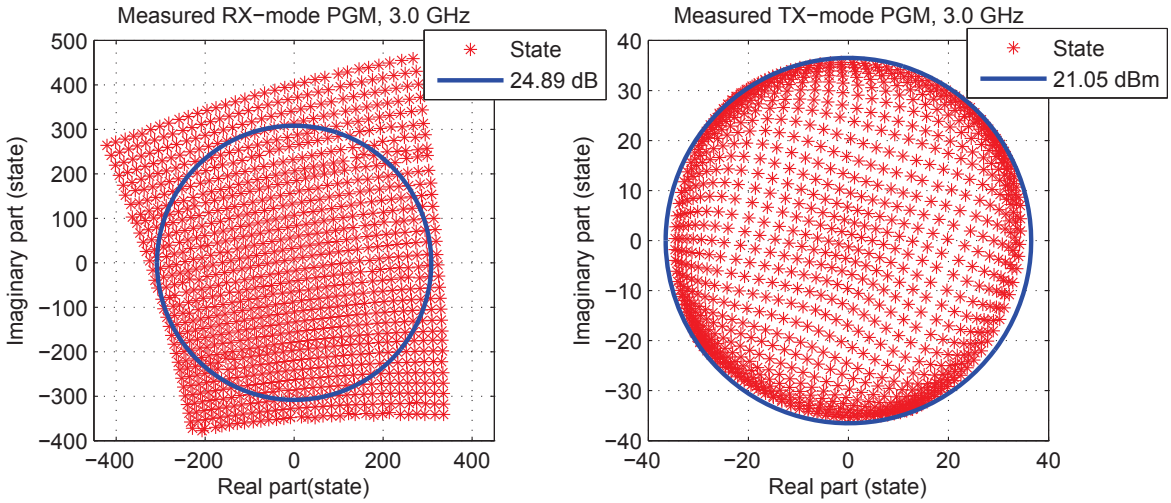


Figure 3.9: Measured T/R-module PGM at 3.0 GHz. In receive-mode (left) the linearity is preserved, while in the transmit-mode (right) saturation is present.

The presented T/R-module measurement results proof the reliability of the challenging TRM-ICC. In addition, it is also demonstrated the inexpensive approach towards *low-cost* T/R-modules based on COTS components and inexpensive solid-state semiconductor circuitry.

Besides, the development of this prototype can be used as a platform for future T/R-module generations, based on an improved SiGe chip-set with a higher integration level. Hence, it is expected that the overall module costs can be greatly reduced, since a higher integration will contribute to reduce the off-chip components and the PCB complexity.

3.3.1 T/R-module test-bed

As explained in the precedent paragraphs, every T/R-module has the same monopole length on the aperture side, but a different monopole length on the feeding side. *A priori*, this means that every module needs a dedicated test circuit to perform the functional tests before installation into the front-end.

The electrical length of the monopoles in the feeding side covers a large range, from approximately 12 mm to 24 mm, which is nearly one λ_g inside a standard S-band rectangular waveguide at 3.0 GHz. However, a hollow waveguide configuration that allows to test every T/R-module in the same structure is presented. The design steps of both transitions are explained.

Aperture side transition

The starting point for the design is based on an ideal TE_{10} steerer, which is designed for the common port of the feeding network. The mode steerer is a probe placed in the centre of an S-band rectangular waveguide, which is short-circuited in one extreme, oriented parallel to the narrow walls. The distance and the length are optimized to excite the fundamental TE mode.

The aperture's monopole, which is slightly longer compared to the mode steerer, is placed again in the waveguide's centre. The transition is shown in Fig. 3.10. As an initial state, the distance to the short-circuiting wall (upper wall on the image) is the same as it is in the antenna's PPW, which is feeding the aperture.

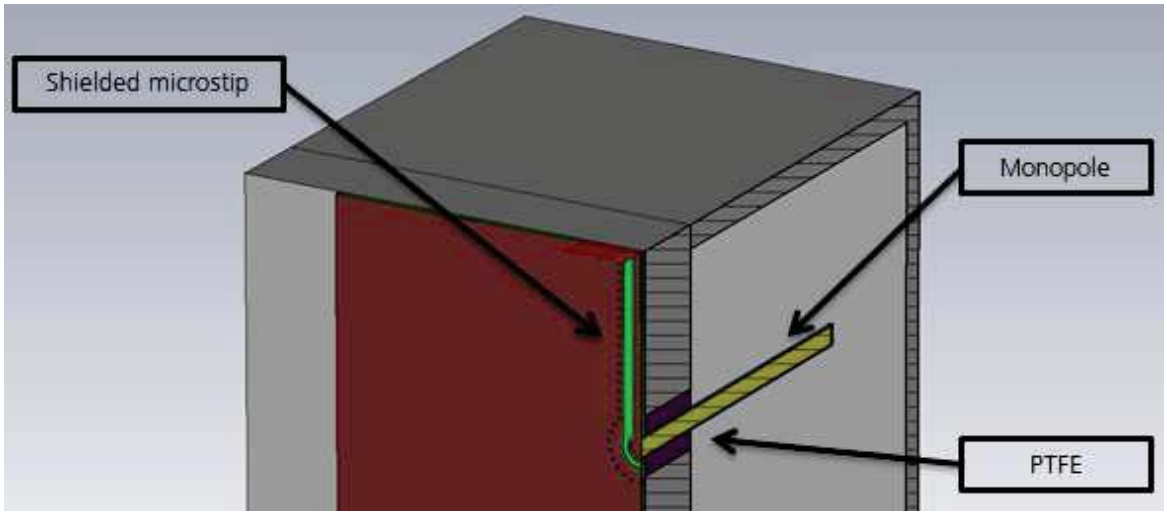


Figure 3.10: Snapshot of the initial transition (axial cut). The monopole's length is the same as in the real antenna. The distance to the short-circuit (upper wall on the image) is the same as in the PPW of the antenna demonstrator.

Unfortunately, at the central frequency (3.0 GHz) this transition is not well-matched: when looking at the Smith chart, the inductance is larger than zero and the real part is not one. The excess of inductance can be compensated by increasing the capacitive coupling of the probe/monopole to the waveguide narrow walls. This can be achieved by introducing any (malleable) material with low losses and relatively high permittivity inside the waveguide. In this case PTFE ($\epsilon_r \approx 2.1, \tan\delta \approx 2.8 \cdot 10^{-4}$) is chosen, since it is also being employed to hold the monopole/probe inserted into the waveguide (see Fig. 3.10).

The variations in the real part can be controlled with two mechanisms, as shown in [76]: moving the probe/monopole along the propagation direction of the mode inside the waveguide, and covering (partially) the probe/monopole by extending the dielectric inside the transition (which in this case is PTFE).

The distance between the two transitions cannot exceed the distance between the probe and the monopole of the T/R-module. Consequently, the transition's distance to the wall should be kept as small as possible. The fabricated transition is shown in Fig. 3.11.

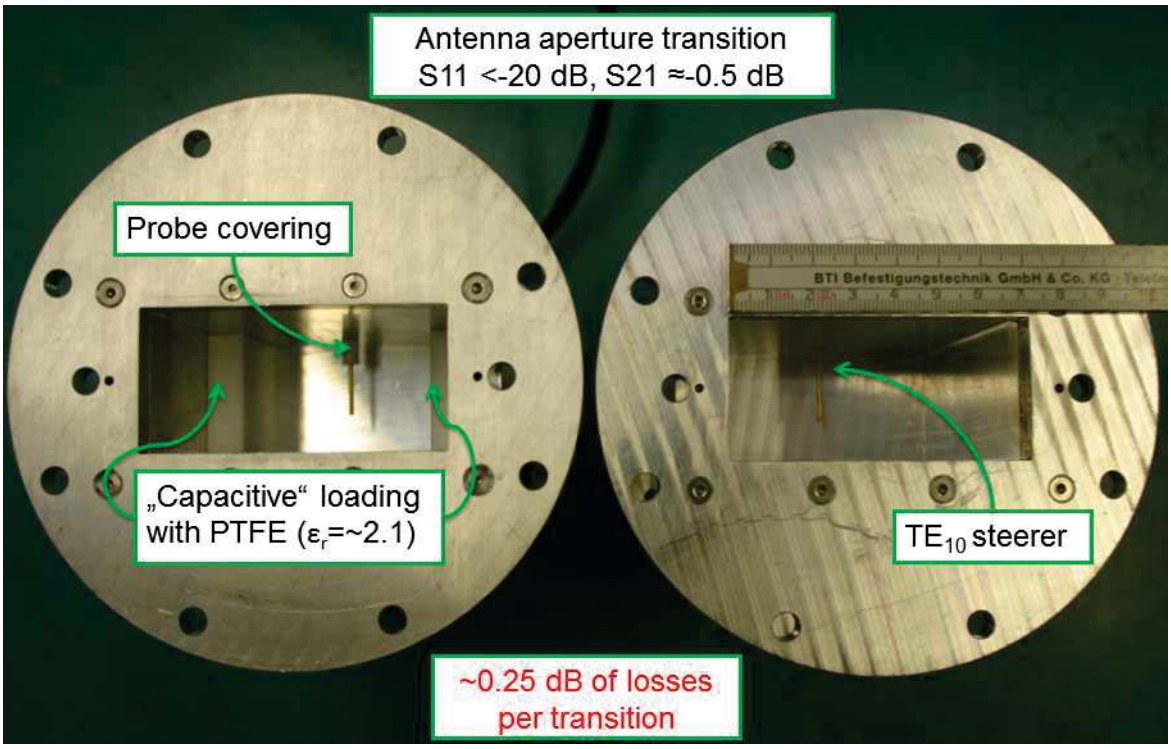


Figure 3.11: Photograph of the hollow waveguide test-bed interior, showing the aperture transition (left) and the TE_{10} steerer (right).

Feeding side transition

A similar concept can be applied in the feeding side transition design. This transition offers two situations, which are very different from a electrical point of view. In the first case, the probe is shorter, therefore, the transition is less inductive. In the second case, the probe is longer, consequently, the transition is more inductive. Typically, a compromise solution can be found, if the electrical range from the shortest to the longest probe is small. In

this particular case, the electrical length difference between the two probes is approximately λ_g inside the rectangular waveguide.

In a first design step, the transition with the probe monopole is compensated by adding more filling (PTFE) on the waveguide narrow walls, and slightly adjusting both, the distance to the short-circuit and the PTFE cylinder insertion length.

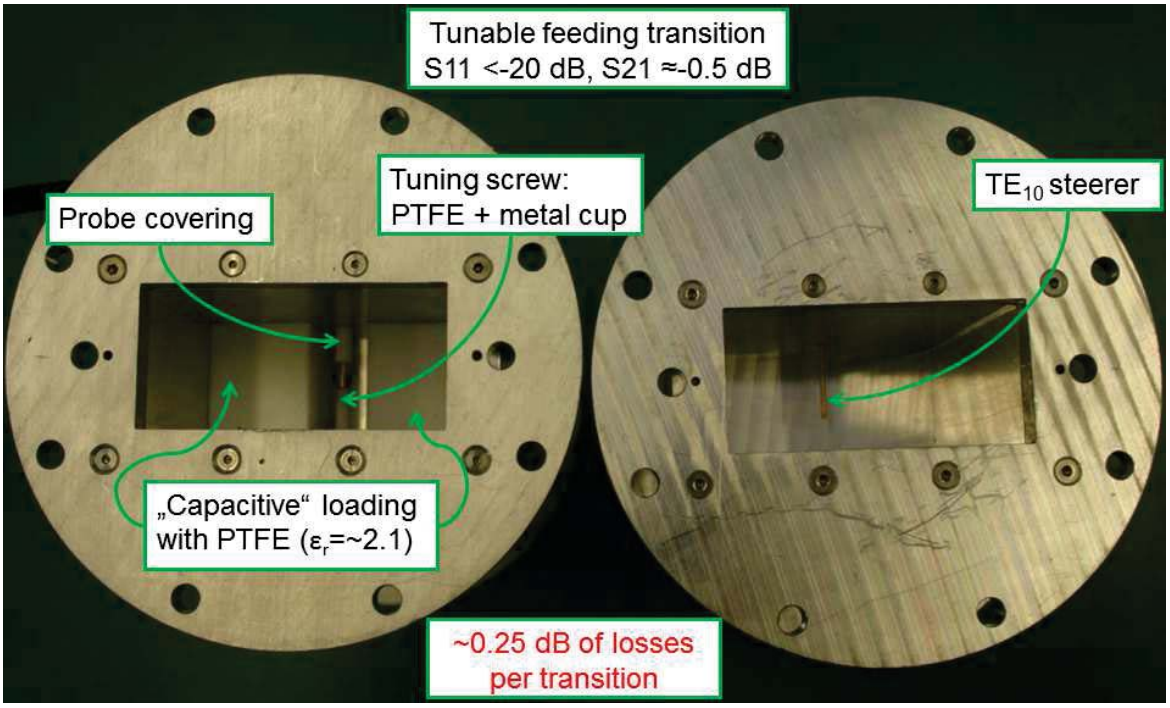


Figure 3.12: Photograph of the hollow waveguide test-bed interior, showing the feeding transition (left) and the TE_{10} steerer (right).

In the next design step, this second transition can be again simulated, but replacing the longest probe by the shortest. As it can be expected, the transition becomes less inductive. This lack of inductance can be compensated by increasing the electrical length of the probe, which can be done with a tuning screw.

The tuning screw is implemented in PTFE material. The screw's core is perforated, in such a way that different length copper probes can be inserted. In order to guarantee a good electrical contact between the screw's probe and the feeding's probe, each of the screw's probes has a metal-cup on top. The length of the probes is obtained by full-wave simulations.

Hence, accordingly to the length of the feeding network transition probe, exclusively the metal-cup of the tuning screw needs to be exchanged every

time that a T/R-module is placed on the test-bed. Consequently, a single test-bed structure can be employed. A photograph of the fabricated transition can be seen in Fig. 3.12.

Complete hollow waveguide test-bed

The two transitions can share a electrical short-circuit in the waveguide test-bed, which is similar to the front-end configuration. The thickness of the wall is adjusted in such a way that the same T/R-module distance between the probe and the monopole is obtained, despite of the significant difference with the final configuration. A photograph of the resultant test-bed, with a T/R-module installed, can be observed in Fig. 3.13.

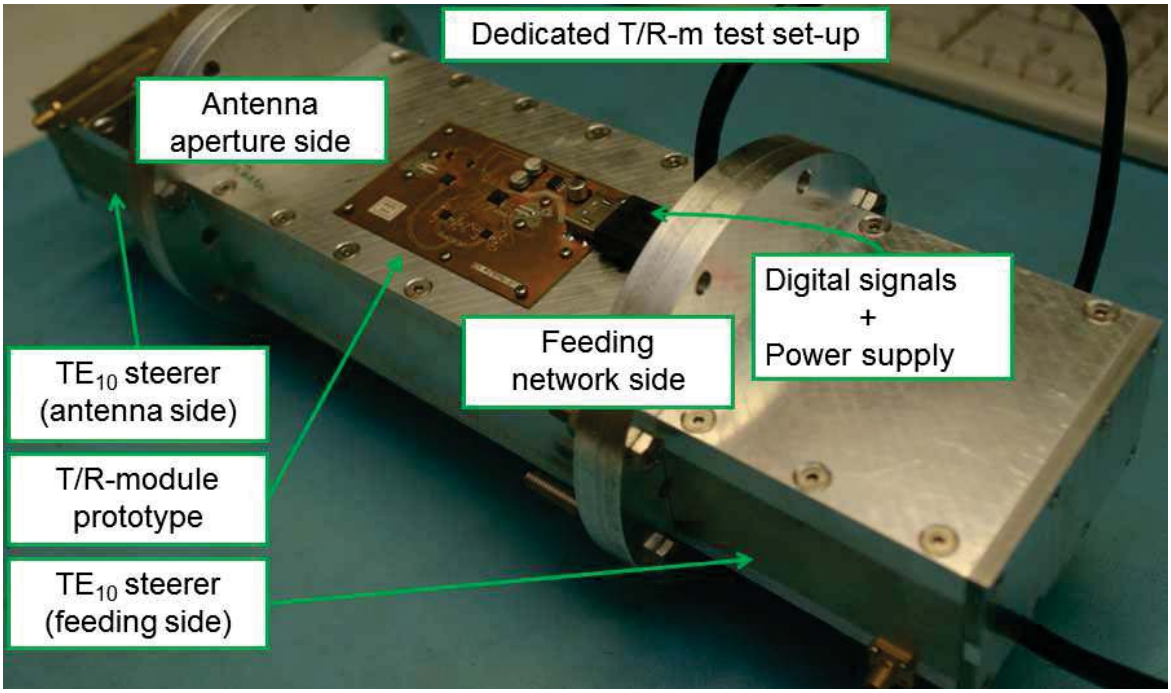


Figure 3.13: Photograph of the hollow waveguide test-bed with the first T/R-module prototype installed. The T/R-module is interfaced with a HDMI cable.

The test environment is validated by measurements with several passive PCBs mounted on top of the waveguide. The PCBs are identical shielded microstrip lines with the corresponding transition to monopoles/probes. In one side of the PCBs, the transition are identical, since probes with equal lengths are soldered (as the monopoles of the antenna aperture). In the

other transition, the probes are different, since they have different lengths, accordingly to the length range obtained in the feeding network design.

The circuit is measured with a VNA, in order to obtain the scattering parameters of the test-bed for the several different monopole-to-probe configurations. The measurement results at the central frequency (3.0 GHz) are summarized in Table 3.1. In all configurations, the matching of both transition is always about -25 dB or lower.

Table 3.1: Test-bed validation with passive PCBs, f_c=3.0 GHz

Length(mm)	S_{11}(dB)**(Feed)**	S_{21}(dB)	S_{12}(dB)	S_{22}(dB)**(Apt.)**
12	-24.85	-1.01	-0.99	-31.78
14	-28.67	-0.99	-0.99	-32.40
16	-33.92	-0.97	-0.99	-29.87
18	-30.18	-0.99	-1.00	-30.92
22	-30.19	-0.96	-0.98	-27.29
24	-33.03	-1.03	-1.03	-29.89

The measurements' calibration plane is at the SMA ports, observed in Fig. 3.13, and their effect is included into the measurement. This cannot explain the relatively high insertion loss ($S_{21} \leftrightarrow S_{12}$) measured. However, this is an *a priori* expected result. The presence of four transitions is observed in Fig. 3.13, going from left to right:

1. SMA port + waveguide TE_{10} steerer
2. Antenna-side monopole of the T/R-module
3. Feeding-side probe of the T/R-module
4. SMA port + waveguide TE_{10} steerer

In total, these four transitions, together with the microstip lines, offer about 1 dB of insertion loss. The experience with similar devices says that, typically, an SMA port to *strip* transition at 3.0 GHz offers an insertion loss in the range of $0.20 - 0.30$ dB [77]. Therefore, every of the transitions is responsible of about 0.25 dB in average, which is more than a successful result with this technology at this working frequency range.

3.4 Front-end assembly summary

The integration of all front-end parts, in order to complete a reliable AESA antenna, has been explained in the precedent paragraphs. The following lines summarize and describe the milestones of the design and implementation, in order to provide a more compact view of the complete process.

Antenna aperture. The antenna aperture is implemented as a flared PPW feed by an array of monopoles, which are sharing the non-flared part of the PPW. The concept of shared aperture produces a plain aperture implementation, although, it represents an extra electromagnetic complexity. However, the proposed design method, supported by full-wave simulations, guarantees an adequate aperture response, which is validated by measurement results.

Feeding network. A standard S-band waveguide is used as basis to implement a series feeding network, which will take advantage of the concept described in Chapter 2. Consequently, there is no isolation mechanism between antenna ports and the RF network is not inherently matched. The use of such an unique and novel feeding network in an AESA antenna imposes several scientific challenges, detailed in Chapter 4 and Chapter 5, which are successfully addressed.

T/R-module. Typically, the implementation of mixed-signal PCBs, in combination with experimental chip-sets, demands an extra design effort, since analogue and digital signals are sharing place and/or are very close to each other. In addition, when RF signals are also present, the level of complexity is increased as well, again due to the shared place and different signals proximity and electrical ground types. Those factors regularly lead to complex, and therefore costly, T/R-module implementations. Nevertheless, a plain, reliable, repeatable and easy to fabricate module is developed.

FPGA controller. The implemented FPGA controller is designed to use the lowest amount of resources possible. In addition, a reliable and efficient implementation with low-jitter is achieved. Only the 10% of FPGA resources are used to control 10 T/R-modules. In addition, this controller uses one mixed-signal omnibus (bus) per T/R-module, since the TRM-ICC does not

allow bus sharing. However, since bus sharing is to be supported by next MMIC generation, a very low number of logic functions is required to control a significantly large number of modules. This means that the amount of FPGA resources to control a complete system formed by four front-ends (each of them with approximately 100 elements) is going to be in the same order of magnitude.

Complete front-end assembly. A photograph of the assembled AESA antenna demonstrator can be observed in Fig. 3.14. The electronics (included the FPGA-board) required to power and control the complete front-end are placed in the box below the flared PPW. The modules are placed on top, as they were in the test-bed. It can be seen that the PPW is covered with a thick polyethylene layer (left-side of the photograph). Besides, a polyethylene stick, that is placed at the edge of the horn structure (right-side of the photograph), gives mechanical stability to the assembly.

In a first set-up, both sides of the demonstrator are completely covered with polyethylene planes. Those layers disturb more than expected the field at the aperture (this is further explained in Chapter 5), which motivates the configuration currently shown in the photograph. In the next chapter (Chapter 4), it is shown the calibration process based on near-field measurements, and those layers are still present. System performance might be affected, whereas the calibration and beam-forming techniques are not influenced by this fact.

The indicated design and implementation steps followed in the front-end development, allow to obtain a reliable demonstrator. Therefore, this phased-array antenna can be used as a platform for the scientific achievements presented in the following chapters. In addition, it is a proof of concept for the inexpensive AESA antenna proposed, which is exclusively based on inexpensive and standard existing technologies.

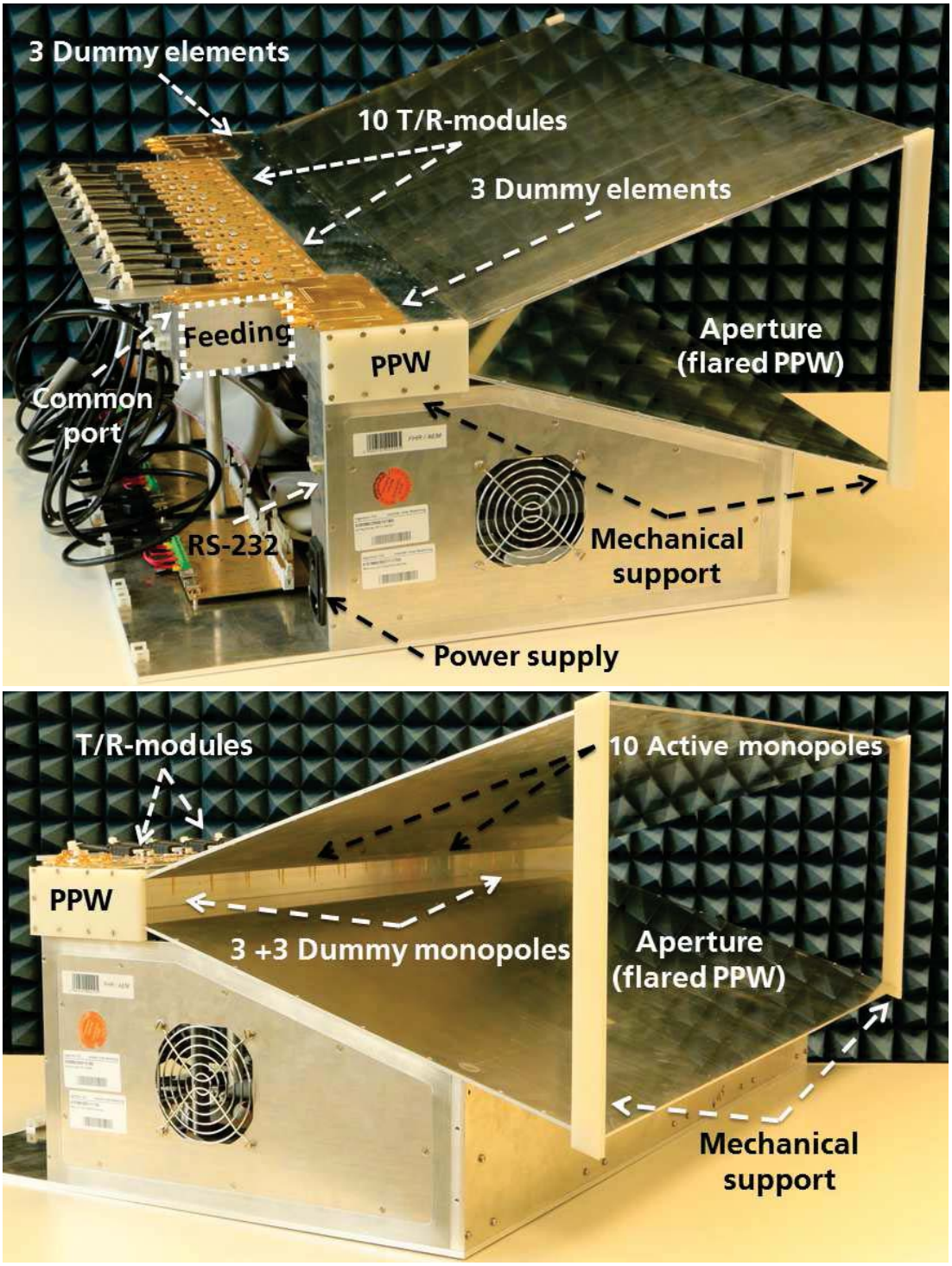


Figure 3.14: Photographs of the back/left-side (top) and the front/left-side (bottom) of the manufactured ten element S-band AESA antenna. The antenna's power supply and the digital control unit of the modules are enclosed in the metallic space below the antenna.

Chapter 4

Near-field based diagram synthesis

Firstly, this chapter introduces a novel calibration approach, applied to the previously presented AESA antenna demonstrator, which is based on near-field measurements, resorting to a near-field antenna radiation numerical model. This radiation model (off-line calibration), in combination with full-wave simulations, allows to solve the (far-field) beam-forming problem by enforcing the proper near-field in the aperture.

Secondly, a near-field to far-field transformation, including probe compensation, is explained with detail. The far-field radiation patterns of the AESA antenna are predicted by means of this transformation. For demonstration purposes, calibration, beam-forming and the resulting array radiation patterns are executed, measured and calculated at the central frequency of the operational band, 3.0 GHz.

Finally, the accuracy of the near-field measurement set-up, the beam-forming principle and the calibration process are discussed and analysed.

4.1 Beam-forming technique introduction

The concept of beam-forming, or pattern/diagram synthesis, refers to the calculation of the optimal excitation of an antenna array, which reproduces a given far-field radiation pattern (reference pattern). In case that the given far-field cannot be physically realized, the antenna excitation should be calculated to reproduce as good as possible the reference pattern.

Furthermore, diagram synthesis can offer several degrees of freedom to access the task. One option to tackle the open problem is the use of pseudo-inverse/Least Mean Square (LMS) algorithms [78], [79]. There are many other techniques which also solve the diagram synthesis of planar arrays gracefully, such as the Dolph-Chebysev method or the Elliot's Modified Taylor Pattern method, among other approaches [10], [32], [48]. Typically, any *standard* diagram synthesis approach, in combination with adaptive methods can provide very successful results [80], [81].

In a *standard* phased-array antenna configuration, like the one presented here, the single radiating antenna elements are not isolated any more. Thus, the radiation of every element is disturbed by its own neighbours. Therefore, mutual coupling effects need to be taken into account to determine the optimum antenna weights [32, 48, 57, 68, 69].

In Chapter 3 it is shown how the mutual coupling can be introduced in the aperture's design, and guarantee a low active reflection coefficient at the antenna elements feeds. In addition, it is shown that the presented technique avoids blind-spots and obtains a successful antenna gain, once the phased-array is fully excited. Moreover, the radiation pattern of the single antenna elements is numerically approximated, assuming an infinite size antenna array [57]. Even though it is sufficient to estimate the overall phased-array radiation pattern performance, in order to achieve a successful beam-forming, it is necessary to consider the effects of mutual coupling between the antenna elements in the horizontal far-field radiation pattern. This process is referred as off-line calibration.

In the case of large phased-array antennas, with several hundreds, even thousands, of elements, like the Captor-E AESA antenna mounted on the Eurofighter [82], it can be assumed that most of the elements, but not the one on the edges, behave in a similar way. Therefore, only a small portion of the elements in the aperture needs to be characterized, since the possible small differences are assumed to compensate each other, if not completely, at least sufficiently.

In the case of small to medium-sized phased-array antennas, with no more than a few dozens of radiating elements, the beam-forming approach needs to be different. The behaviour of each individual active antenna can vary significantly from element to element. Consequently, an *auto*-compensation of (not any more small) differences and errors cannot be expected. Actually, the off-line calibration might need to measure even more elements than in a considerably larger antenna.

Furthermore, the operational AESA antenna here presented has two more inconveniences:

1. It has large physical dimensions (about 6 meters in the horizontal plane), thus, it is complicated to perform a far-field calibration with conventional techniques, by measuring every single antenna element in an anechoic chamber

2. The antenna ports of the feeding network are highly coupled, and if every antenna element is operated separately, it can be expected that the measurement results will be strongly disturbed

In addition, and as justified later, it is not possible to analytically determine a feasible, from the physical point of view, reference near-field of the antenna array. Consequently, the off-line calibration, necessary for the beam-forming, becomes a problematic task.

However, it is proposed to solve the diagram synthesis in a straightforward approach, by using an antenna's near-field radiation model, supported by full-wave simulations of the phased-array. This way, despite of the inherent difficulties described, calibration and beam-forming can be successfully completed.

4.2 Near-field radiation model

The calibration and beam-forming approaches proposed here are based on near-field measurements, whereas the aim is the far-field radiation pattern for several main-beam directions. For this reason, a near-field to far-field transformation is used later-on to predict the radiation patterns.

The near-field measurement set-up of the manufactured demonstrator and its sketch are shown in Fig. 4.1. Three main objects are depicted: an absorber wall, the AESA antenna demonstrator itself and a horizontal mechanical scanner including a probe antenna, which is a custom-made printed dipole.

Moreover, in Fig. 4.1 (right) it can be observed that the sides of the demonstrator's horn structure are covered with polyethylene layers. Within the calibration process it is encountered that those layers disturb more than expected the aperture's field. For that reason, a different configuration with similar mechanical stability is chosen, as shown in the photograph in Fig. 3.14 (Chapter 3). This exclusively affects the radiation pattern performance, but does not have any influence on the calibration or beam-forming methods.

The E-plane horn structure needs to be terminated on its edges, in order to ensure the front-end's mechanical stability. This inherently forces a large electrical distance between the probe and the radiating sources, which is about 5λ. Consequently, the field sampled by the probe is not dominated by the nearest array element, and it is a combination of the several interactions between the antenna elements and the aperture itself.

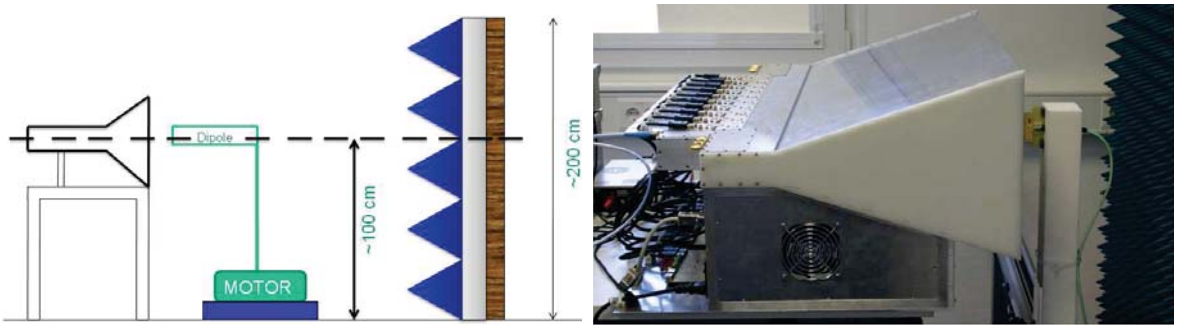


Figure 4.1: Left: schematic of the near-field measurement set-up, side-view. The motor on the image moves the probe in perpendicular direction to the image plane. Right: photograph of the antenna demonstrator is shown. The FPGA which controls the antenna, the main power supply and the PCBs for signal distribution are enclosed in the box integrated below the front-end.

The field generated by the aperture at the probe's measurement plane is obtained from full-wave simulations. The antenna array is optimally excited to obtain the desired far-field, and its corresponding near-field aperture's distribution is acquired. In addition, the full-wave simulation can include the complex electromagnetic problem, comprising the flared PPW, the 10 antenna elements, as well as the 3 dummies and the polyethylene walls. Moreover, the interest of the simulation is on the radiation mechanism, therefore, a full-wave simulation with reduced accuracy can be used, resulting in a calculation time in the range of hours with conventional computers.

In the transmit case, a constant aperture illumination is required, producing a radiation pattern SLL of approximately -13 dB, for all main-beam angles. On the contrary, a low SLL is required in receive mode, which is to be achieved by means of a Taylor aperture distribution. This is considered in the full-wave simulation, and the antenna is steered with the ideal array factor weights that reproduce the required radiation pattern constraints.

As mentioned above, the steering of the antenna in the full-wave simulation is done with the optimal solution of the beam-forming problem. The

calculation of the weights can be done analytically, nevertheless, with the given measurement set-up and the given AESA antenna architecture, there is no straightforward method to relate the antenna excitation and the radiated field.

In this situation, it is proposed an innovative approach to solve the near-field (off-line) antenna calibration. The aperture's field at the probe's position and the antenna weights can be related with a numerical model. The resulting antenna calibration can be used to solve successfully the beam-forming problem, which in this case is done based on pseudo-inverse/Least-Mean-Square (LMS) algorithm. Following, the proposed numerical model of the off-line calibration is explained.

The electric field produced by every antenna element, at every single probe's position in front of the aperture (see Fig. 4.2), can be defined as follows:

$$E_{n,m} = \alpha_m \beta_{n,m}, \tag{4.1}$$

where:

- n: discrete probe position in the aperture
- m: single antenna element
- α_m: PGM state of the m-th element
- $\beta_{n,m}$: propagation from the source point to the (discrete) probe position

Unfortunately, it cannot be determined the module state, α_m, which produces the sampled field, $E_{n,m}$, since the propagation factor, $\beta_{n,m}$, is unknown and different for every antenna element with respect to every probe position. This *a priori* undetermined problem can be solved in a plain way.

Firstly, the following aperture's field reference measurement is defined:

$$E_{ref,n,m} = \alpha_{ref,m} \beta_{n,m}. \tag{4.2}$$

Secondly, the unknown factors $\beta_{n,m}$ can be expressed as a function of eq. (4.2). Then, eq. (4.1) resorts to:

$$E_{n,m} = \alpha_m \frac{E_{ref,n,m}}{\alpha_{ref,m}}. \tag{4.3}$$

Thirdly, the expression in eq. (4.3) can be formulated differently:

$$E_{n,m} = E_{ref,n,m}\alpha_m^{'}, \tag{4.4}$$

where $\alpha_m^{'} = \frac{\alpha_m}{\alpha_{ref,m}}$. It is assumed that this way the effects of the strongly coupled antenna ports are, if not completely removed, at least significantly mitigated. The values of $\alpha_{ref,m}$ and $E_{ref,n,m}$, as well as the set of possible α_m values, can be obtained by the near-field measurement set-up. These sets of T/R-module states are previously referred as PGMs, and the $\alpha_{ref,m}$ can be chosen to be any state of the mentioned maps, but it has to be the same for all the modules. This allows to assume that it has a identical response for all the elements.

Finally, the field at the aperture can be written in matrix form generalizing eq. (4.4):

$$E_n = \underline{E}_{ref,n}\underline{\alpha}^{'} \Rightarrow \underline{E} = \underline{\underline{E}}_{ref}\underline{\alpha}^{'}. \tag{4.5}$$

In this way, by means of direct measurements it is obtained a relation between the near-field produced at the antenna, $\underline{E}$, by a certain excitation vector, $\underline{\alpha}$, as the antenna's reference near-field, $\underline{\underline{E}}_{ref}$. Besides, the effects of the strongly coupled ports are to be mitigated, or even removed. This resorts to an off-line calibration, that allows to predict the near-field radiation of the antenna.

Once the off-line calibration of the antenna is completed, the beamforming algorithm can be applied. It is assumed that a (targeted) near-field distribution, which produces a scanned far-field, $\underline{E}(\theta_0)$, is known. It can be obtained the desired, $\underline{\alpha}^{'}$ by pseudo-inverse:

$$\underline{\alpha}^{'} = \underline{\underline{A}}\ \underline{E}(\theta_0),\ \textit{where}\ \underline{\underline{A}} = \underline{\underline{E}}_{ref}^{T}[\underline{\underline{E}}_{ref}\underline{\underline{E}}_{ref}^{T}]^{-1}. \tag{4.6}$$

The following step is to obtain the discrete T/R-module excitations, that would produce an equivalent/similar solution as the continuous excitation $\underline{\alpha}^{'}$. The algorithm is explained with detail in section 4.4. The desired far-field can be calculated by means of a near-field to far-field transformation, which is explained in the following paragraph.

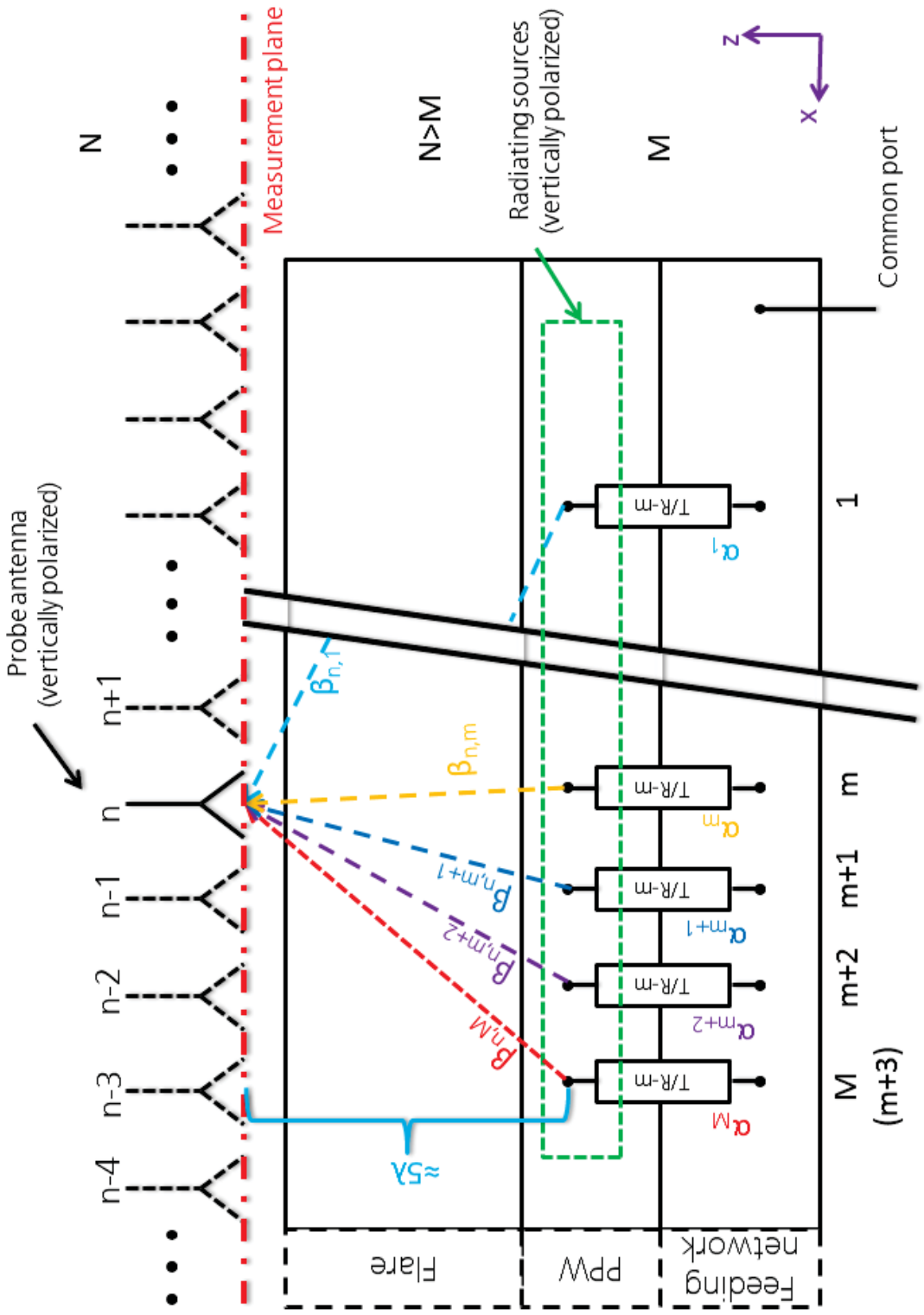


Figure 4.2: Sketch of the near-field calibration problem. It can be observed different magnitudes and parameters, which are used to establish a relation between the antenna weights and the near-field at the measurement plane.

4.3 Near-Field to Far-field transformation

Before presenting the beam-forming algorithm, section 4.4, the near-field to far-field (NF/FF) transformation method should be explained with detail. This is necessary to facilitate the understanding of the complete beam-forming process, as well as the later discussions.

The proposed pattern synthesis approach is based on the near-field distribution of the aperture, whereas the aim is a given far-field radiation pattern. The straight forward solution is to apply a NF/FF transformation to the near-field distributions measured [83]. Besides, a transformation comprising a simple probe correction [84], which assumes no interaction between the probe and the antenna under test (AUT), can be chosen. The mentioned probe correction neglects possible interactions with the AUT, and only eliminates the effect of the probe's radiation pattern.

The analytical demonstration of the probe correction in [84] is not given. However, by means of the methods presented in [85–88] complete analytical demonstration of the transformation (comprising probe correction and computation schemes) can be derived. In the following lines, an analytical near-field to far-field transformation comprising probe correction is presented.

It can be assumed an electromagnetic source in space, whose electric field in the region free of sources (free-space, $z \geq z_0$) can be obtained from the plane-wave spectrum representation [89]:

$$\underline{E}(\underline{r}) = \frac{1}{2\pi} \int_{-\infty}^{+\infty} \int_{-\infty}^{+\infty} \underline{T}(k_x, k_y) e^{+j(k_x x + k_y y + k_z z)} dk_x dk_y, \;\; z \geq z_0, \tag{4.7}$$

where the propagation vector is $\underline{k} = k_x \hat{x} + k_y \hat{y} + \gamma \hat{z}$ and the position vector is $\underline{r} = x\hat{x} + y\hat{y} + z\hat{z}$. Besides, its spectrum, $\underline{T}(k_x, k_y)$, is defined as:

$$\underline{T}(k_x, k_y) = \frac{e^{-j\gamma z}}{2\pi} \int_{-\infty}^{+\infty} \int_{-\infty}^{+\infty} \underline{E}(\underline{r}) e^{-j(k_x x + k_y y)} dx dy, \;\; z \geq z_0. \tag{4.8}$$

Furthermore, the divergence of the electric field has to be zero. Consequently, the spectrum of the field has to satisfy:

$$\underline{T}(k_x, k_y)\underline{k} = 0. \tag{4.9}$$

The spectral components of the field are perpendicular to the propagation direction, thus for $\gamma \neq 0$ the component T_z can be determined from T_x and T_y. Then, the electric field in $z \geq z_0$ is given from its spectrum $\underline{T}(k_x, k_y)$.

In a later step it is shown that the spectrum can be obtained from the field at the measurement plane, $z = z_0$. It is demonstrated how the far-field can be expressed as a function of the field's pattern $\underline{F}(\theta, \phi)$, which in turn can be expressed in terms of the field at the aperture (planar surface field source). Firstly, the well-known Helmholtz equation is presented:

$$\nabla^2 \underline{E}(\underline{r}) + k^2 \underline{E}(\underline{r}),\ z > z_0, \tag{4.10}$$

where k is the propagation constant. Moreover, the electric-field whose tangential components satisfy the Helmholtz equation can be defined as:

$$\underline{E}(\underline{r}) = \frac{z - z_0}{2\pi} \int_{-\infty}^{+\infty} \int_{-\infty}^{+\infty} \underline{E}(\underline{r}_0) \left[jk - \frac{1}{R} \right] \frac{e^{jkR}}{R^2} dx_0 dy_0,\ z > z_0, \tag{4.11}$$

where $R = \sqrt{(x - x_0)^2 + (y - y_0)^2 + (z - z_0)^2}$ and $\underline{r}_0 = x_0\hat{x} + y_0\hat{y} + z_0\hat{z}$, as shown in [88], sec. 2.1.4, pag. 14-16.

The eq. (4.11) can be further manipulated, and the following expression for the electric far-field is obtained:

$$\underline{E}(\underline{r}) = \frac{1}{2\pi} \int_{-\infty}^{+\infty} \int_{-\infty}^{+\infty} \frac{e^{jkR}}{R^2} \left[jk - \frac{1}{R} \right] \underline{R} \times [\hat{z} \times \underline{E}(\underline{r}_0)]\, dx_0 dy_0,\ z > z_0. \tag{4.12}$$

A far-field approximation can be introduced in eq. (4.12), and the far-field pattern can be defined such as $\underline{E}(\underline{r}) \propto \underline{F}(\theta, \phi)\frac{e^{jkr}}{r}$. Hence, the far-field pattern, $\underline{F}(\theta, \phi)$, can be expressed directly from the spectral components of the field at the planar surface source:

$$\underline{F}(\theta, \phi) = \frac{+jk}{2\pi} \hat{r} \times \int_{-\infty}^{+\infty} \int_{-\infty}^{+\infty} \hat{z} \times \underline{E}(\underline{r}_0) e^{-jk\hat{r}\underline{r}_0} dx_0 dy_0,\ z > z_0. \tag{4.13}$$

This is demonstrated with detail in [88], sec. 2.2.1, pag. 18. Alternatively, an equivalent expression is derived in [83], approximating the electric field in the free-space region ($z \geq z_0$) from the angular spectrum of a planar surface field source.

Furthermore, making use of the identity:

$$\hat{r} \times (\hat{z} \times \underline{E}) = (\hat{r}\underline{E})\hat{z} - cos(\theta)\underline{E} = -cos(\theta)\underline{E}, \tag{4.14}$$

the far-field pattern is directly obtained from eq. (4.13) and the plane-wave spectrum in eq. (4.8):

$$\underline{F}(\theta, \phi) = -jk\ cos\theta\ \underline{T}(k\ cos\phi\ sin\theta, k\ sin\phi\ sin\theta),\ z > z_0. \tag{4.15}$$

All the required intermediate calculations, starting from the Helmholtz equation, are shown in [88], [90]. This way, it can be defined the far-field pattern of the planar surface field source as function of its spectral components, directly from the field at the measurement plane, $z = z_0$.

The last step is to remove the probe's effects from the measured field, assuming that the distance between the probe and the AUT is enough to avoid multiple interactions. Let us start defining the output (voltage) of the probe to an incident field:

$$\underline{s}_p = s_p^x \hat{x} + s_p^y \hat{y}. \tag{4.16}$$

Then, the response of the probe to an incident plane-wave at the origin, $\underline{r}_0 = 0$, is defined as:

$$\underline{s}_p = \underline{\underline{R}}_p(k_x, k_y)\underline{w}, \tag{4.17}$$

where the plane-wave is defined as $(1/2\pi)\underline{w}e^{j(k_x x + k_y y + \gamma z)}$, and satisfies the condition $\underline{w} \cdot \underline{k} = 0$.

Consequently, the probe's output at an arbitrary position, $\underline{r}_0 = x_0\hat{x} + y_0\hat{y} + z_0\hat{z}$, for the same incident plane-wave is:

$$\underline{s}_p = \underline{\underline{R}}_p(k_x, k_y)\underline{w}e^{j(k_x x_0 + k_y y_0 + \gamma z_0)}. \tag{4.18}$$

From [89] it can be said that in the direction (k_x, k_y) the component of the propagating plane-wave is $(a_0/2\pi)\underline{T}_0(k_x, k_y)e^{j(k_x x + k_y y + \gamma z)}dk_x dk_y$. Therefore, the response of the probe to this component can be written as:

$$d\underline{s}_p(\underline{r}_0) = a_0\underline{\underline{R}}_p(k_x, k_y)\underline{T}_0(k_x, k_y)e^{j(k_x x_0 + k_y y_0 + \gamma z_0)}dk_x dk_y. \tag{4.19}$$

Thus, assuming that the probe has a linear behaviour with respect to its incident fields, its output due to the same plane-wave component can be expressed as:

$$\underline{s}_p(\underline{r}_0) = a_0 \int_{-\infty}^{+\infty} \int_{-\infty}^{+\infty} \underline{\underline{R}}_p(k_x, k_y)\underline{T}_0(k_x, k_y) e^{j(k_x x_0 + k_y y_0 + \gamma z_0)} dk_x dk_y. \quad (4.20)$$

Then, the far-field produced by the planar surface (field source) can be obtained as function of the field measured by the probe at the surface, correcting the effects of the probe itself. This can be deduced in three steps.

First, we can use an inverse Fourier transform-like approach to obtain:

$$\underline{\underline{R}}_p(k_x, k_y)\underline{T}_0(k_x, k_y) = \frac{e^{-j\gamma z_0}}{(2\pi)^2 a_0} \int_{-\infty}^{+\infty} \int_{-\infty}^{+\infty} \underline{s}_p(\underline{r}_0) e^{-j(k_x x_0 + k_y y_0)} dx_0 dy_0. \quad (4.21)$$

Second, we can define the received spectrum at the probe's output as:

$$\underline{T}_0(k_x, k_y) = \frac{e^{-j\gamma z_0}}{(2\pi)^2 a_0} \underline{\underline{R}}_p(k_x, k_y)^{-1} \int_{-\infty}^{+\infty} \int_{-\infty}^{+\infty} \underline{s}_p(\underline{r}_0) e^{-j(k_x x_0 + k_y y_0)} dx_0 dy_0. \quad (4.22)$$

Third, recalling that $\underline{E}(\underline{r}) \propto \underline{F}(\theta, \phi)\frac{e^{jkr}}{r}$ and using eq. (4.15) together with eq. (4.22), we can obtain the electric far-field produced by the surface:

$$\underline{E}(\underline{r}) \propto cos\theta \underline{\underline{R}}_p(k_x, k_y)^{-1} \int_{-\infty}^{+\infty} \int_{-\infty}^{+\infty} \underline{s}_p(\underline{r}_0) e^{-j(k_x x_0 + k_y y_0)} dx_0 dy_0. \quad (4.23)$$

The validity of the expression in eq. (4.23) is obviously restricted to the free-space region, $z > z_0$. Moreover, this result is equivalent to the far-field pattern expression found in [84], which assumes as well no interaction between probe and AUT.

Significant interactions between the aperture and the probe should be taken into account. In this set-up the probe is relatively far away from the radiating sources, approx. 5λ. Therefore, the previously presented transformation can be applied since possible interactions can be considered negligible.

For validation purposes, the implemented transformation is compared against far-fields given by a full-wave solver, when applied to the near-field

distributions of the same full-wave simulations. Simulation results are shown in Fig. 4.3 for two representative examples of transmit and receive far-field patterns. A good agreement is obtained.

On the one hand, the space between samples, which makes the integration discrete, should accomplish the Nyquist sampling theorem in the k-space [87]. On the other hand, an excess of samples leads to long measurement times, while the length of the integration line has to be large enough: all the significant field contributions need to be sampled [87]. This demands a careful choice of the number and the space between samples, which is matter of discussion in section 4.5.1.

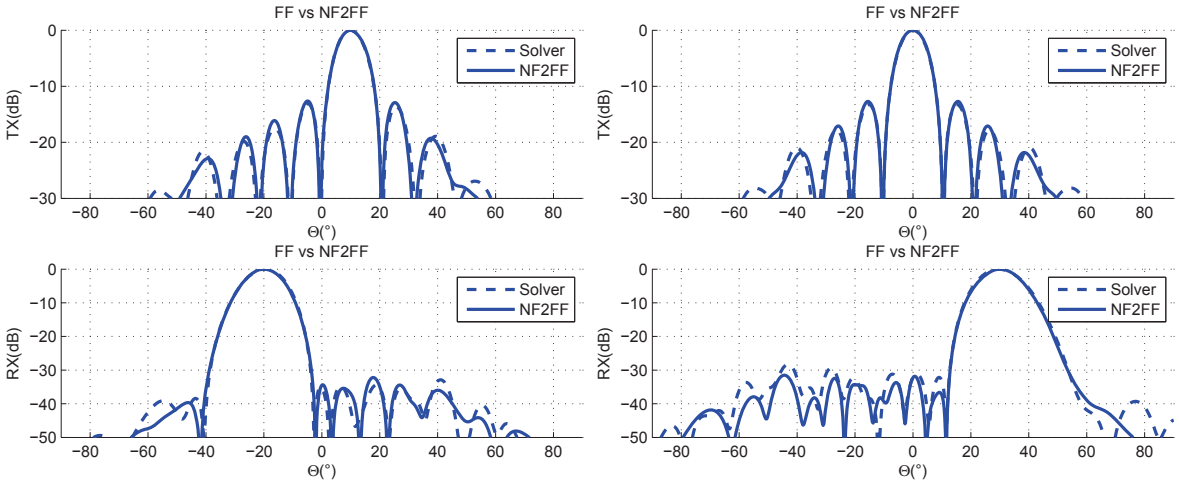


Figure 4.3: Comparison of far-field radiation pattern in transmit (top) and receive (bottom), obtained by the implemented NF/FF transformation and from the full-wave solver direct solutions.

4.4 Near-field based beam-forming

In this paragraph, it is explained how the discrete set of T/R-modules states are determined, in order to obtain the equivalent solution for the given near-field of the aperture, which produces the desired far-field, i.e.: the beam-forming algorithm is presented. In addition, experimental results are shown to demonstrate the validity of the method.

As mentioned before, once the continuous $\underline{\alpha}'$ weights are obtained, the next step is to obtain an equivalent solution from the discrete set of $\underline{\alpha}$ that can be generated by the T/R-modules, previously referred as PGMs. It has to

be considered that a small variation on any element of the excitation vector, $\alpha_m^{'}$, can produce a strong change into the near-field distribution. This is a consequence of measuring in the radiating near-field of the aperture, where the combination of the power radiated by every element is very sensitive.

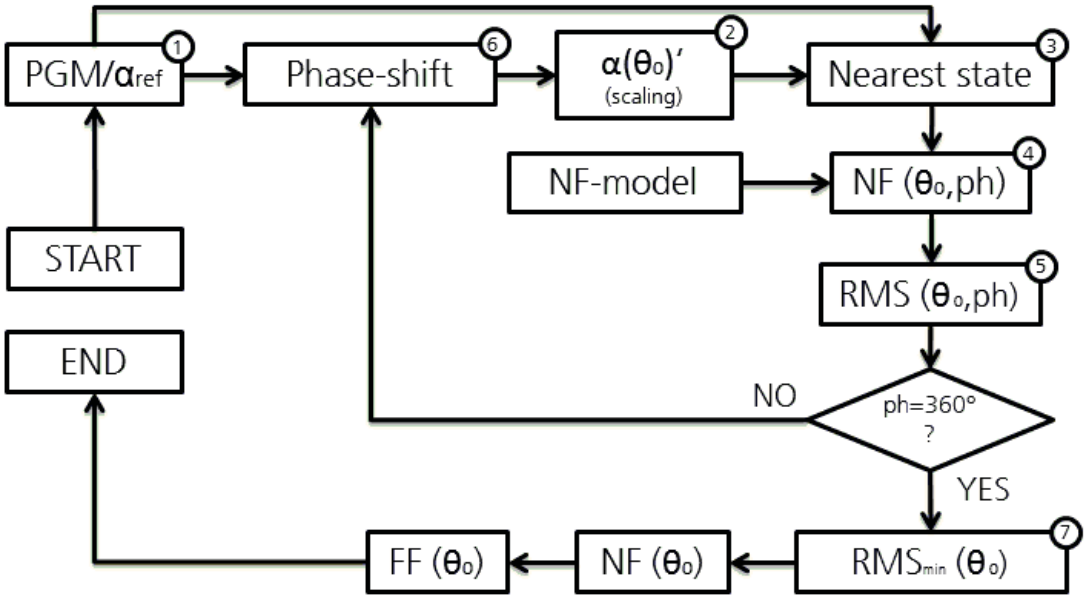


Figure 4.4: Determination of best α' for the desired main-beam angle, based on the near-field antenna radiation model.

The block diagram of the implemented process is shown by Fig. 4.4. It can be explained as follows:

1. Every PGM is normalized by its $\alpha_{ref,m}$
2. $\underline{\alpha}^{'}$ is scaled until all its values are contained in the normalized PGM
3. The nearest PGM states to the scaled $\underline{\alpha}^{'}$ are chosen
4. The near-field distribution produced by the chosen states is calculated
5. The average Root-Mean-Square (RMS) error of the calculated distribution is computed with respect to the reference distribution
6. A phase-shift, lower than the achievable phase resolution of the T/R-module, is applied to the $\underline{\alpha}^{'}$ vector and steps 2 to 5 are repeated
7. The distribution with the lowest amplitude-RMS error is chosen and its far-field is calculated

The RMS error is calculated with respect to the near-field, since the far-field contains *zeros* that produce spurious values in the calculation. Furthermore, it can be demonstrated that amplitude errors introduced by the selection of the PGM states tends to have a larger influence in the realized far-field, when compared to the effects due to a erroneous phase distribution. In addition, the phase errors are typically smaller, with respect to the amplitude errors. Consequently, the amplitude errors should be minimized by the beam-forming algorithm.

The set of weights obtained is used to predicted the aperture's near-field, which is then transformed to far-field using the method shown in the previous paragraph. The patterns predicted by the model exhibit, in general, the expected performance for both antenna modes and for all the main-beam directions. For validation purposes, the predicted far-field patterns from modelled near-field distributions, can be compared against far-field patterns obtained from directly measured aperture's near-field distributions.

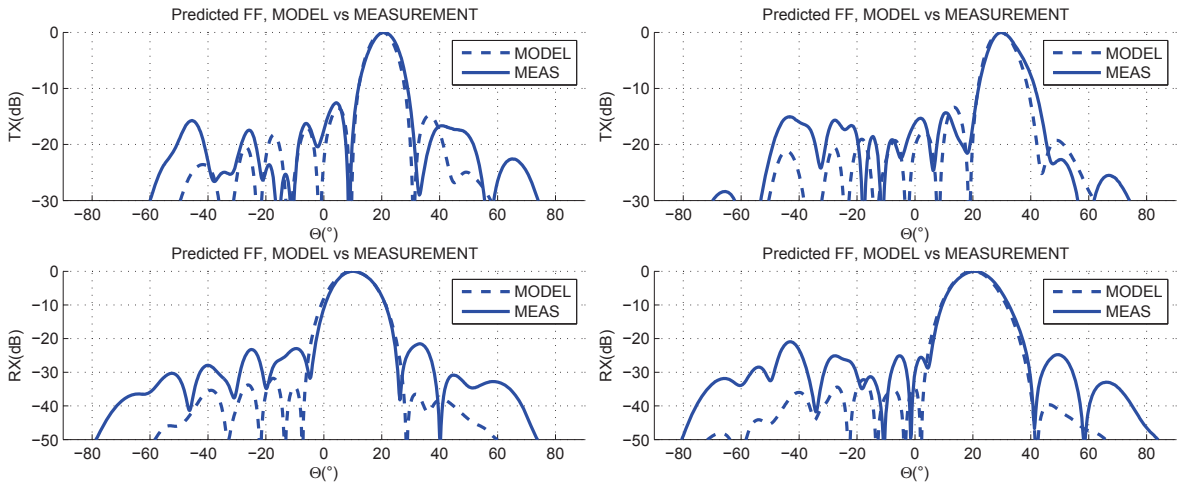


Figure 4.5: Comparison of normalized far-fields predicted by the near-field model and from measured near-fields, in transmit (top) and receive (bottom), for some exemplary angles. The model is not predicting properly the SLL, specially in the receive case, where more than 10 dB of deviation can be observed. However, successful predictions are obtained for the main-beam angle and the HPBW.

In Fig. 4.5 are compared predicted far-fields from measured near-fields and from near-fields predicted by the radiation model. It can be observed that the SLL as well as the pointing direction are not predicted by the model with high accuracy, especially in receive mode. One possible source of error in the predicted far-fields is the NF/FF transformation. However, it will affect

both, model predictions and measurements in the same proportion, which is clearly not the case. Therefore, the near-field to far-field transformation is discarded as main source of error. Consequently, it is considered that most of the observed error is caused by the calibration (near-field radiation model). The discussion can be conducted separately for every antenna mode.

Transmit mode. Firstly, the required level of accuracy of the model and the measurement set-up is not necessarily high, since the -13 dB of SLL only represent about one order of magnitude. This means that the dynamic range of the field is relatively small, consequently, the model that represents the radiation does not need to feature a high resolution/accuracy/precision. Secondly, the antenna ports of the feeding network are highly isolated (the T/R-modules offer a very low transmission from the aperture to the feeding). Thirdly, the modules offer a good matching condition, and almost all the energy fed at every port is amplified by the module, and, consequently, radiated by the monopoles. These facts explain the observed accuracy on the predicted far-fields, as shown by the experimental results: HPBW, overall SLL and main-beam pointing direction are reproduced correctly.

Receive mode. This mode represents a more critical situation. Firstly, the -30 dB of SLL require a high precision of the model and of the measurement set-up (three orders of magnitude). Secondly, the feeding's network ports are highly coupled, independently of the matching offered by every module to its respective antenna port. It can be expected that this high coupling, in combination with the method followed to obtain the radiation model, can lead to measurement inaccuracies, which translate into an incorrect prediction of the radiation. The calibration process, and its possible sources of error, are analysed and explained with detail in the section 4.5.3.

Conclusions. The presented antenna radiation model is not predicting with sufficient accuracy the near-field distributions: both antenna modes show a higher SLL, as well as a certain pointing error, none of them accurately predicted by the model. This triggered the development of optimization routines, explained in Chapter 5, which successfully counteract the not sufficiently precise (*inaccurate*) calibration. Accuracy, or precision, has to be discussed at this point. It should be considered that -30 dB of SLL translate into a necessary accuracy of, at least, three orders of magnitude in the

beam-forming algorithm. Moreover, the erroneous prediction of results can have several causes, whose possible sources have been partially drawn within the previous paragraphs of the chapter. They are discussed in detail in the following and last section.

4.5 Model limitations

In this section the most sensitive aspects of the calibration and beam-forming process are described with detail. Firstly, the implementation of the near-field to far-field transformation is analyzed for this particular application, showing an strategy to reduced the amount of samples, as well as minimize the impact of the discrete sampling line in the predicted far-field. Secondly, an interpolation algorithm to obtain the beam-forming weights for any main-beam direction, without its corresponding near-field distribution, is shown. This way, the necessary full-wave simulations to accomplish the beam-forming can be very reduced. Finally, the role of the feeding network in the calibration process is explained and discussed. It is analytically demonstrated how the feeding network and the reflection coefficient of the T/R-modules can reduce the calibration's accuracy.

4.5.1 Near-field sampling effects

The deviations observed in the far-field radiation patterns motivate a study of the sampling line in front of the antenna, which in the NF/FF transformation is the integration line. A sketch of the set-up is depicted in Fig. 4.6.

The extension of the sampling line, as well as the number of samples are important parameters. On the one hand, the number of samples should be kept as low as possible to reduce the measurement time. On the other hand, the total length of the sampling line has to be enough to contain the most relevant aperture field contributions [87]. Furthermore, the distance between samples is previously fixed to the half of the distance between elements. This distance is accomplishing the Nyquist sampling theorem, applied in the k-space [87], and facilitates the calibration process implementation.

Besides, in this particular application, it has been observed a dependency between the main-beam angle and the position of the strongest field contributions along the aperture, as depicted in Fig. 4.7. This is due to the large electrical distance between the radiation sources and the measurement plane,

since there is enough distance to start observing the combination of the fields radiated by every antenna element.

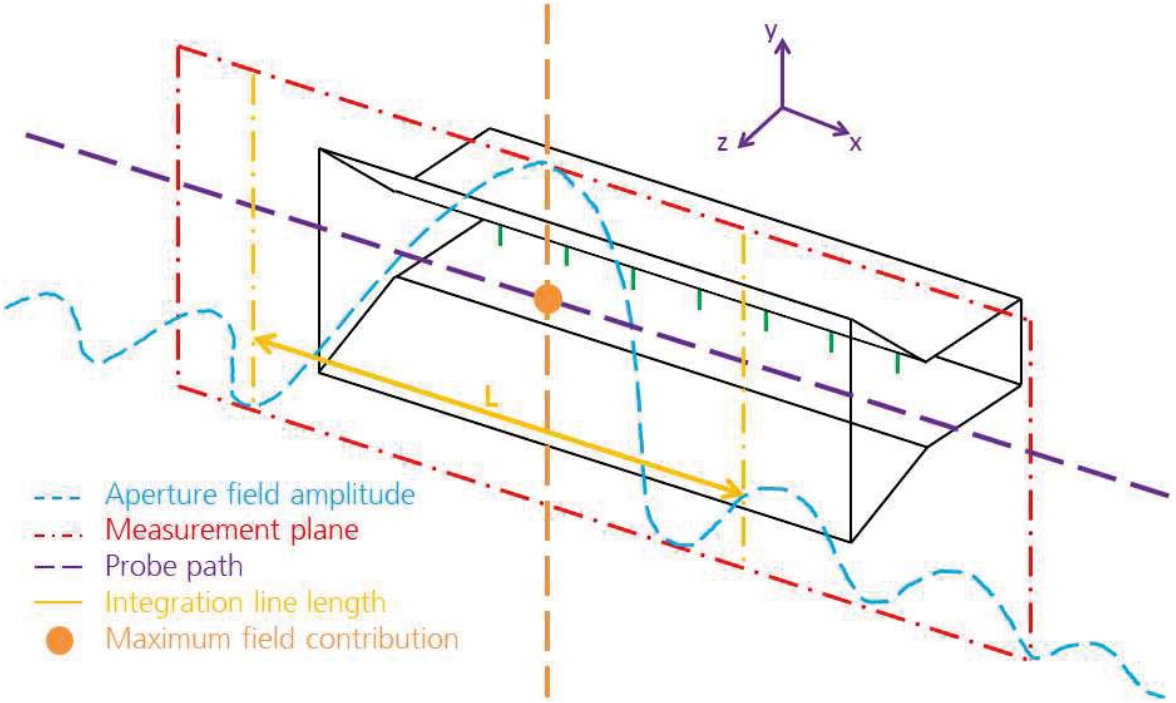


Figure 4.6: Sketch of the near-field measurement. The probe moves along the horizontal axis (x), measuring the vertical E-field contribution at each position.

This effect triggered the development of an iterative routine based on simulated near-fields, which increases progressively the length of the NF/FF integration line, which is centred at *the most significant field contribution* (see Fig. 4.6 or Fig. 4.7). The amount of samples is increased at each side until a certain far-field SLL error is achieved. An example of the calculated integration-line length for a SLL error below 1.5 dB (in transmit mode) can be observed in Fig. 4.8. Further near-field measurements are scheduled in order to validate experimentally this investigation. In any case, the introduction of large errors can be discarded.

As mentioned above, this is intended to minimize the amount of required near-field samples with two purposes: maintain the accuracy of the predicted far-field, and predict possible errors. This represents a general advantage in the calibration of an AESA antenna formed by several dozens of elements, since the measurement time is minimized.

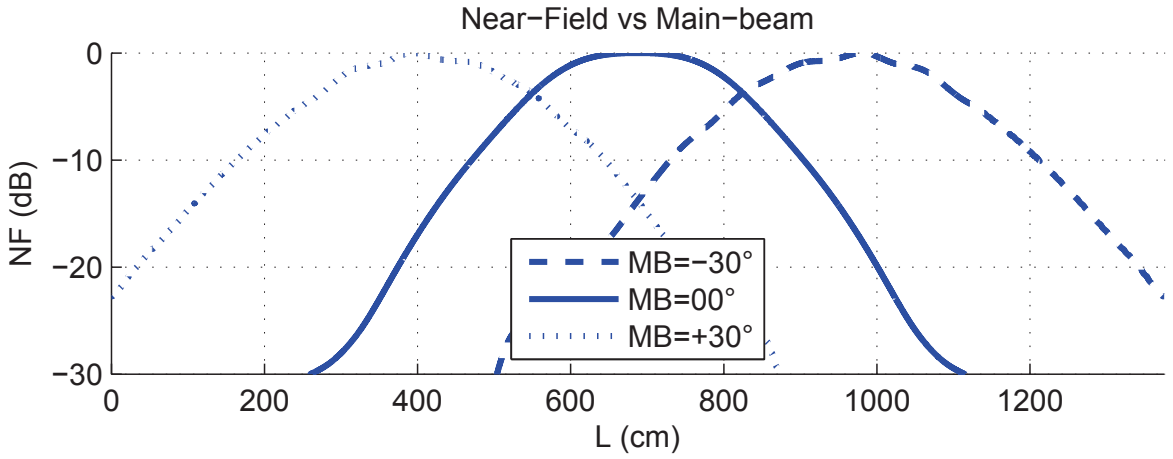


Figure 4.7: Measured near-field amplitude distributions for different main-beam angles.

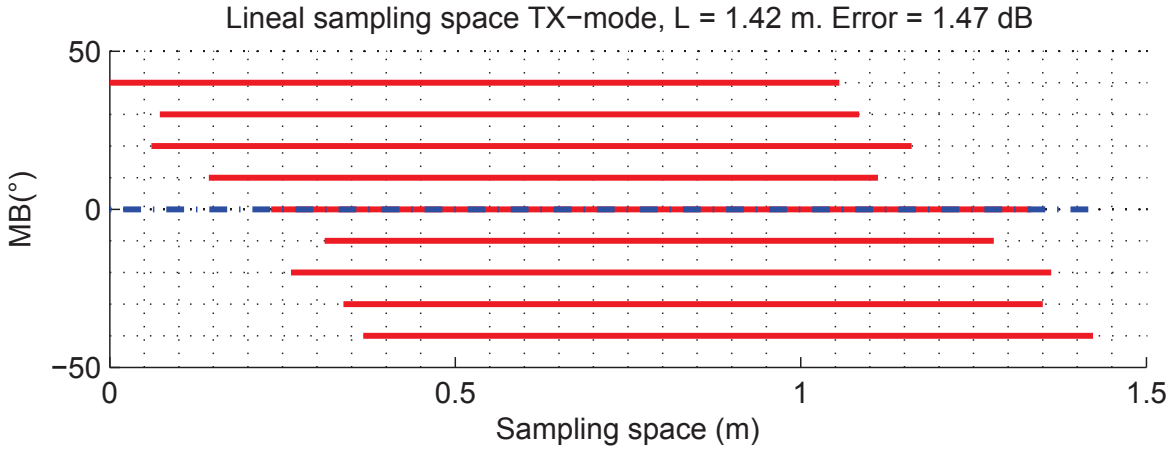


Figure 4.8: Required sampling line length depending on the main-beam angle and the maximum SLL error, transmit mode.

4.5.2 Predicted far-fields from extrapolated near-fields

One disadvantage of the proposed beam-forming technique is the need of full-wave simulations, since the near-field distribution along the aperture has to be obtained from simulations of every desired main-beam angle (θ_0).

In the case of a phased-array formed by a few elements, the full-wave simulation time is considerably long but manageable up to a certain extend. In the case of an AESA antenna made-up of about one hundred elements, the structure covers several dozens of wave-lengths (λ), and will require a high accuracy with respect to the electrical size of the problem. This typically translates into long simulation times.

For the reasons given above, it is decided to implement a method that can retrieve the needed near-field distributions with the minimum full-wave simulations possible. Here, an algorithm which obtains the aperture's near-field, for any main-beam angle, based on a reduced set of pre-computed distributions, is proposed.

The near-field to far-field transformation is similar to a Fourier-transform. Actually, it can be solved with the same computation scheme. Instead of time to frequency domain, $t \rightarrow \omega$, the transformation is from space to spectral domain, $x \rightarrow K_x$. Well-known transform properties can be used to address the extrapolation. First, we can apply the property of translation to model the change in the main-beam angle:

$$T_0(K_x - K'_x) \propto \int_{-\infty}^{\infty} s_p(x) e^{jK'_x t} e^{-jkt} dx. \tag{4.24}$$

By changing K'_x, a phase-shift of the near-field function, $s_p(x)$, produces a shift in the spectrum, $T_0(K_x - K'_x)$, where the spectrum shift is defined as $K'_x = k_0 sin(\theta_0)$, and $K_x = k_0 sin(\theta)$.

Besides, the near-field distributions exhibit not only a change in the phase proportional to θ_0, but also a shift in space, which can be defined as x_0 (see Fig. 4.7). Hence, the space-shift of the near-field is included in the model, recalling the property of translation in the space domain:

$$\begin{aligned} T(K_x - K'_x) \propto \int_{-\infty}^{\infty} s_p(x - x_0) e^{jK'_x(x-x_0)} e^{-jk_x x} dx = \\ e^{-jK'_x x_0} \int_{-\infty}^{\infty} s_p(x - x_0) e^{jK'_x x} e^{-jk_x x} dx. \end{aligned} \tag{4.25}$$

In addition, the integral terms in eq. (4.25) and eq. (4.24) are very similar, since the Fourier transform of $s_p(x)$ is a *sinc*-like distribution. Thus, it can be assumed that the transformation of its space-shifted version produces a very similar result. Hence, the following approximation is proposed:

$$T(K_x - K'_x) \approx e^{-jK'_x x_0} T_0(K_x - K'_x). \tag{4.26}$$

Besides, the near-field distributions of the aperture are very similar for far-fields with closely scanned main-beams. Therefore, it is proposed to obtain the desired main-beam angle by applying the appropriate phase-shift and space-shift to a given near-field distribution (reference), which corresponds to a different but closely scanned far-field.

Consequently, it is assumed that it can be obtained the spectrum of the desired far-field pattern, $T(K_x - K'_x)$, as a function of a given reference distribution, $s_{p,ref}(x)$. Then, the target of the extrapolation is to obtain an spectrum, $T'(K_x - K'_x)$, which is equivalent to the desired one.

With this purpose, it is assumed that the desired (extrapolated) function can be obtained applying a different spectrum shift and space shift terms, K''_x and x'_0 respectively, to the given reference near-field. These assumptions resort to the following formulation of the extrapolated spectrum:

$$\begin{aligned} T'(K_x - K'_x) \propto \int_{-\infty}^{\infty} s_{p,ref}(x - x'_0) e^{jK''_x(x-x'_0)} e^{-jk_x x} dx = \\ e^{-jK''_x x'_0} \int_{-\infty}^{\infty} s_{p,ref}(x - x'_0) e^{jK''_x x} e^{-jk_x x} dx. \end{aligned} \tag{4.27}$$

The shifting terms, K''_x and x'_0, can be expressed as a function of the desired main-beam direction and the given one, θ_0 and θ_{ref} respectively.

Firstly, the analytical solution of the K''_x term is given. As previously mentioned, it is assumed that eq. (4.26) is equivalent to eq. (4.27):

$$\begin{aligned} T(K_x - K'_x) \propto e^{-jK'_x x_0} \int_{-\infty}^{\infty} s_p(x - x_0) e^{jK'_x x} e^{-jk_x x} dx \equiv \\ T'(K_x - K'_x) \propto e^{-jK''_x x'_0} \int_{-\infty}^{\infty} s_{p,ref}(x - x'_0) e^{jK''_x x} e^{-jk_x x} dx. \end{aligned} \tag{4.28}$$

In addition, it is considered that the reference function of the near-field has the same behaviour as the targeted near-field. Besides, the corresponding phase-shifting, according to the angular shift, has to be included. Hence:

$$s_{p,ref}(x) \approx s_p(x) e^{jK'_{x,ref}x}. \tag{4.29}$$

Then, we can rewrite the equivalence in eq. (4.28) as follows:

$$\begin{aligned} T(K_x - K'_x) &\propto e^{-jK'_x x_0} \int_{-\infty}^{\infty} s_p(x - x_0) e^{jK'_x x} e^{-jk_x x} dx \equiv \\ T'(K_x - K'_x) &\propto e^{-jK''_x x'_0} \int_{-\infty}^{\infty} s_p(x - x'_0) e^{jK'_{x,ref} x} e^{jK''_x x} e^{-jk_x x} dx. \end{aligned} \tag{4.30}$$

The equivalence in eq. (4.30) can be considered valid when the phase terms of both integrals satisfy the expression $K'_x = K''_x + K'_{x,ref}$, which can be developed to obtain:

$$\begin{aligned} &K''_x = K'_x - K'_{x,ref} = k_0 \; sin\theta_0 - k_0 \; sin\theta_{ref} \Longrightarrow \\ &K''_x = k_0(sin\theta_0 - sin\theta_{ref}) \approx k_0(\theta_0 - \theta_{ref}), \ll (\theta_0 - \theta_{ref}). \end{aligned} \tag{4.31}$$

The analytical solution of the term x'_0 has not being determined. On the one hand, this term has no influence in the pointing direction, accordingly to the presented model. On the other hand, it has to be ensured that the interpolated near-field distribution can be physically generated by the phased-array. For this reason, the space-shift has been determined by means of inspection from simulated, near-field distributions, as $x'_0 = (\theta_0 - \theta_{0,ref})/2$.

In this case, any angle within the full scanning range, $[-46°, +46°]$, can be obtained with only nine reference near-fields, starting from $-40°$ to $+40°$, with $10°$ spacing. For demonstrating purposes, in the receive-mode, several scanned near-fields with $3°$ spacing are compared for both, near-field model predictions and directly measured near-fields in Fig. 4.9. A good agreement between simulations and measurements is observed.

This extrapolation allows to obtain antenna weights for any θ_0, as far as the real (non-interpolated) near-field distribution similarity to the reference distribution is sufficient, and the difference between the targeted and the reference beam direction is small.

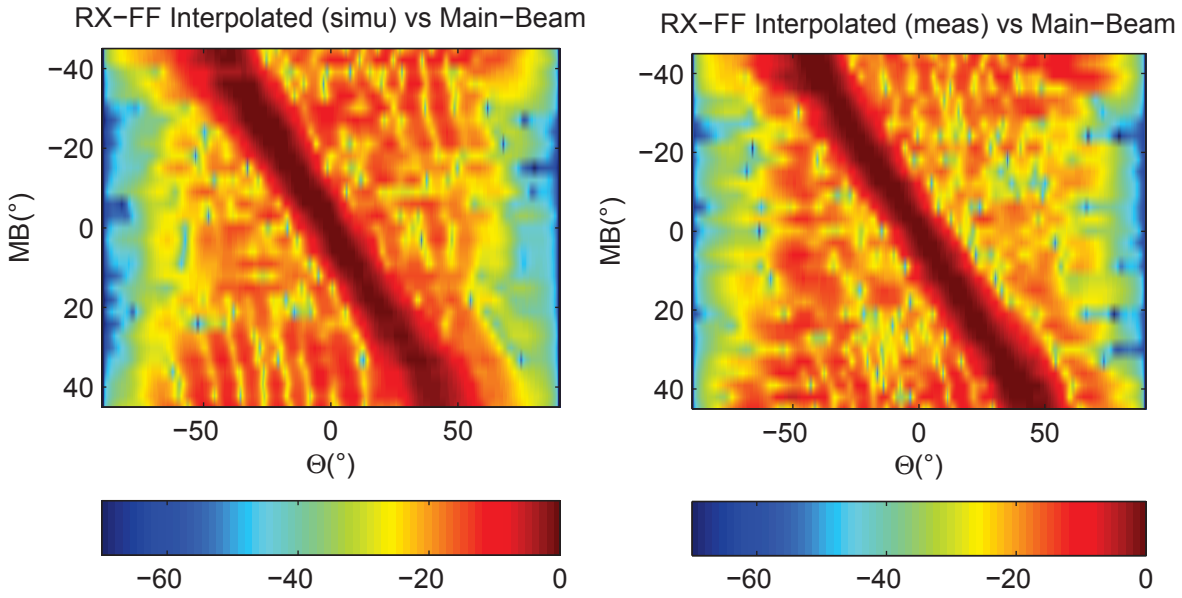


Figure 4.9: Prediction of far-field radiation based on extrapolated near-fields, receive-mode. On the left, the extrapolated near-fields are simulated. On the right, the near-field distributions are directly measured. In both cases, the far-fields are obtained by the shown NF/FF transformation.

4.5.3 Near-field radiation model limits

The calibration assumes that the factors $\beta_{n,m}$, eq. (4.1), are independent of the states of the T/R-modules, which might not be the case since active elements may behave slightly different depending on the state that they, and their neighbouring modules, are operated in.

The relation between the weights and the field in the aperture is not necessarily linear, despite of the linear/passive feeding network, which can translate into an inaccurate antenna calibration. This can be the consequence of the non-linear devices present in the front-end, as well as the strongly coupled antenna ports. Furthermore, the solutions obtained from the pseudo-inverse are approximated by discrete values of the PGMs. However, it is considered that the influence of these effects cannot represent an error of 10 dB in the SLL, as observed for the receive-mode.

In addition, there are undesired effects consequence of the particular feeding network employed, which are not included in the numerical antenna radiation model. The measurement process to obtain the antenna calibration is explained in first place, in order to illustrate these negative effects. The calibration process concept is depicted in Fig. 4.10.

The routine's milestones can be explained as follows:

1. All modules are set to the lowest gain state (*passivated*)
2. The probe is moved one step along the horizontal axis (x-direction)
3. The modules are set to the reference state one by one, while the remaining elements are *passivated*
4. The modules' transmissions/receptions are measured one-by-one with all the other elements *passivated*. If the probe is directly in front of one T/R-module, its corresponding PGM is measured
5. The process is repeated until the last sampling point is reached

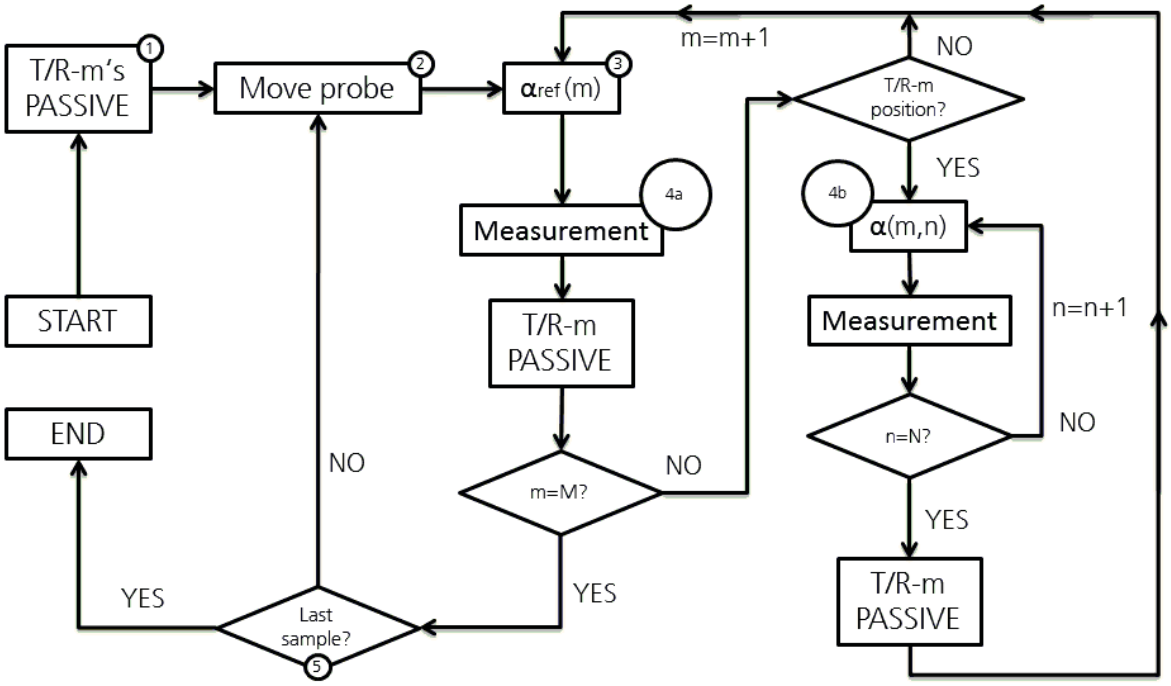


Figure 4.10: Near-field calibration process concept. This measurement routine allows to obtain the relation of the near-field produced at the aperture and any arbitrary antenna excitation.

In the transmit mode, the transmission from the common port of the feeding to every antenna element depends nearly on the element itself: the modules are highly isolated from each other and they offer a good matching condition to their corresponding RF port. On the contrary, in the receive

case, there is no isolation between antenna ports: the RF ports of the feeding network are strongly coupled. This high-coupling can be affecting the calibration more than expected.

The behaviour of the calibration in receive mode can be explained with numerical models based on the scattering parameters of the feeding network demonstrator. The modelling concept used to observe this situation is represented in Fig. 4.11. It can be shown that multiple interactions are not considered, although, it is an acceptable approach to show and understand the possible effects. Following, the model is analytically described.

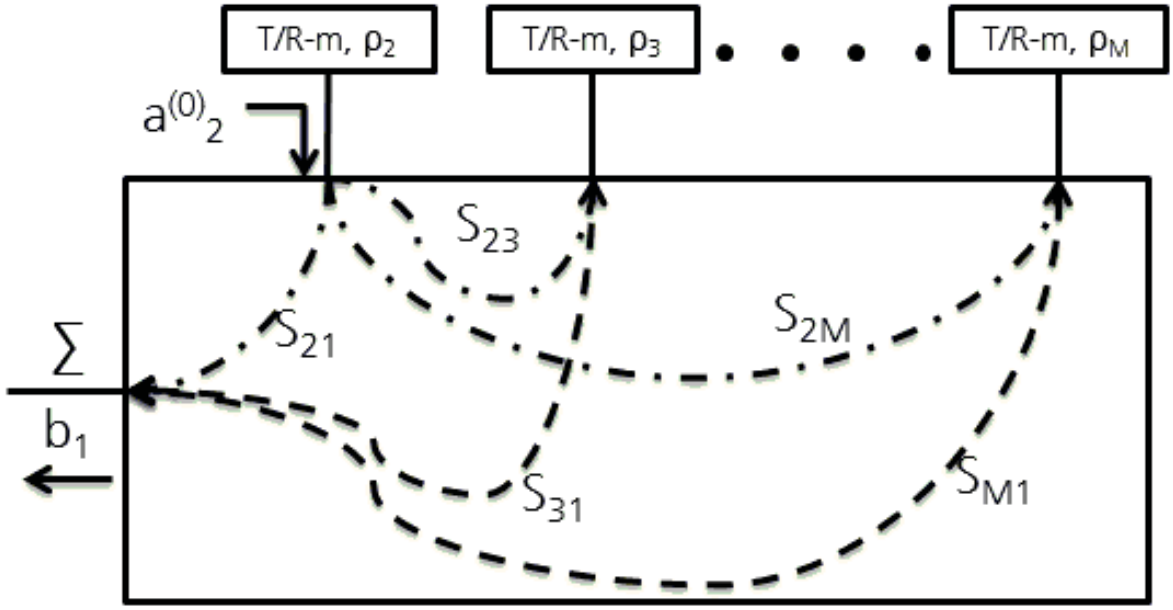


Figure 4.11: Representation of undesired effects on the calibration, due to the highly coupled RF ports of the feeding network, in receive mode. In this case, the input signal is at port number 2. Multiple interactions are not considered.

Firstly, the output signal at the summation port (nr. 1) is defined as function of the incoming waves on every port, a_m, and the transmission parameters from every port to the feeding's common-port, S_{m1}:

$$b_1 = \sum_{m=2}^{M} a_m S_{m1}, \tag{4.32}$$

for $a_1 = 0$. Furthermore, in the particular case of excitation present only at port nr. 2, the term a_m in eq. (4.32) can be expressed as a function of the

scattering parameters and the reflection coefficients, S_{m2} and ρ_m respectively, in the following manner:

$$\begin{aligned} a_m &\approx a_2^{(0)},\ m = 2 \\ a_m &\approx a_2^{(0)} S_{m2} \rho_m S_{1m},\ m \neq 2, \end{aligned} \tag{4.33}$$

where:

- $a_2^{(0)}$: incoming wave at port nr. 2
- S_{m2}: transmission parameter from port nr. 2 to the m-th port
- S_{1m}: transmission parameter from the m-th port to port nr. 1
- ρ_m: reflection coefficient at the m-th port

Then, the output signal at the common port can be expressed as:

$$b_1 \approx a_2^{(0)} S_{21} + \sum_{m=3}^{M} a_2^{(0)} S_{2m} \rho_m S_{1m} = a_2^{(0)} \left(S_{21} + \sum_{m=3}^{M} a_2^{(0)} S_{m2} \rho_m S_{1m} \right). \tag{4.34}$$

Finally, we can generalize eq. (4.34) to an arbitrarily excited k-th port:

$$b_{1,k} \approx a_k^{(0)} \left(S_{k1} + \sum_{m=2, m\neq k}^{M} a_k^{(0)} S_{mk} \rho_m S_{1m} \right). \tag{4.35}$$

This simplified model allows to simulate the measured transmission parameters from every T/R-module to the summation port of the feeding, in the case of different reflection coefficients on the non-active ports. Simulation results are shown in Fig. 4.12. It can be observed that the transmissions to the summation port are not acquired properly, even for significantly low reflection coefficients. Therefore, a low reflection coefficient at the RF ports, ρ_m, is necessary. Consequently, this is a fundamental condition to be full-filled by the T/R-modules while they are *passivated*.

Feeding networks are typically designed to be inherently matched, i.e. the reflection coefficient, ρ_m, of all ports is always very low, and with a high isolation between antenna ports [10, 28, 50, 51]. Therefore, any effects due to the reflection coefficient at the antenna ports will be present within

the calibration process of any *conventional* phased-array antenna. However, any undesired influence would be mitigated by the *resistors* in the feeding network.

Because of this, the influence of the feeding network is usually negligible and similar for all antenna elements. On the contrary, it has been shown that, for the proposed system's architecture, the feeding network has an important influence during the calibration process, especially in receive mode. However, this effect can be mitigated if the T/R-modules offer a sufficiently low reflection coefficient to the RF network ports.

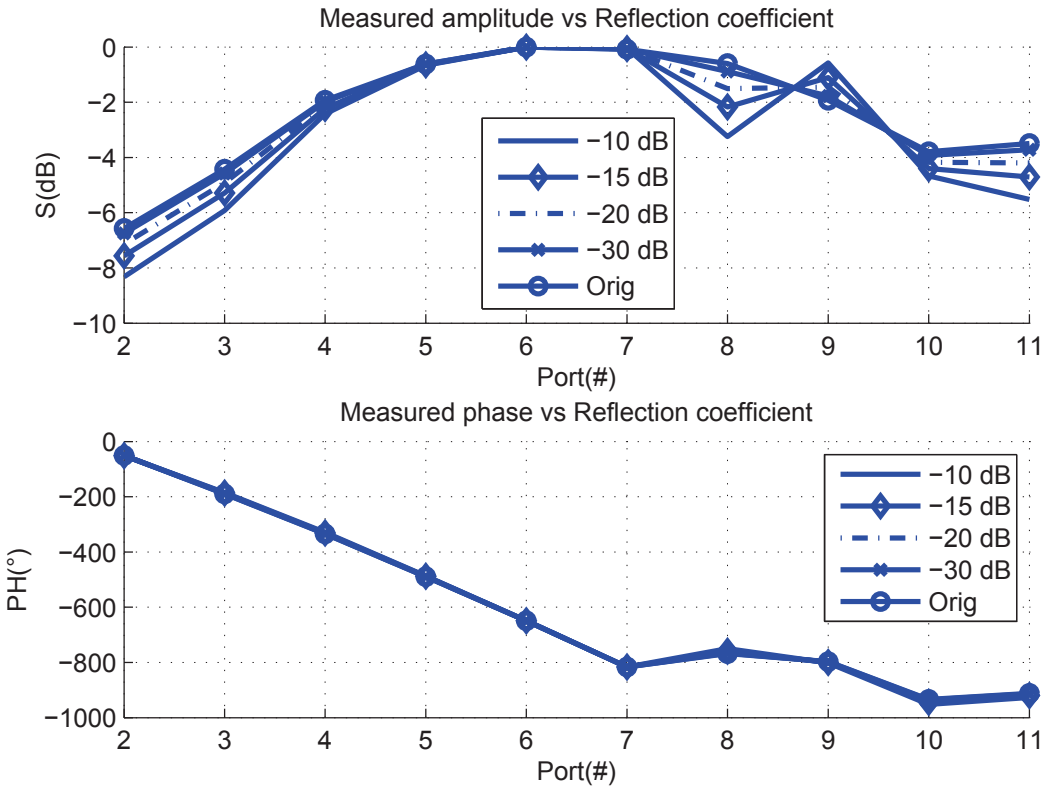


Figure 4.12: Simulated transmissions to the common port for several different *passivated* T/R-modules' reflection coefficients. The ideal values are shown for a better comparison (*Orig*).

Other drawback of the technique to obtain the radiation model of the antenna is due to the lowest gain (residual gain) achievable by every T/R-module. The receive mode calibration can be taken as an example to describe this situation. It can be assumed that every T/R-module is contributing with its own gain to the signal at the summation port, even when one module is

being measured alone. Therefore, an undesired transmission is produced and added to the *activated* element transmission.

The model presented above can be modified to represent the effects of any residual gain. The simulation results on Fig. 4.13 are an example, where the same amplitude is fed into every module, and assumes that the signal is amplified with a lower gain by the *passivated* modules. It can be observed that even for amplifications 20 dB lower than for the *active* element, the transmission is not acquired properly. A similar effect can be expected in transmit mode.

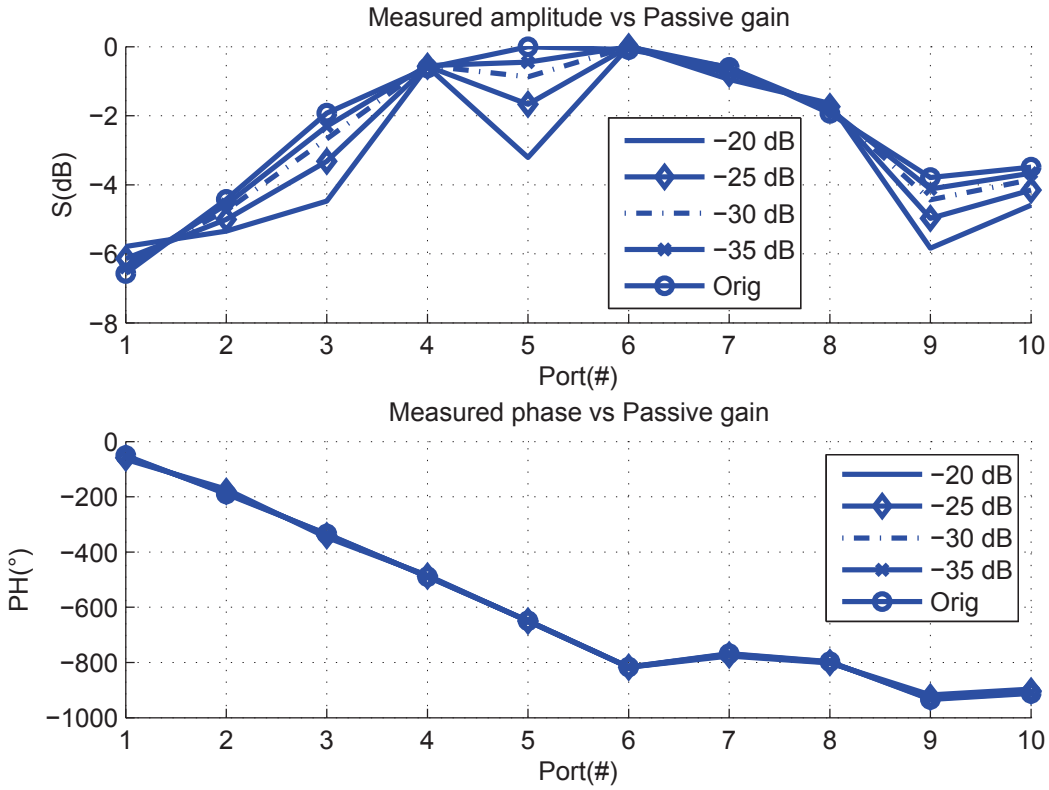


Figure 4.13: Simulated transmissions to the common port for several different *passivated* T/R-modules' residual gains. The ideal values are shown for a better comparison (*Orig*).

On the one hand, the shown issues are assumed as the principle causes of the inaccuracies of the calibration. On the other hand, the process is not clearly showing any of the listed effects, but a small combination of them can produce a strong effect, since the order of magnitude necessary is very large (at least three orders of magnitude for the receive case).

Additionally, as mentioned before, this model is an approximation that allows to illustrate in a simplified manner the behaviour and influence of the feeding network within the calibration process. However, in Chapter 5 (section. 5.5) a more complete approach is shown. In addition, the role of the special feeding network operation is discussed, focusing the analysis in the results to be expected when the AESA antenna receives plane waves from several angles, different from the main-beam direction.

Chapter 5

Far-field optimization and analysis

The results of the beam-forming presented in the previous chapter can be improved by means of optimization routines [80], [81]. Therefore, a post-optimization algorithm is developed with this purpose. In addition, as validation method, the far-fields of the AESA antenna are measured in an anechoic chamber, after and before the optimization. Moreover, the experience acquired with the near-field based calibration approach is used to develop an improved calibration method, following similar principles but based on far-field measurements.

Firstly, this chapter presents a post-optimization algorithm, which actively enhances the far-field radiation patterns obtained by the near-field based synthesis presented in Chapter 4. This optimization is necessary due to the previously mentioned limitations of the near-field antenna calibration. In addition, as experimental validation for the NF/FF transformation, the predicted radiation patterns (optimized and non-optimized) are compared against directly measured far-fields.

Secondly, a far-field based antenna calibration is presented. In Chapter 4 it is shown that the near-field calibration approach is not sufficiently accurate. For this reason, it is developed a far-field based calibration, in order to research for possible causes of inaccuracy directly in the far-field radiation. In fact, due to the far-field approach, it is possible to identify and counteract the source of the erroneous prediction of patterns.

Thirdly, since the required radiation pattern performance is not achieved, it is shown that there is room for improvement by means of an optimization

routine. The main advantage of the presented method is that the far-field patterns are enhanced without further antenna measurements, thanks to the improved calibration approach. Consequently, the overall beam-forming time is highly reduced, which enables the method for medium-size phased-arrays.

Finally, the behaviour of the feeding network is further analysed, but from a far-field point of view, completing the discussion introduced in Chapter 4. In addition, this allows to explore the limits of the beam-forming by means of numerical models.

5.1 Near-Field based optimization

After calibration, the near-field based beam-forming is producing satisfying electronically scanned radiation patterns in both antenna modes, as shown by the measurement results in Chapter 4. Nevertheless, increased SLLs and slight main-beam pointing errors can be observed, specially in the receive mode. In addition, those deviations are not completely predicted by the antenna radiation model previously presented. However, it can be proposed to optimize the initial beam-forming weights (pseudo-inverse/LMS-based) by means of an iterative post-optimization process.

The pattern synthesis method in [91] shows that the beam-forming does not necessarily need to be an optimum excitation, but a sub-optimum. The approach proposed here makes use of this synthesis concept, in combination with small variations of the initially calculated antenna excitation. The optimization routine varies the initial (original) beam-forming weights, towards a configuration that accomplishes the given radiation pattern constraints.

The main disadvantage is the near-field radiation model accuracy, which is not sufficiently precise to properly predict the antenna's radiation, specially in receive mode. However, this can be counteracted by systematic modification of the beam-forming weights (T/R-module states). A set of locally small phase and amplitude changes on every T/R-module can be defined. Every set of changes produces its corresponding slight variations on the aperture's near-field, which can be directly measured.

The changes applied to the beam-forming produce small, but measurable, effects on the far-field. Therefore, an interpolation can be used to obtain patterns produced by both, local and global (and full or partial) combinations of T/R-module state variations. Hence, the dependence on the initial *not sufficiently accurate* calibration is eliminated.

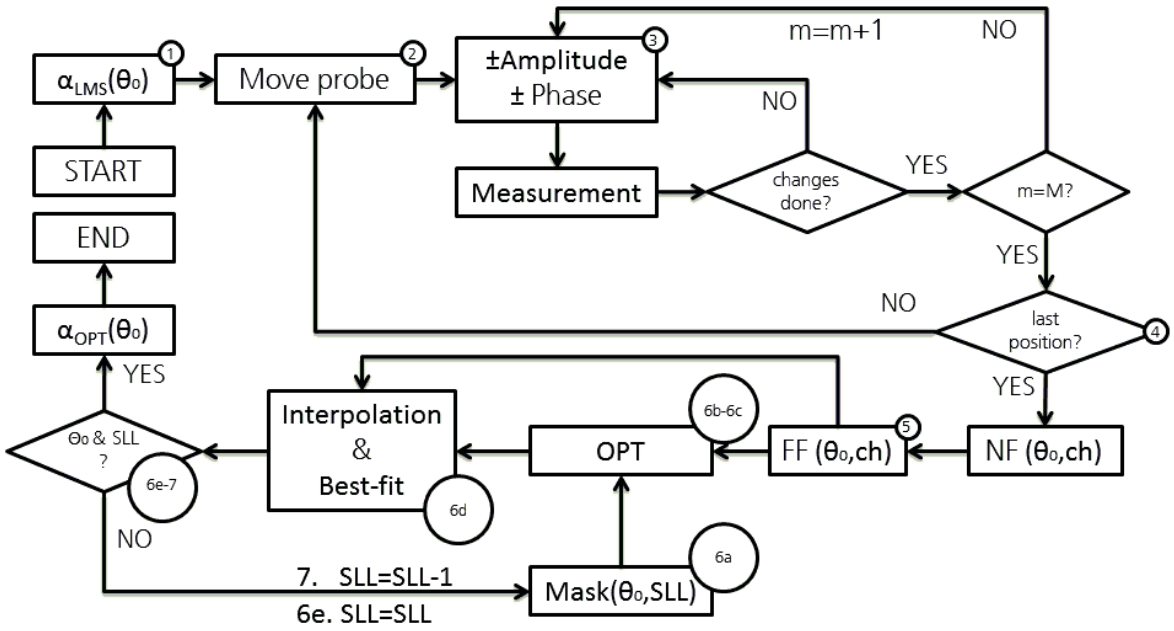


Figure 5.1: Optimization routine to enhance the LMS antenna weights obtained by the near-field antenna model. Some steps are omitted for the sake of simplicity.

The post-optimization algorithm is shown in Fig. 5.1, and it can be explained as follows:

1. The T/R-modules are set to the LMS weights
2. The probe is moved one step trough the horizontal axis (x)
3. Phase & amplitude of every module are slightly changed, while the remaining elements are *static*. The field is sampled after every change
4. Steps 2 and 3 are repeated until the last scanning position is reached
5. Far-fields of the locally changed near-fields are calculated
6. A gradient-based optimization routine determines the amount of phase and amplitude to be changed in every element, by interpolation of the far-fields, obtained from the previously recorded near-field *changes*:
   (a) The pattern mask which sets the maximum levels of the pattern at every θ is defined. If there is a significant pointing error, a larger SLL than the one offered by the original pattern is used. On the opposite case, the SLL is set to a lower value

(b) The cost function of the algorithm depends on the pattern mask and the pointing direction

(c) The gradient-based algorithm varies the weights to minimize the cost function

(d) The new pattern is calculated (by interpolation)

(e) The process is repeated until the pattern accomplishes the mask

7. The previous step is repeated until the targeted SLL is reached

The double iteration in step 6.*e* and step 7 can be necessary, since the distance between the initial patterns an the targeted result can be large.

In addition, the SLL of the pattern mask is decreased slowly, in order to avoid conflicts between the main-beam angle and local *minima* of the cost function. In case that the algorithm converges to an unsatisfactory result, the process can be repeated. In the transmit case, only changes in phase are necessary (steps 3 & 6), since uniform illumination is desired.

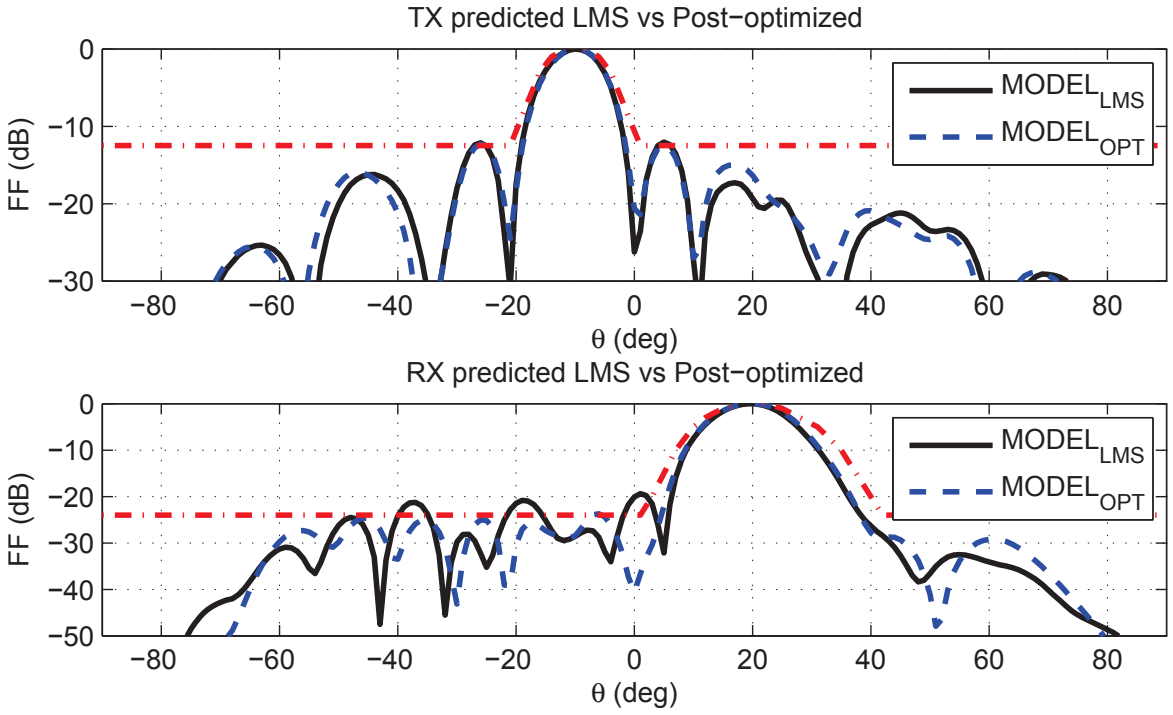


Figure 5.2: Predicted transmit (top) and receive (bottom) far-field radiation patterns, for main-beam directions of $-10°$ and $+20°$ with respect to broad side, respectively. Antenna weights obtained by LMS and after post-optimization.

The far-fields shown in Fig. 5.2 are calculated from measured near-fields, using the NF/FF transformation previously presented (Chapter 4). The pointing error predicted is negligible, and the desired SLLs are almost reached (see Fig. 5.2, red dashed line). A single iteration of the algorithm has been performed. The duration of the post-optimization is dominated by the measurement time of the several state changes on every T/R-module, for every probe position in front of the antenna aperture. The overall time makes the approach un-practical for a medium-sized phased-array.

As experimental validation, the far-field patterns are measured in an anechoic chamber, installing the demonstrator on a turning table (shown in Fig. 5.3). Examples of measurements are depicted in Fig. 5.4. The main-beam angle, the HPBW and the SLL are predicted correctly.

In the transmit mode, the optimized beam-forming is successful: the pointing error is negligible and the targeted SLL (-13 dB) is accomplished.

In the receive mode, the main-beam direction error is always very low. Moreover, in the $[-15°, +15°]$ scanning range, the targeted -30 dB of SLL has almost been reached with only a single iteration of the post-optimization process. The beam-forming (and its optimization) becomes more difficult for the main-beam angles beyond $\pm 20°$. This issue is discussed with detail in the forthcoming sections.



Figure 5.3: Photograph of the AESA antenna mounted on the turning table. The reference antenna is static (not shown). The array of monopoles can be observed inside the aperture. Only three cables are necessary to interface the front-end: power supply, RS-232 and RF.

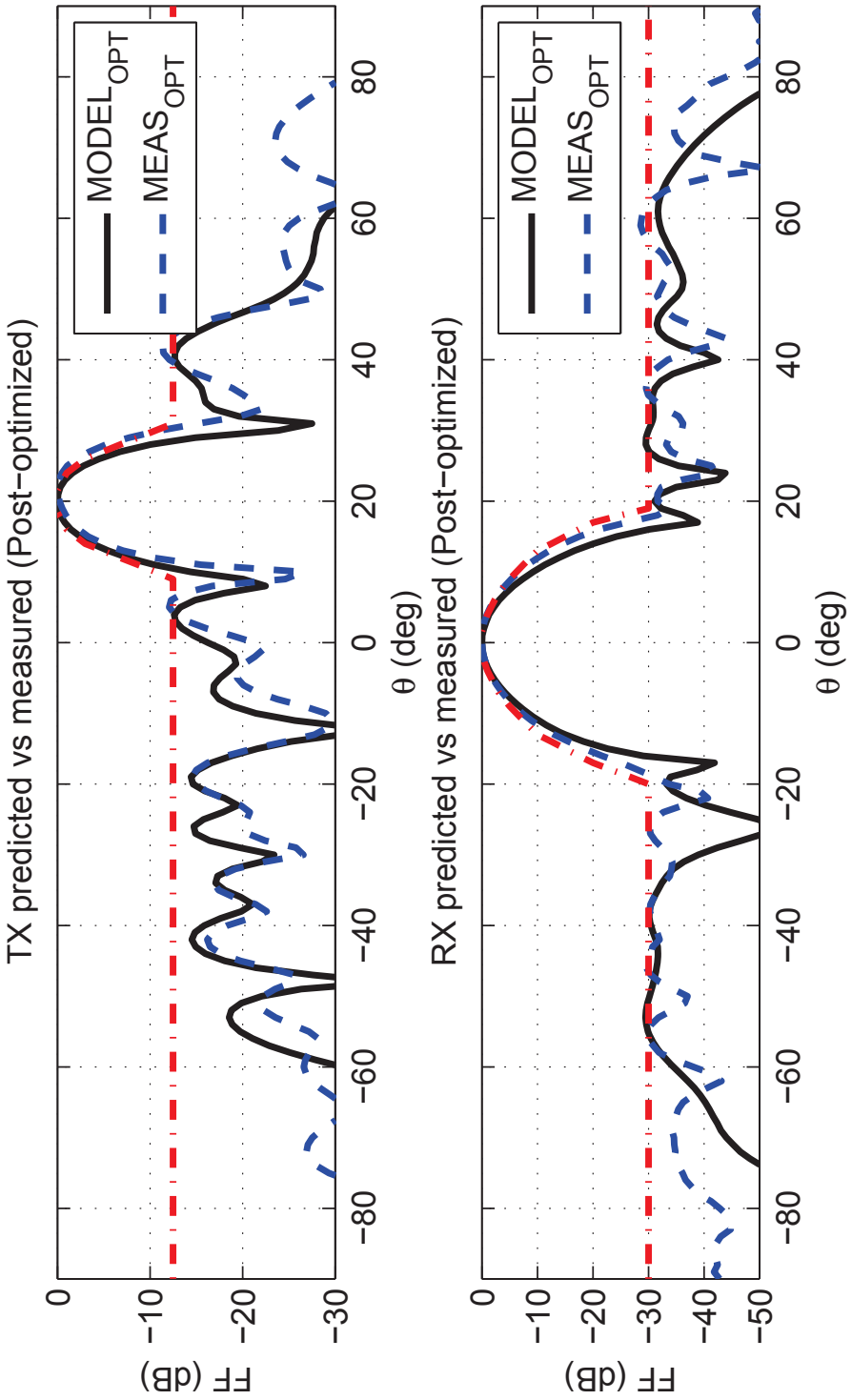


Figure 5.4: Measured transmit (top) and receive (bottom) far-field radiation patterns, for main-beam directions of $+20°$ and $0°$ with respect to broad side, respectively. The far-field predicted by the NF/FF transformation is included for better comparison. Post-optimized antenna weights.

5.2 Far-field beam-forming and calibration

In the previous section, it has been shown a successful optimization algorithm. This optimization requires a significantly large overall measurement time, which makes the approach non-practical either if several iterations are necessary, or for medium-sized phased-array antennas.

In order to increase the calibration accuracy, while reducing the necessary time, two algorithms based on far-field measurements are developed: an alternative calibration and an improved beam-forming strategy.

5.2.1 Far-field calibration

Prior to research for possible alternatives to improve the measured beam-forming results, it should be analyzed the difficulties encountered to obtain low SLL for high main-beam angles in the receive mode. It is proposed that inherent front-end physical limitations can be the cause, and an analysis directly in the radiating far-field of the aperture can facilitate the task.

At the sides of the aperture, lateral polyethylene walls are placed, in order to provide mechanical stability to the assembly (shown in Fig. 5.3). Furthermore, these walls are proposed as a smother transition from the antenna aperture sides to the free-space, in an attempt to reduce edged effects in such a small aperture. In addition, the electronic scanning of the antenna produces that the maximum of the near-field received/radiated by the aperture is moved towards the edges. Therefore, the possible disturbances of the lateral walls on the aperture's near-field are to be significant in the far-field.

It is proposed to replace those walls by polyethylene sticks on the edges of the horn structure (Chapter 3, Fig. 3.14). On the one hand, after the substitution of the polyethylene-walls, a much lower SLL (in receive mode) is measured with the previously calculated antenna weights, for the high main-beam angles. On the other hand, a pronounced error on the main-beam angle is measured. Despite of the promising results, since the electromagnetic environment of the whole aperture is different, it is necessary to calibrate the new AESA antenna configuration, either in the near-field or in the far-field.

Despite of the demonstrated robustness of the NF/FF transformation, it is decided to develop a far-field antenna calibration, as mentioned above. This way, it can be investigated directly in the far-field the sources of the unsatisfactory experimental results. An sketch of the calibration algorithm is shown in Fig. 5.5.

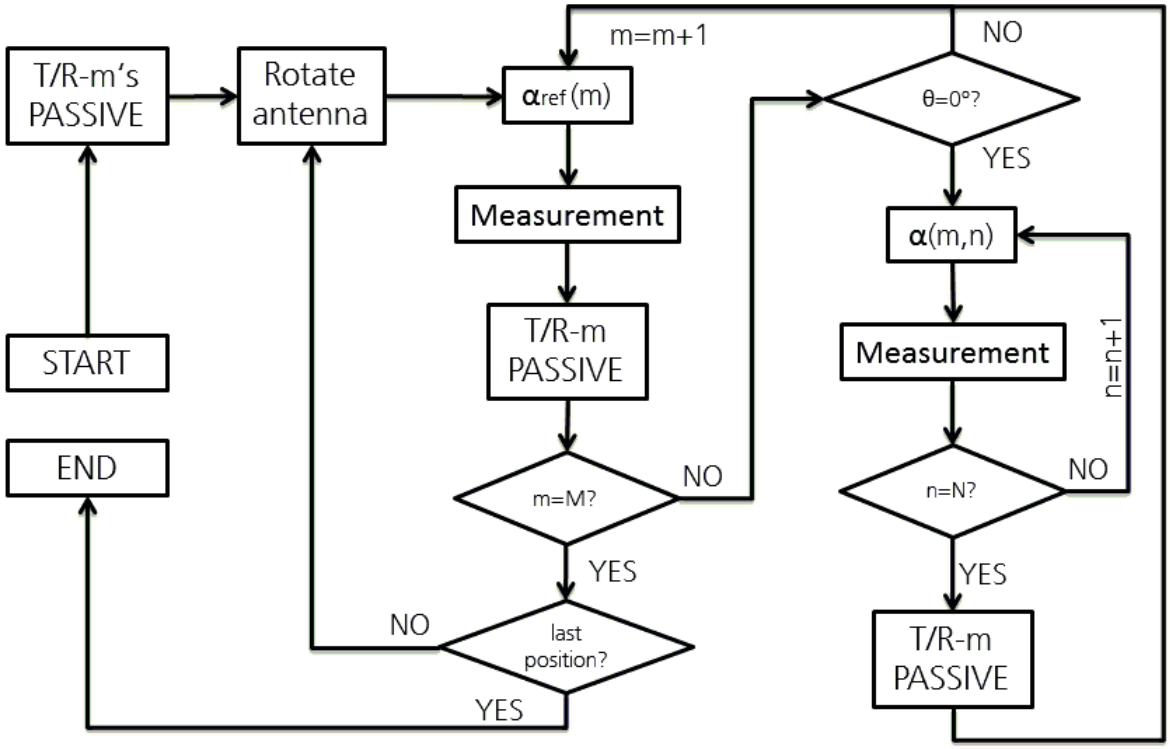


Figure 5.5: Far-field calibration process based on far-field measurements.

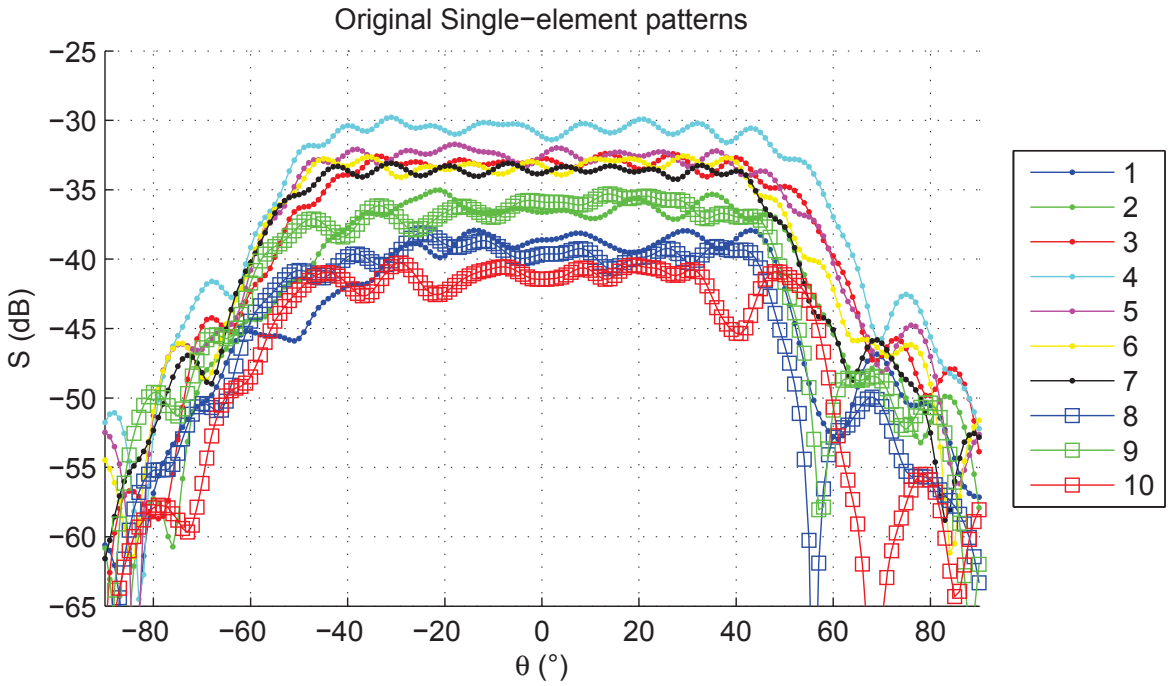


Figure 5.6: Directly measured embedded element patterns, receive mode. It is not expected such an asymmetric behaviour.

The main difference in the algorithm, with respect to the near-field case, is that this second calibration measures the far-field patterns of the elements and the embedded PGMs in the far-field; in the first case all the measurement where done in the radiating near-field of the aperture.

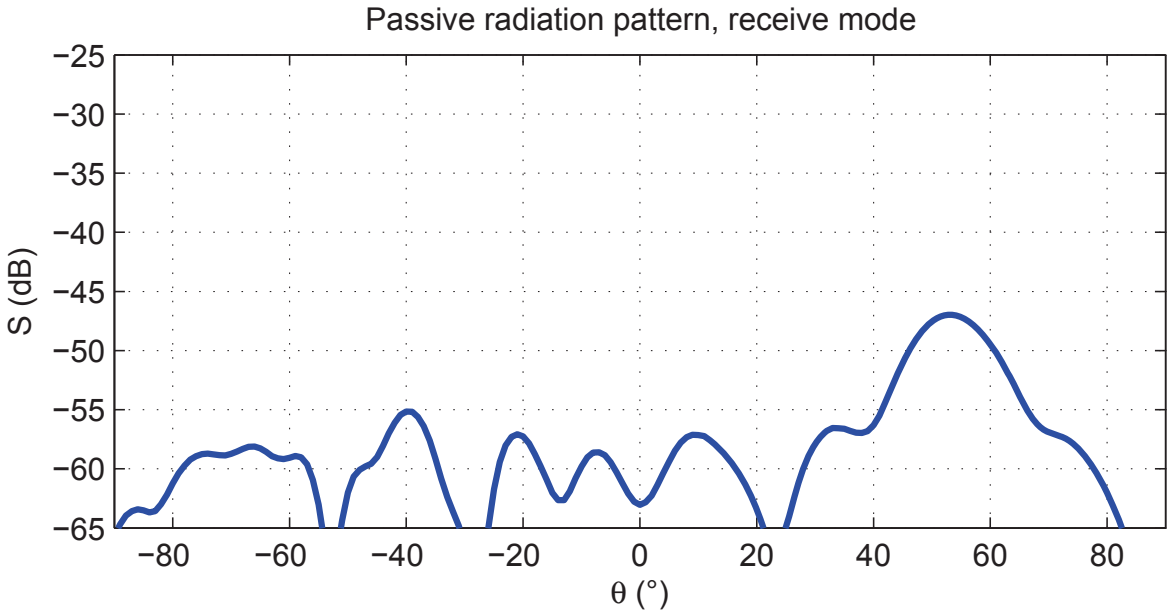


Figure 5.7: Measured passive pattern in receive mode while the active antenna is *passivated*. This is an expected result, but not the order of magnitude, which is comparable to the single element patterns.

The measured single-element patterns in receive mode are depicted in Fig. 5.6. The asymmetry observed in the patterns cannot be justified exclusively by the inherent mutual coupling or edge effects [32], [49]. In addition, with all the elements set to their minimum gain (*passivated*), the far-field shown in Fig. 5.7 is measured. This can be an expected result, since when the modules are *passivated* there is still a residual transmission from the aperture to the feeding network. However we can observe that the order of magnitude is comparable to the single element patterns. Hence, it is assumed that the passive pattern is shading off the actual embedded element radiation pattern.

A plain manner to remove the undesired effects from the measurements is proposed. The concept is based on the T/R-module's PGM. The T/R-module is designed in such a way that, the four lowest gain states define the corners of a square centred at *zero*-gain (Chapter 3, Fig. 3.9), whose average is ideally zero. The four passive states of the module of interest are measured,

and its average is subtracted from the single element pattern. This has to be done for all angular positions, since the phase of the wave fed by every element into the feeding network changes with the angle of incidence of the plane wave emitted by the reference antenna.

The corrected embedded-element radiation patterns show a smother and much more symmetric behaviour, as depicted by Fig. 5.8. Nevertheless, the reduced amount of radiating elements is still producing pronounced edged effects. In the following paragraph, the benefits of the improved calibration method are demonstrated for both antenna modes.

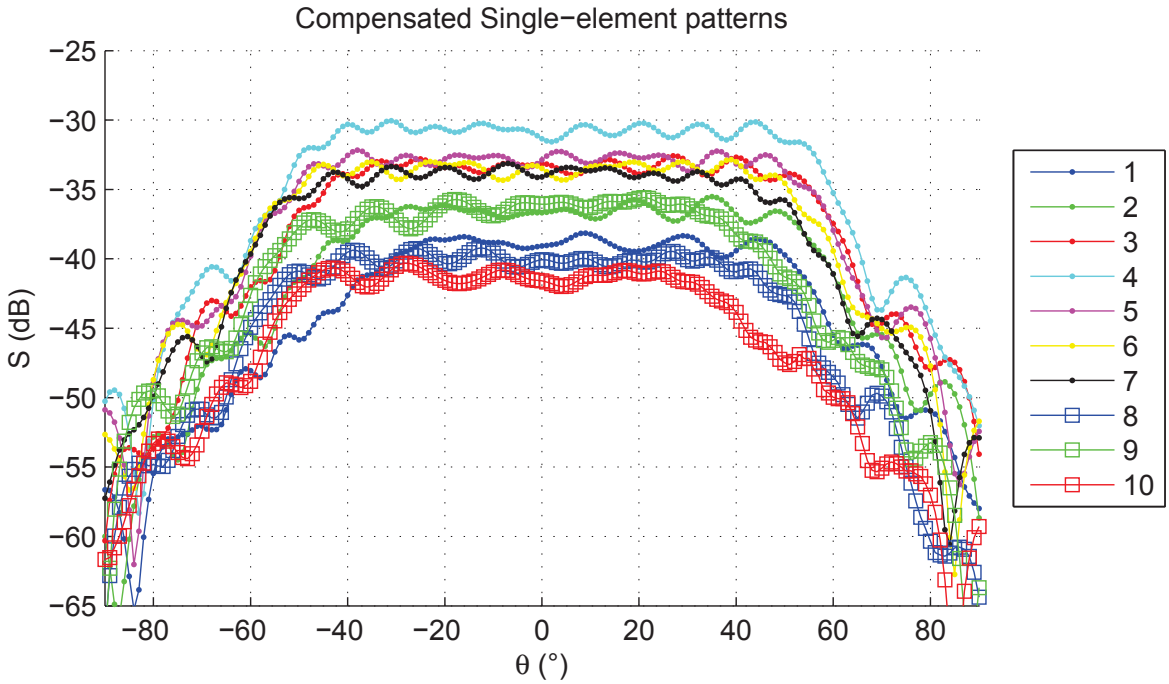


Figure 5.8: Compensated embedded element patterns, receive mode. The far-field of the element patterns are smother, and the behaviour is in general more symmetric. The edge effects of such an small array can justify the observed results.

5.2.2 Far-field based beam-forming

The far-field based calibration uses similar concepts as in the near-field case. The main modification is the compensation of the undesired effects measured on the single element patterns. The diagram synthesis principle proposed is much more different: neither LMS or full-wave simulations are involved. The beam-forming concept and implementation are inspired by [92].

In Fig. 5.9 it is shown the algorithm's block diagram, detailed as follows:

1. The opposite phase of the single-elements at θ_0 gives the corresponding weights' phases. Amplitudes are obtained from the ideal illumination
2. The set of weights is scaled until all elements are contained in the PGMs
3. The nearest PGM' states producing the desired weights are chosen
4. The far-field is calculated by superposition of single-element patterns
5. The SLL and main-beam direction of the pattern is retrieved
6. The phases in step 1 are shifted and steps 2 to 5 are calculated
7. The pattern with the lowest SLL & main-beam error is chosen

The first step of the beam-forming guarantees coherent addition of the radiation from/to every element. The subsequent steps are introduced in order to approach the optimum excitation of the antenna as good as possible. In addition, the algorithm is formulated so the highest active antenna gain is always obtained with a minimum pointing error, while achieving the required SLL. Furthermore, possible quantization errors of the PGM states selection are taken into account. They can be reduced, or counteracted, by applying a phase-shift to the ideal weights (step 6), which is in the order of magnitude of the T/R-module's achievable phase resolution.

A good agreement between measurements and predictions is obtained. This is an expected results, since the calibration process is counteracting better the inconveniences of the novel feeding network, which has visible effects on the measured single element patterns. Some examples of measured far-fields are shown in Fig. 5.10.

While this second model offers a rather accurate prediction of the scanned far-fields, the SLL in receive mode is still rather unsatisfactory. Therefore, an optimization routine based on this model (without further antenna measurements) is developed. Detailed explanation is provided in the following section.

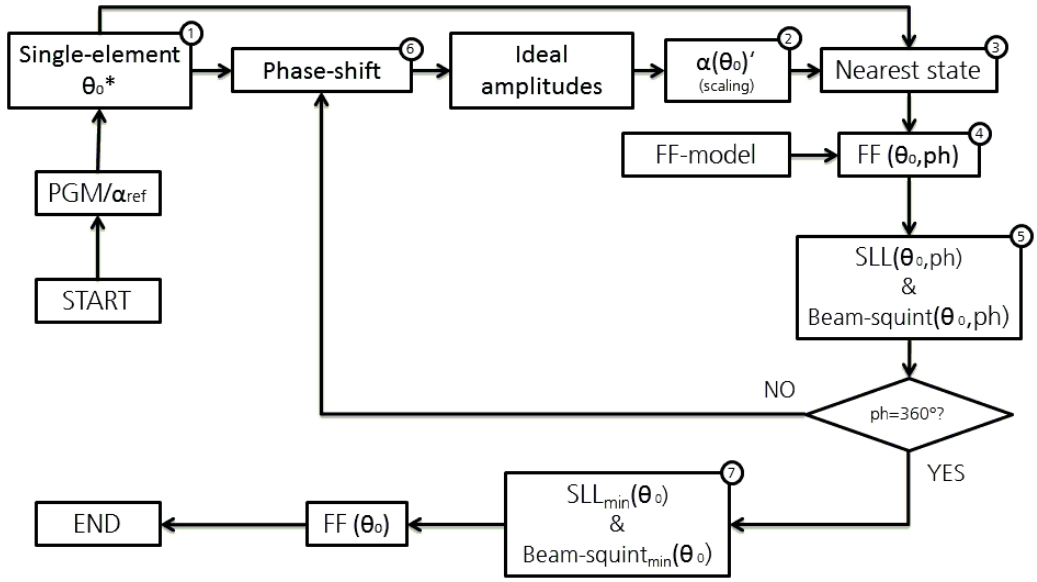


Figure 5.9: Beam-forming method based on far-field measurements.

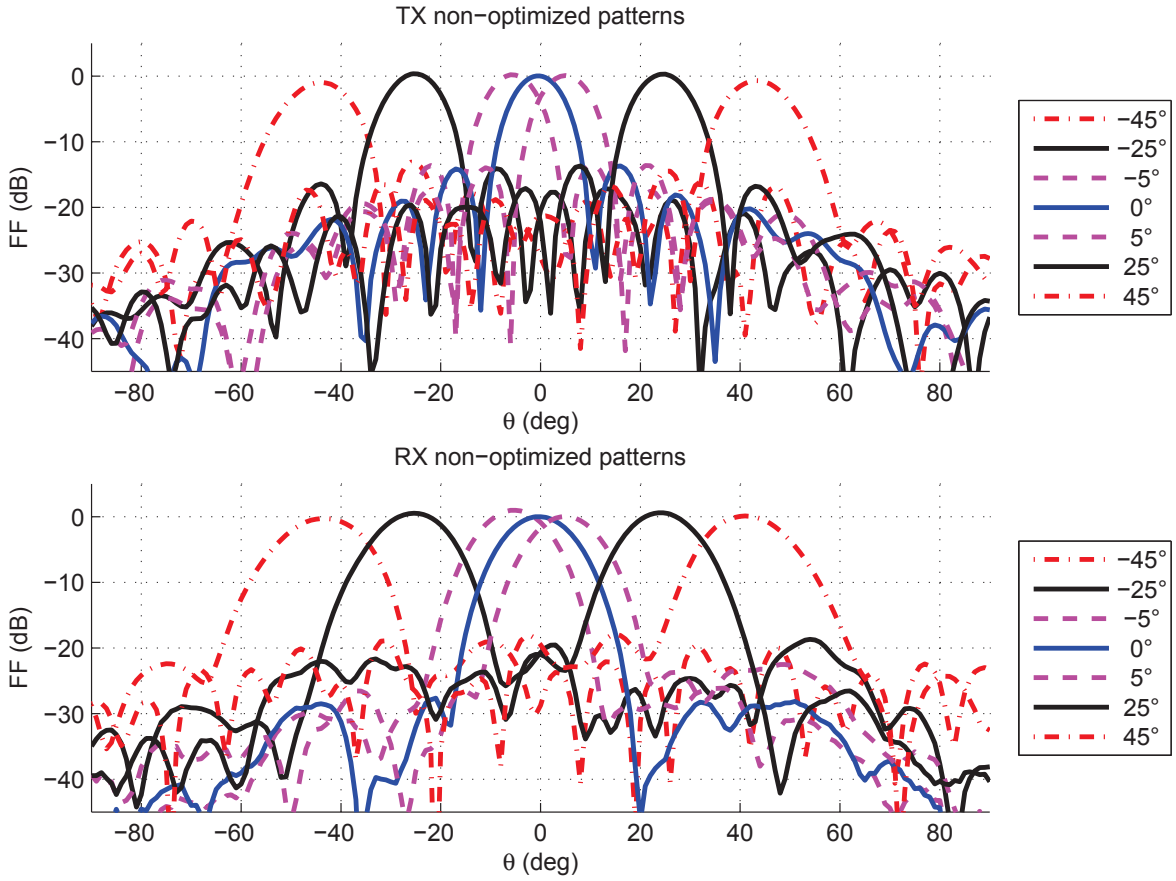


Figure 5.10: Directly measured transmit (top) and receive (bottom) radiation patterns for several main-beam angles. Original antenna weights (non-optimized).

5.3 Far-field based optimization

A good agreement between the simulated radiation pattern and the measured ones is obtained. This is a consequence of the radiation model based on far-field measurements, which can predict with accuracy the electronically scanned patterns. However, the obtained SLL is still unsatisfying, and minor pointing errors are measured.

The radiation model developed compensates/counteracts the effects of the particular feeding network into the measurement of the single element radiation patterns, which means a good accuracy in the prediction of radiation patterns of the complete array antenna. Consequently, an optimization routine exclusively based on this far-field model can allow to enhance the initial diagram synthesis. This optimization can be conducted off-line, and it does not depend on any further antenna measurements.

The optimization here proposed is similar to the near-field case, since it is based again on concepts presented in [91], [92]. The algorithm's implementation is shown in Fig. 5.11.

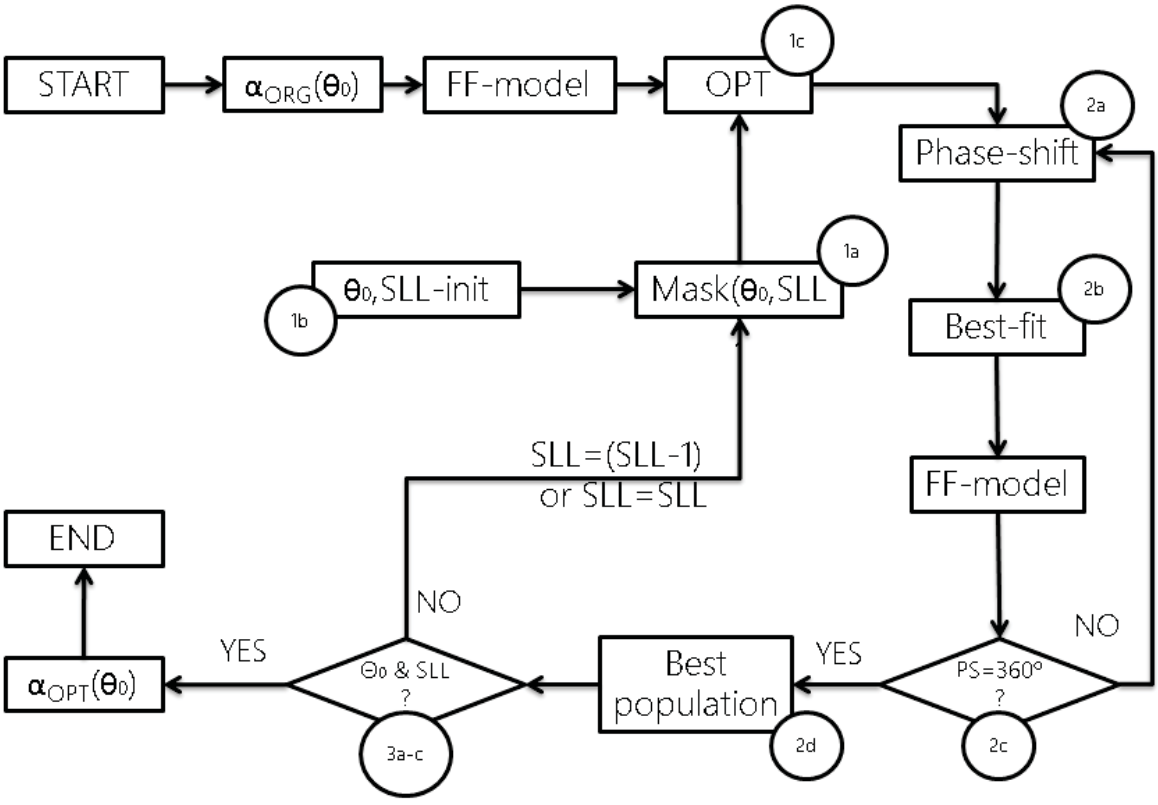


Figure 5.11: Far field off-line optimization sketch.

The optimization process can be explained as follows:

1. A gradient-based algorithm optimizes the radiation pattern until the given pattern mask is accomplished:
   (a) The pattern mask depends on the SLL and the main-beam angle
   (b) The algorithm is started with a SLL larger than the targeted one. This improves the convergence, since possible conflicts between SLL, HPBW and main-beam angle are mitigated
   (c) The weights are varied in the continuous complex domain
2. The population producing the most suited radiation pattern is chosen:
   (a) A phase-shift (in the order of the PGM phase resolution) is applied to the optimized (continuous) weights
   (b) The closest PGM states of each module are chosen (best-fit)
   (c) Phase-shift is applied until the initial population is obtained again
   (d) The population which produces the most suited pattern is chosen
3. The most suited radiation pattern is evaluated:
   (a) If the pattern accomplishes the targeted SLL (and the mask), the process is finished
   (b) If the pattern accomplish the mask, but not the targeted SLL, the SLL is decreased
   (c) If the pattern mask is not accomplished, the process is repeated with the same SLL

Measured post-optimized far-fields are depicted in Fig. 5.12, for both antenna modes and scanning from $-45°$ to $+45°$, with $20°$ step. The diagrams in transmit mode show a correct pointing direction, as well as a successful SLL. In receive mode, the main-beam angle error is negligible and the SLL is rather low; the targeted -30 dB is reached for the lower pointing directions.

The performance is comparable to results of the near-field optimization. However, this approach reduces (dramatically) the beam-forming time, at the price of a slightly longer calibration time.

Furthermore, it can be investigated whether lower receive-mode' SLL are possible, e.g. when the post-optimization routine presented in the near-field case is applied. The reduction of the SLL involves several aspects, which are discussed in the following section.

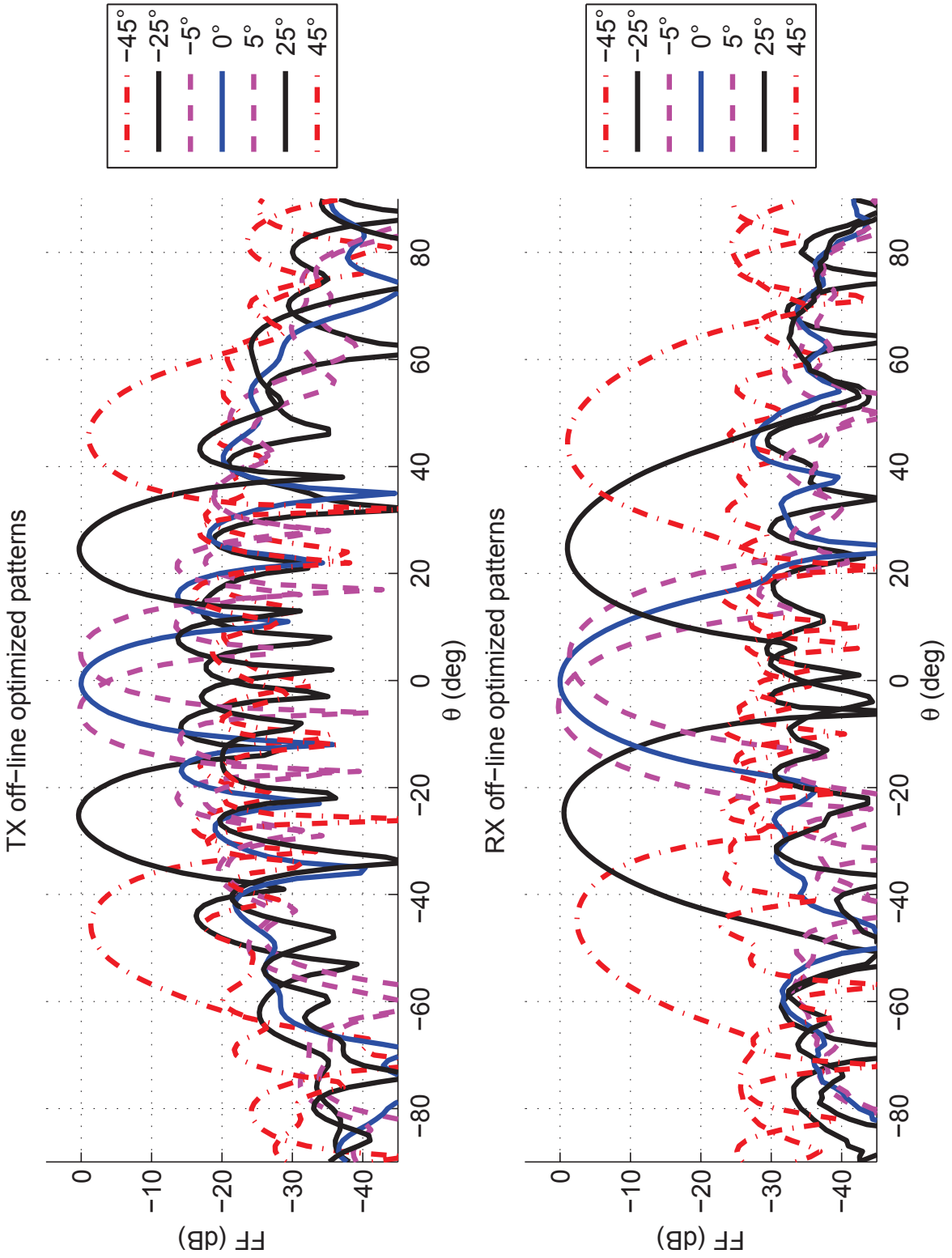


Figure 5.12: Directly measured transmit (top) and receive (bottom) radiation patterns for several main-beam angles. Antenna weights optimized off-line.

5.4 Far-field pattern optimization limits

First of all, it has to be considered the reduced amount of radiating elements. This introduces extra difficulties to realize the desired SLL in receive mode, mostly due to the relatively wide main-beam of the array factor and the weights quantization error, made by selection on the finite population of solutions (PGMs) [10], [32]. However, typically these effects can be compensated within certain limitations by optimization algorithms [93].

A good approach to determine the optimization quality is to compare the results obtained against reference diagrams. This reference patterns are obtained by simulations based on an *idealized* element pattern, the scattering parameters of the feeding network and the ideal beam-forming weights. In Fig. 5.13 are given exemplary comparisons of reference and measured radiation patterns. It can be observed that the measured SLL is lower than the reference, but at the price of a slight main-beam broadening.

Moreover, the reference SLL is generally higher than the specified -30 dB (see Fig. 5.13), since the feeding's network fixed aperture taper is different from the required square-root of Taylor taper. Consequently, respecting the condition of the feeding's reciprocal operation, the aperture's taper is not ideal any more. In this case, this non-ideal realized taper leads to radiation patterns such as in the examples in Fig. 5.13.

For the main-beam angles beyond $\pm 30°$, a low SLL starts to become problematic. This can be explained observing the reference radiation pattern: due to the taper and the reduce number of antennas, a grating-lobe appears early in the visible range, as shown by Fig. 5.13 (middle, bottom), $\theta \approx -80°$.

On the one hand, an *idealized* element pattern is being used to provide the reference diagram. On the other hand, the reduced number of radiating elements makes every radiation pattern slightly different from each other in the antenna demonstrator. The combination of the *non-equal* single-element radiation patterns can produce a reduction of the amplitude of the grating lobe. This can explain why when the radiation patterns are electronically scanned beyond $\pm 40°$, the grating lobe shown in the simulations is not clearly appearing in the measurements.

Furthermore, the dynamic range of the radiation pattern in receive mode is about 1:100 to 1:1000. Hence, when the measured patterns are compared against the ideal pattern predictions, the deviations observed can be considered negligible. Moreover, it is shown that the measured SLL is lower than the *a-priori* level given by the feeding's realized taper.

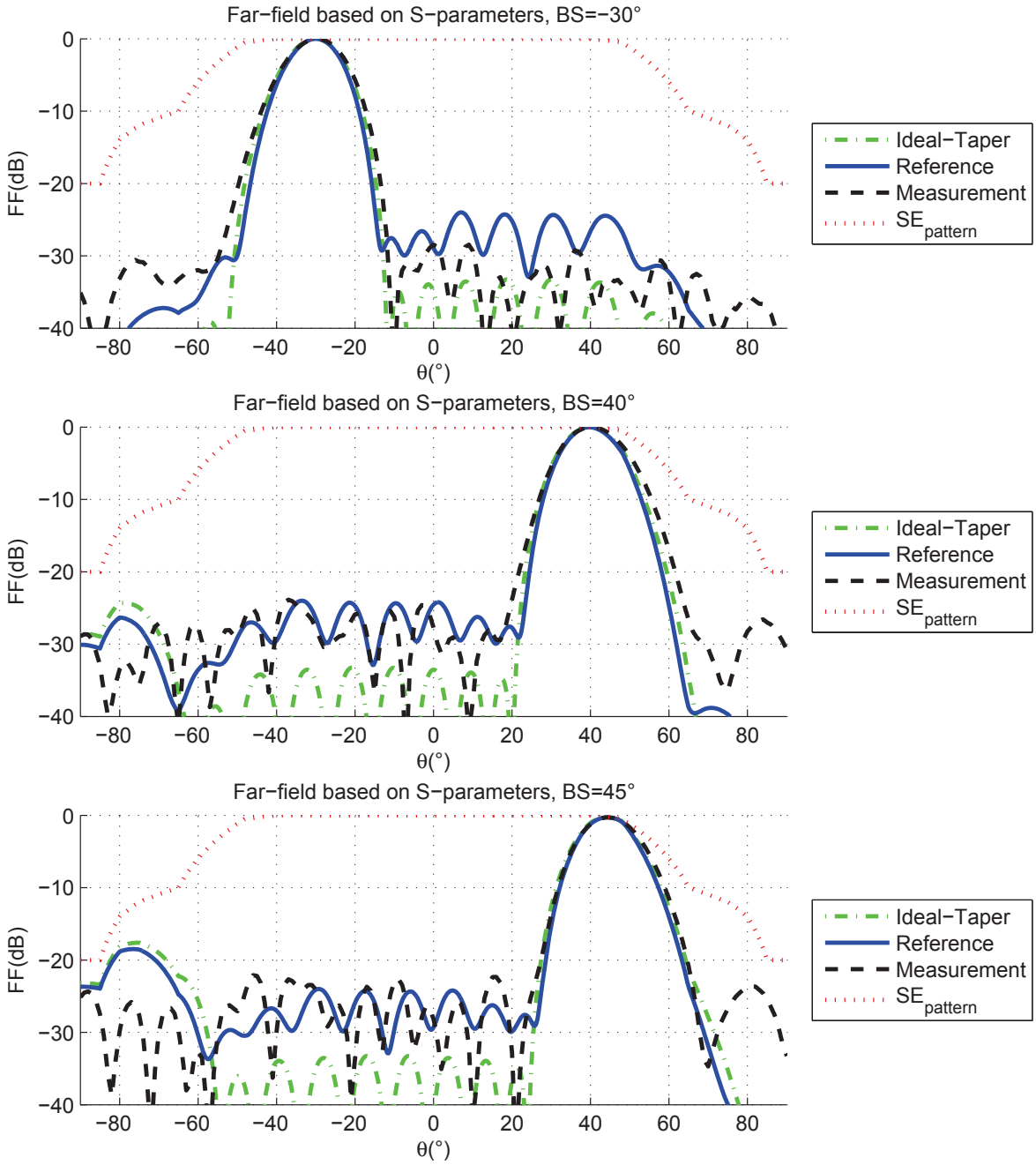


Figure 5.13: Comparison of measured and simulated radiation patterns for different main-beam angles. The SLLs of the measured far-fields are comparable to the reference patterns.

Furthermore, if the amount of radiating elements is increased, the performance should be better for high main-beam angle values, since:

1. The beam-width is reduced
2. The taper function is reproduced better (Chapter 3, paragraph 3.2)
3. The single element diagrams are much more similar
4. A larger array has an inherent larger degrees of freedom, which makes easier to compensate amplitude and phase errors made on the quantization of the beam-forming weights

Consequently, an operative AESA front-end, with about one hundred active antenna elements, can be expected to produced the required radiation patterns (with -30 dB of SLL in receive mode).

5.5 Feeding network role

This paragraph extends the discussion on the influence of the novel feeding network in the radiation pattern, in order to deepen in the understanding of the SLL limits for main-beam angles larger than $\pm 30°$.

Assuming a successful beam-forming, it is still to be discussed the behaviour of the novel feeding network (with highly coupled RF ports) in receive mode from a far-field point of view, and it has to be analysed the effects in the achievable SLL. As previously mentioned, in transmit mode the effect of the feeding is negligible. Nevertheless, in receive mode the network introduces difficulties within the calibration process. However, it has been demonstrated how to counteract these issues.

A different point of view is the active response of the antenna against plane waves hitting the front-end. On the one hand, when the main-beam is electronically scanned to a certain direction, the portions of the plane wave received in a narrow range around this angle are coherently added at the feeding's common-port. On the other hand, the role of the feeding network has to be taken into account for any other angle different to the main-beam direction.

5.5.1 Feeding network impact on the SLL

The influence of the feeding network, in the SLL of the radiation pattern, is briefly introduced. The behaviour of three different kinds of RF feeding networks is generally described.

Corporate feeding network made-up of Wilkinson-splitters. In the case of a corporate feeding network, e.g. build-up by Wilkinson-splitters in a tree-like structure, every T/R-module is compensating the progressive phase among the front-end, as well as internal small differences of its signal path towards the common port. This guarantees that all signals reach the summation port with the same phase and the desired amplitudes. Eventually, small differences, producing an *un-balanced* excitation of any Wilkinson-splitter in the structure, are to be absorbed by the internal resistors. When a plane wave with a different direction than the main-beam is received, this produces an *un-balanced* excitation of the Wilkinson-splitters. However, the internal resistors absorb the reflected waves. Consequently, it can be expected that the SLL is not strongly influenced by the feeding's network architecture.

Series feeding network made-up of Wilkinson-splitters. When this architecture is employed, every module has to compensate the progressive phase among the front-end, as well as the different electrical length towards the summation port. This can be counteracted in combination with the T/R-modules and delay/true-time-delay lines at every Wilkinson-splitter port. Furthermore, the *un-balanced* excitation of the elements from angles different than the main-beam is still present. However, the reflected waves are to be absorbed by the internal resistors in any case, resulting in negligible effects in the radiation pattern SLL.

Feeding network with highly coupled RF ports. The shown novel feeding network operation demonstrates that a non-inherently matched network, with highly couple RF ports, is perfectly matched when the feeding is excited reciprocally, and all the energy is summed-up at the feeding's network common-port (Chapter 2, sec 2.4). When the beam is scanned towards a certain direction, and a plane wave is received, the T/R-modules compensate the progressive phase to reciprocally excite the network, which guarantees coherent addition of waves at the summation port. When a plane wave is received from a different direction, the feeding operation conditions are not full-filled

any more, and reflected waves can be present at the feeding ports. Signals can be back propagated to the T/R-modules, and if the T/R-modules' reflection coefficients are sufficiently low, the reflected waves might be significantly absorbed. If the reflection coefficients are not sufficiently low, a significant amount of energy can be back propagated towards the network's common port. Consequently, a higher SLL level can be expected. These effects are analysed in the following section.

5.5.2 Proposed feeding network and the SLL

The last situation presented in the previous paragraph is the case of the AESA antenna demonstrator presented here: an AESA antenna comprising a feeding network with highly coupled ports, which in addition is implemented as a series structure. The behaviour of this architecture can be evaluated by means of an ideal antenna model, using the scattering parameters of the feeding network and ideal beam-forming weights. The modelling can be approached in several ways; here, two different analytical solutions are presented. An scheme describing both models is shown in Fig. 5.14.

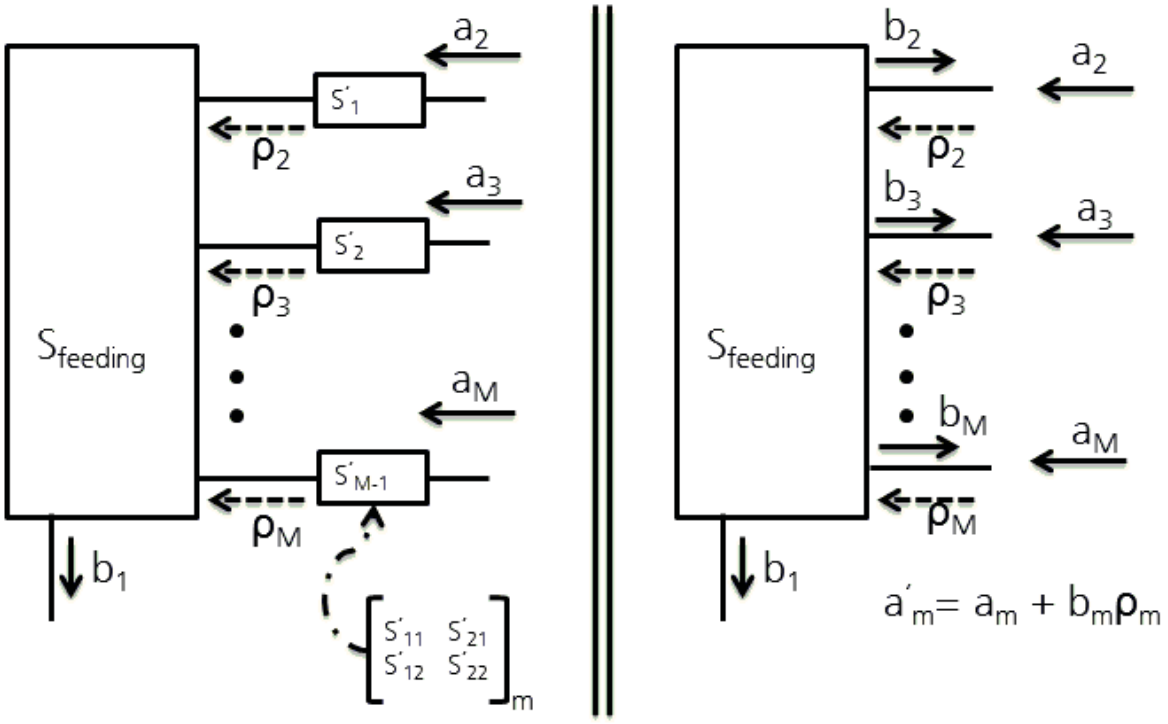


Figure 5.14: Antenna model, based on concatenation of scattering parameters (left) and back-propagated waves (right).

The first model is relatively plain: every feeding network port is loaded with an arbitrary passive component represented by its scattering parameters, offering a non-perfectly matched port, $|S_{nn}| > 0$. This allows to obtain the new scattering parameter matrix of the feeding by analytical concatenation of matrices.

The second model is more elaborated. This approach assumes an inherent reflection coefficient on the feeding's ports, adding a back-propagated wave to the excitation vector. Firstly, the ideal feeding network behaviour is:

$$\underline{b} = \underline{\underline{S}}\ \underline{a}, \tag{5.1}$$

where the original feeding network' scattering parameters is $\underline{\underline{S}}$, and $\underline{a}$ and $\underline{b}$ are the excitation and response vectors, respectively.

Secondly, it is assumed the presence of a back propagated wave, which is added to the excitation, $\underline{a}$, and it can be expressed as a function of the reflection coefficients of the network ports and the feeding network' response. It is proposed that a different overall response of the network is to be expected. It can be defined a new excitation vector which contains the reflected wave as follows:

$$\underline{a}' = \underline{a} + \underline{\underline{r}}\ \underline{b}'. \tag{5.2}$$

The last step applies the excitation from eq. (5.2) to the original scattering parameters of the network, eq. (5.1). Then, a feeding network response including the effects of the back-propagated waves is obtained, $\underline{b}'$:

$$\begin{aligned} &\underline{b}' = \underline{\underline{S}}\ \underline{a}' = \underline{\underline{S}}\ (\underline{a} + \underline{\underline{r}}\ \underline{b}') = \underline{\underline{S}}\ \underline{a} + \underline{\underline{S}}\ \underline{\underline{r}}\ \underline{b}' \implies \\ &\underline{b}' - \underline{\underline{S}}\ \underline{\underline{r}}\ \underline{b}' = \underline{\underline{S}}\ \underline{a} \Leftrightarrow [\underline{\underline{I}} - \underline{\underline{S}}\ \underline{\underline{r}}]\ \underline{b}' = \underline{\underline{S}}\ \underline{a} \Rightarrow \\ &\underline{b}' = [\underline{\underline{I}} - \underline{\underline{S}}\ \underline{\underline{r}}]^{-1} \underline{\underline{S}}\ \underline{a} \Leftrightarrow \underline{b}' = \underline{\underline{S}}'\ \underline{a}, \end{aligned} \tag{5.3}$$

where the vector containing the reflection coefficients needs to be dimensioned as a diagonal matrix, $\underline{\underline{r}}$, in order to allow the previous operations.

The first and the second model offer identical results, since they are representing exactly the same situation, but from different points of view. This modelling can be used to obtain the effects due to different reflection coefficients in the radiation pattern. This is done exciting the scattering parameter matrix, $\underline{\underline{S}}'$, with different plane waves and using ideal beam-forming weights.

An exemplary simulation, for a main-beam angle of $\theta_0 = 0°$, is depicted in Fig. 5.15 (top). The simulation results show that for relatively high reflection coefficients, -10 dB, the radiation-pattern' SLL is already increased. Similar results are obtained for other main-beam angles (Fig. 5.15, middle).

As mentioned above, it is expected that the SLL increment is mitigated by lower reflection coefficient values. Simulation results with a reflection coefficient of -15 dB are proving this assumption (Fig. 5.15, bottom).

The measured far-field do not appear to strongly suffer from this effect. Moreover, the T/R-module is optimized to provide the best matching possible among almost any operational conditions. Nevertheless, the slight deviations are probably a combination of the feeding network effects and the several issues mentioned within this work (e.g.: discrete beam-forming weights, reduced number of antennas, measurement inaccuracies or the high dynamic range of the radiation patterns in receive mode). Three conclusions can be obtained from this analysis:

1. The SLL inherently given by the (non-ideally realized) taper of the feeding network is improved

2. The previous result (1) can only be achieved if the reflection coefficient at the feeding network ports is sufficiently low, in order to mitigate the adverse effects (due to the special feeding network) on the SLL

3. Considering low degrees of freedom (reduced amount of elements), the diagram synthesis offers successful results

Therefore, the beam-forming results shown demonstrate not only the feasibility of the novel and challenging AESA antenna architecture, which comprehends a novel feeding network with highly coupled ports and inexpensive T/R-modules, but also validates the novel calibration, beam-forming and optimization methods developed, in order to account for the special AESA antenna architecture.

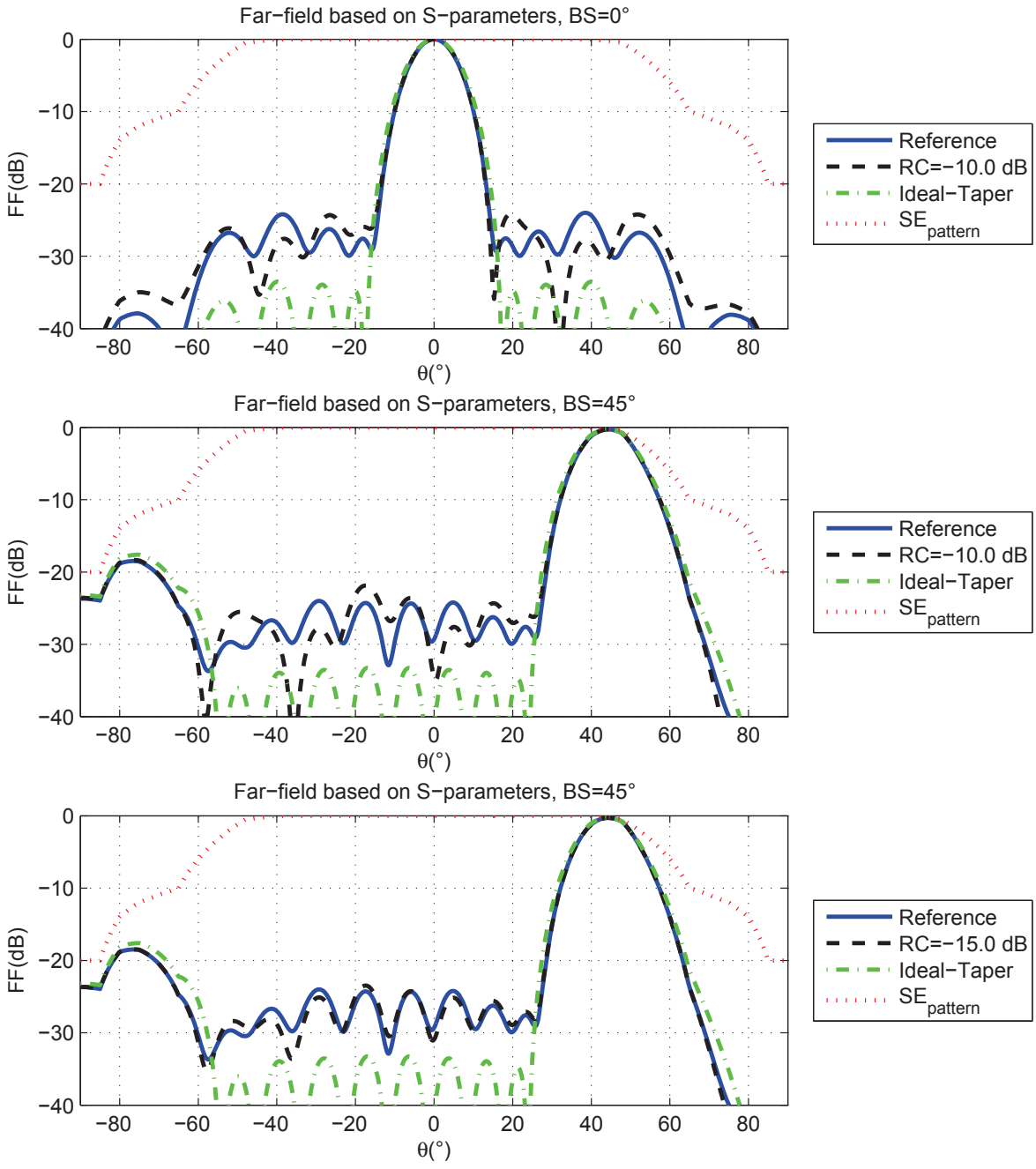


Figure 5.15: Comparison of simulated and measured radiation patterns, showing the influence of the T/R-module's reflection coefficient on the SLL.

Chapter 6

Receiver protection

6.1 Introduction to receiver protection

Nowadays, the electromagnetic spectrum is heavily populated. There is a vast number of applications taking advantage of the use of RF front-ends [94]. This generally imposes protection mechanisms at RF receivers against other radiating systems (interferences), specially in the case of sensitive receiver chains or front-ends. Besides, in densely populated scenarios, such as in harbours, it can be expected a large amount of interference sources: WiFi systems, GSM communications, traffic surveillance radar, short-wave and long-wave radio are a few examples. For these reasons, receiver protector techniques are a key aspect of radar systems [59].

In general, it can be said that a radiating system may produce two major kind of effects into a radar receiver: performance degradation and system damage. Obviously, the most important task in receiver protection is to avoid permanent system damage under any conditions (*keep-alive*). Consequently, it is a secondary, but still relevant task, to guarantee system performance. When the target is to maintain system performance and reduce the disruptive effect of the interference, the techniques to be applied are known as electronic counter-countermeasures (ECCM) in the military market [28], [59].

Mostly, ECCMs require a high system complexity and cover a wide variety of techniques, which involve complex RF hardware and advanced signal processing techniques. This kind of techniques, ECCMs, cannot be considered in a system such as the one presented here. In any case, a *keep-alive* mechanism is always to be included in a radar receiver, while maintaining operability.

The first part of the chapter introduces the topic of interference sensitivity and system protection, but from the point of view of the AESA antenna demonstrator shown in this work. The purpose is to analyse the front-end's sensitivity to interferences, in order to address the receiver protection mechanism of the front-end.

This is necessary, because the antenna does not include any protection technique. Moreover, state-of-the-art techniques produce an excessive cost increment, since every active element (T/R-module) of the AESA antenna needs its own protection mechanism. Therefore, the overall costs of the front-end can make the approach infeasible for civil phased-array applications. These reasons conduct to an interference experiment in a controlled environment, in this case in an anechoic chamber. By means of this experimental set-up, it is shown how the front-end performance can be easily and severely deteriorated by an in-band or an out-of-band interferer. This is an expected result, since, as mentioned above, the AESA antenna demonstrator does not include mitigation/cancellation mechanism against interferences.

In the experimental analysis, representative (interference) carriers are sent against the AESA front-end, and, at the same time, far-field radiation patterns are measured. It is estimated, by plain numerical modelling, that the power levels reaching the front-end generate a signal strength in the antenna's active elements far below the maximum power admissible by the sensitive TRM-ICC (+5 dBm), included in the T/R-modules [95], which is the first active element in the receiver chain. Besides, the power received at every T/R-module is approximately 10 dB lower than the 1 dB compression point of the complete module (−21dBm) [95].

Despite of the rather low powers used in the experiment, noticeable degradation of the AESA antenna performance in receive mode can be observed. Consequently, a receiver protector which guarantees system survival and maintains system performance, up to a certain extend, is demanded.

The last part of this chapter approaches the design of a suitable receiver protector. It has to be considered the restricted cost of the system, therefore, the techniques to be applied are as well very restricted. In a first step, State-of-the-Art techniques that can be used in order to accomplish the required system protection are evaluated. Finally, an innovative receiver protection approach is proposed and analysed.

6.2 Sensitivity to interferences

The experimental T/R-module shown (Chapter 3) is a challenge for the front-end's realization, not only from an implementation point of view, but to define which measures or mechanisms can be necessary to mitigate interferences effects on the T/R-module, and consequently on the antenna front-end.

Therefore, the front-end's sensitivity to interferences should be evaluated. For this purpose, a dedicated interference experimental analysis is carried out at an anechoic chamber, where a secondary illumination pointing towards the AESA antenna is deployed, representing a source of interference. The proposed set-up allows to observe the qualitative response of the demonstrator when a second source is present in an interference free and very controlled environment.

6.2.1 Interference experimental set-up

This section describes the experimental set-up where the qualitative interference sensitivity of the AESA antenna is evaluated. A wide range of frequencies is to be covered, since there is a dense population of potentially harmful systems. A representative list of different systems, and their designated frequency bands of operation, is offered in [94]. The ones considered as the most harmful, for the given AESA front-end, are listed in Table 6.1.

Table 6.1: Selected interference frequencies

Application	**Band**	f_0 **(GHz)**
GSM800	L-band	0.80
Radar & Communications		1.40
GSM1900		1.90
Radio/Mobile/Satellite	S-band	2.35
WiFi b/g		2.45
GSMA		2.60
Maritime navigation radar		3.00
Communications		3.40
Satellite	C-band	5.30
WiFi a		5.50
Satellite		7.80
Maritime navigation radar	X-band	9.25
Communications		10.25

An scheme and a photograph of the measurement set-up are shown in Fig. 6.1 and Fig. 6.2, respectively. For operational reasons, the location of the second illumination is very limited. However, this configuration is sufficient to address a qualitative analysis. The reference antenna (main illumination) is kept fixed, while the AESA antenna is rotated by a turning table.

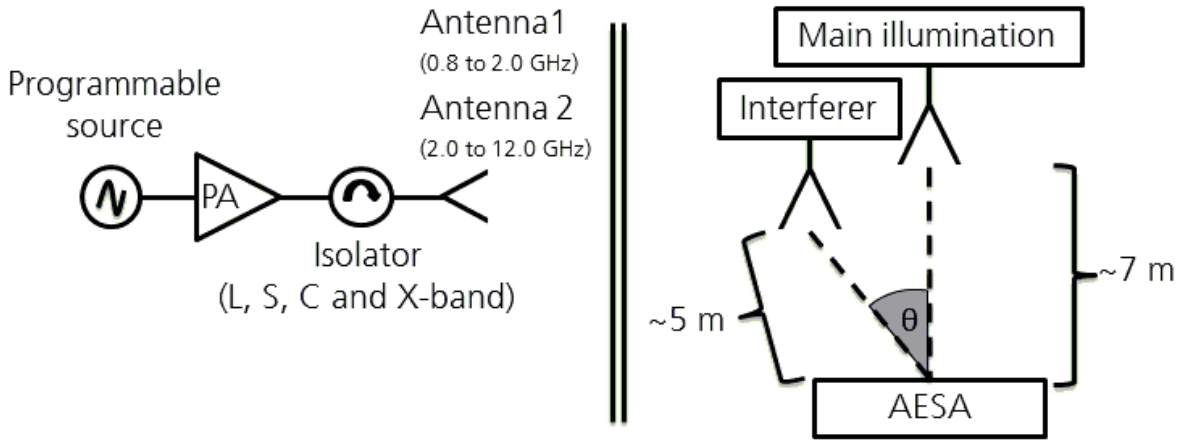


Figure 6.1: Scheme of the interference sensitivity experiment, showing the CW interferer concept (left), and the complete experimental set-up (top view, right). The interferer is placed at approximately 10° to the left of the AESA antenna.

Most of the devices required for the interference generation are located out of the chamber, in order to preserver the chamber's environment. Simultaneously, a relatively high power is desired at the secondary antenna's feeding, in order to ensure a significant effect on the front-end operation. Moreover, there are several elements of the set-up (e.g. cables, connectors or antennas) that behave differently depending on the operational frequency. Therefore, the hardware parts that can significantly reduce the performance, depending on the frequency, are to be exchanged: the interferer antenna and the isolator. In addition, the T/R-module components need to be preserved/protected (there are not *keep-alive* mechanisms), and it would be desired a constant received power from every CW interference signal, for a better comparison.

For these reasons, data-sheets, measurements and numerical models are combined to estimate the power received by a single T/R-module. A relatively constant level (−30 dBm) is predicted when the generator output power is set to 0 dBm, as observed in Fig. 6.3. Besides, the power level received at every T/R-module is approximately 10 dB lower than the TRM-ICC's saturation point [95].

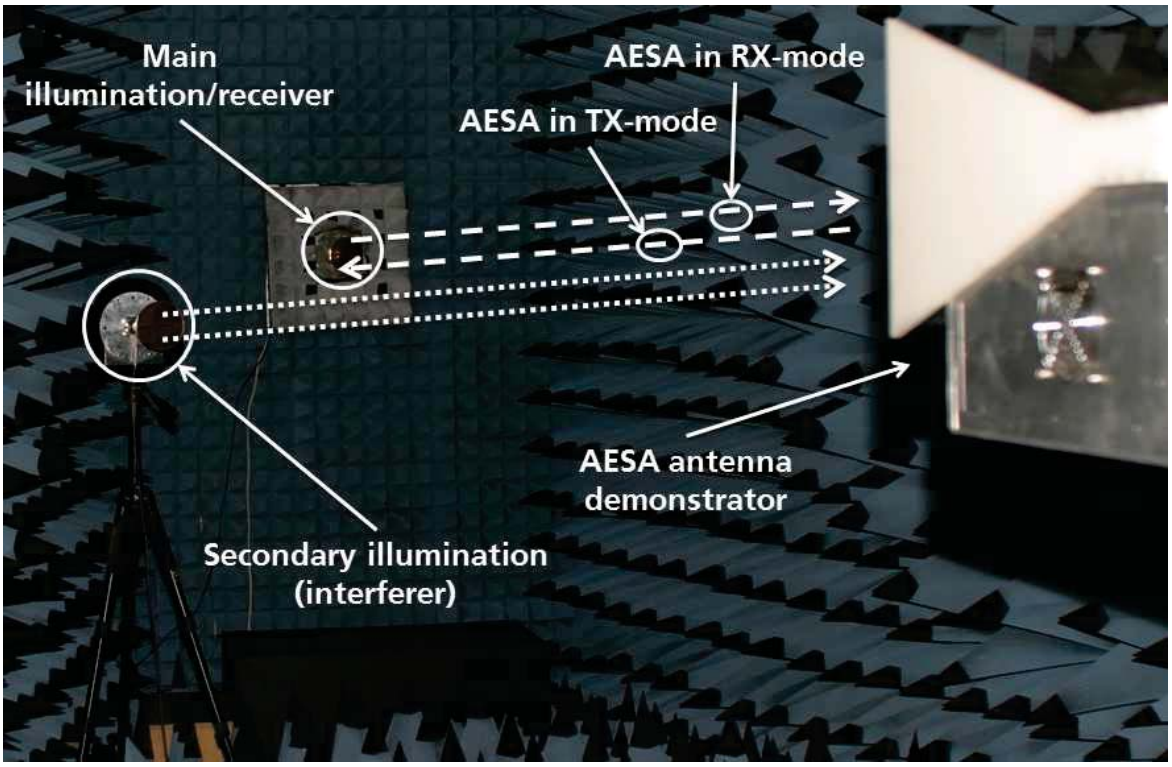


Figure 6.2: Photograph of the interference experimental set-up. The three main elements of the experiment can be seen: the main illumination, the interferer and the S-band AESA demonstrator.

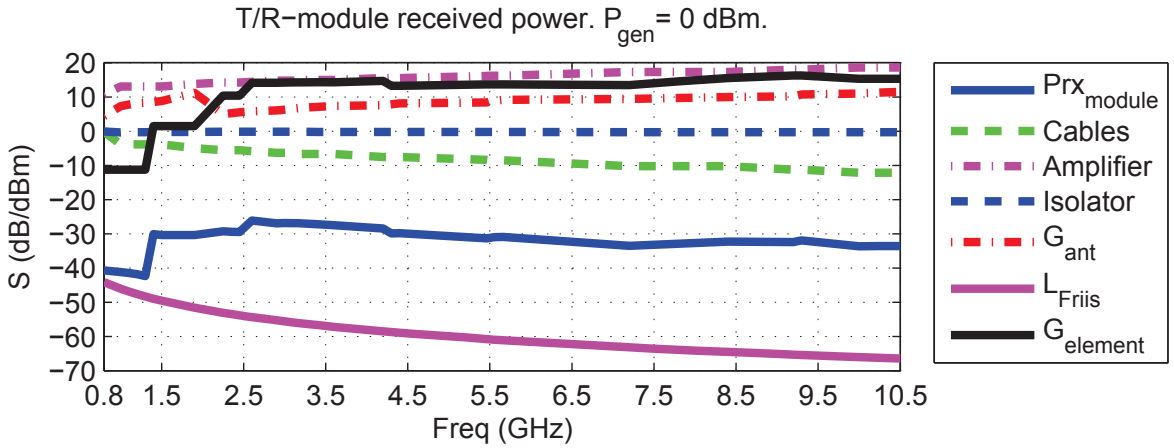


Figure 6.3: Simulation results of the estimated RF power received by every T/R-module, Prx_{module}. The power of the generator, P_{gen}, is set to 0 dBm. The gain of the demonstrator's antenna element is obtained from full-wave simulations, $G_{element}$. The response of the rest of the components is obtained from either data-sheets or measurements.

Furthermore, when the TRM-ICC is operated in receive mode it behaves as a very sensitive LNA. Therefore, it can be expected that the combined filtering effect of the antenna and its monopole feed will be not enough to avoid the following two effects:

1. In the case of a low-power interference, which may not saturate the LNA, the amplification of the interfering signal would produce a lack of amplification of the desired signal, which is typically very low power in a radar system, since most of the LNA power would be used in the amplification of the dominant signal

2. In the case of a high-power interference, which may saturate the LNA, any amplification of the desired signal would not occur, resulting in system *blindness*

These effects can appear in measured radiation patterns, if an interfering source is inside the anechoic chamber while the measurement is taken. It is expected that the beam-forming weights performed by every TRM-ICC can be highly distorted, introducing phase and amplitude errors.

For the sake of simplicity, the electronic steering of the antenna's main-beam is fixed to $\theta = 0°$ in both antenna modes. In addition, the front-end's radiation pattern is measured only at 3000 MHz, while the several different CW interference frequencies are successively transmitted towards the demonstrator. Meanwhile, the demonstrator is rotated to obtain the far-field radiation pattern.

Moreover, the phase of the interference's source is phase-locked with the measurements VNA. It is assumed as the worst-case scenario when the interference and the antenna RF sources are coherent, although it may occur very rarely. Besides, the stability of the experimental results is guaranteed, since the relative phase between the interferer source and the antenna source is kept stable, even though both RF sources have different local oscillators.

6.2.2 Experimental results

It can be expected that the behaviour of the AESA antenna is rather different depending on the operational mode, transmit or receive. In the transmit case, in most of the cases the power chain of the antenna will generate more power than any incoming interference. In addition, it is assumed that the

reflection coefficient of the amplifiers will strongly reflect any incoming wave. In the receive case, the lack of interference mitigation mechanisms, combined with the experimental components of the T/R-modules, can lead to a highly unpredictable behaviour of the antenna. Therefore, the analysis of the effects of interferences is conducted separately for every front-end mode. The following two paragraphs present and analyse the experimental results, firstly in receive mode, and secondly in transmit mode.

Receive mode

The antenna is very sensitive in receive mode: there is not a mitigation mechanism of interferences. Mostly, it is observed a degradation of the SLL in the upper part of the frequency range of the experiment, as depicted by the examples in Fig. 6.4 (top). This would mean a minor loss of performance into the front-end's receive mode operation.

In other cases, mostly in the lower frequency range, in addition to the SLL degradation, it can be observed a significant loss of main-beam amplitude. Some examples are depicted in Fig. 6.4 (middle and bottom). These effects can be considered as a high performance degradation, since the distortion into the radiation pattern will translate as a loss of detection range into the radar operation.

Additional analysis is required for the measurement results obtained for CW signals at 1000 MHz (f_{ha1}) and 1500 MHz (f_{ha2}), shown in Fig. 6.5. On the one hand, the fundamental signals from these components, as well as the first harmonic from f_{ha1}, cannot propagate through the front-end, since their frequencies are below the cut-off frequency of the feeding network's waveguide. On the other hand, those frequencies can produce the excitation of harmonics inside the front-end's frequency band of operation. The first and third harmonic of f_{ha2} and f_{ha1}, respectively, can propagate trough the feeding network since they are above cut-off. Hence, it is concluded that the radiation patterns whose main-beams are centred at the position of the interferer (see Fig. 6.5) are the result of the excitation of harmonics in the TRM-ICC by the interferences at f_{ha1} and f_{ha2}.

The measured power levels of the interfered patterns, as a result of the excitation of harmonics in receive mode (see Fig. 6.5) is much higher than the fundamental one (at 3000 MHz), since the transmit power levels of the interference signals are 30 to 40 dB higher than the power level of the main illumination.

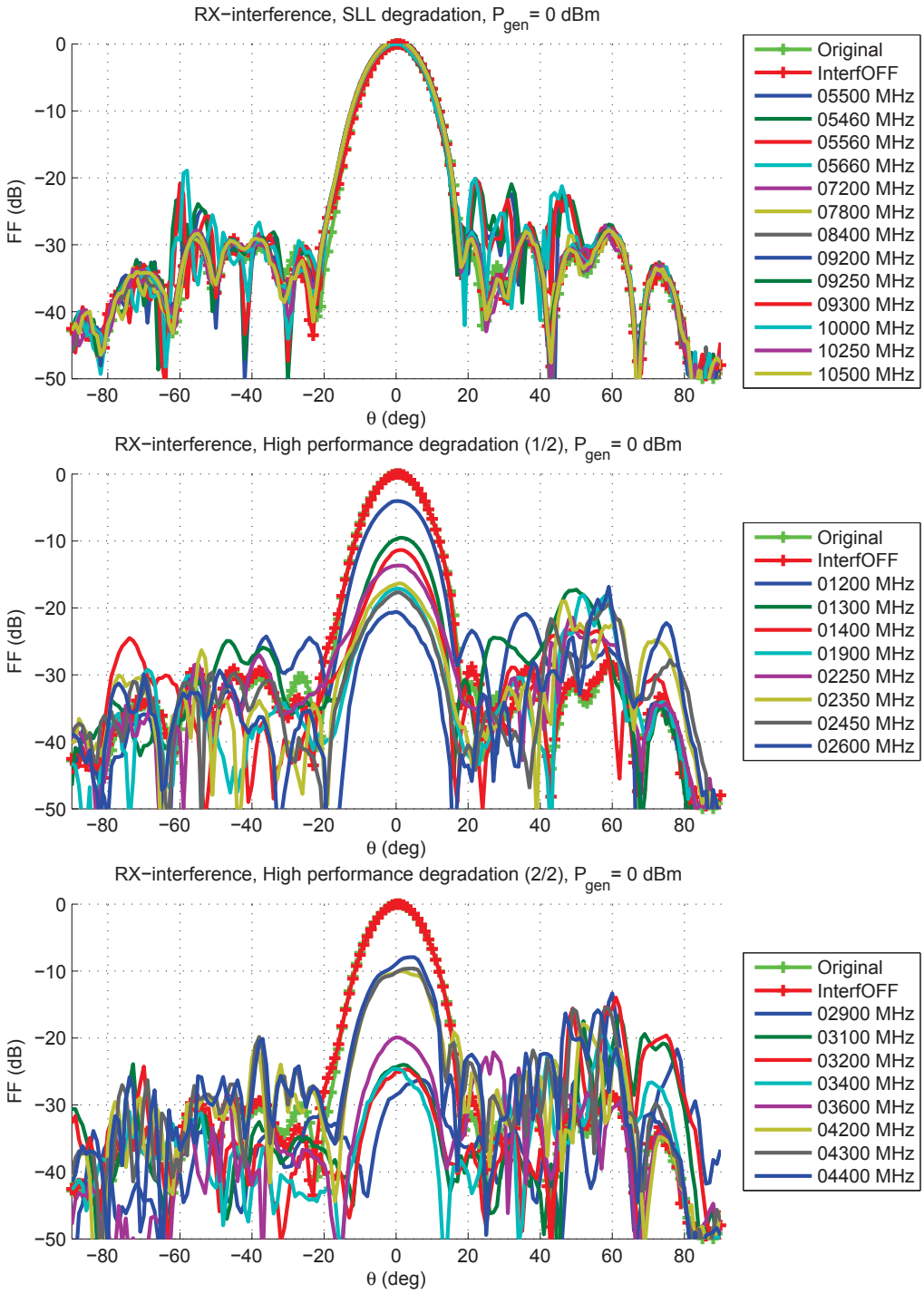


Figure 6.4: Radiation patterns in RX-mode showing the degradation on the main-lobe and the SLL (middle and bottom), depending on the frequency of the CW interference. For better comparison, the original pattern with and without the second illumination in the chamber are depicted in green (*Original*) and red (*InterfOFF*), respectively.

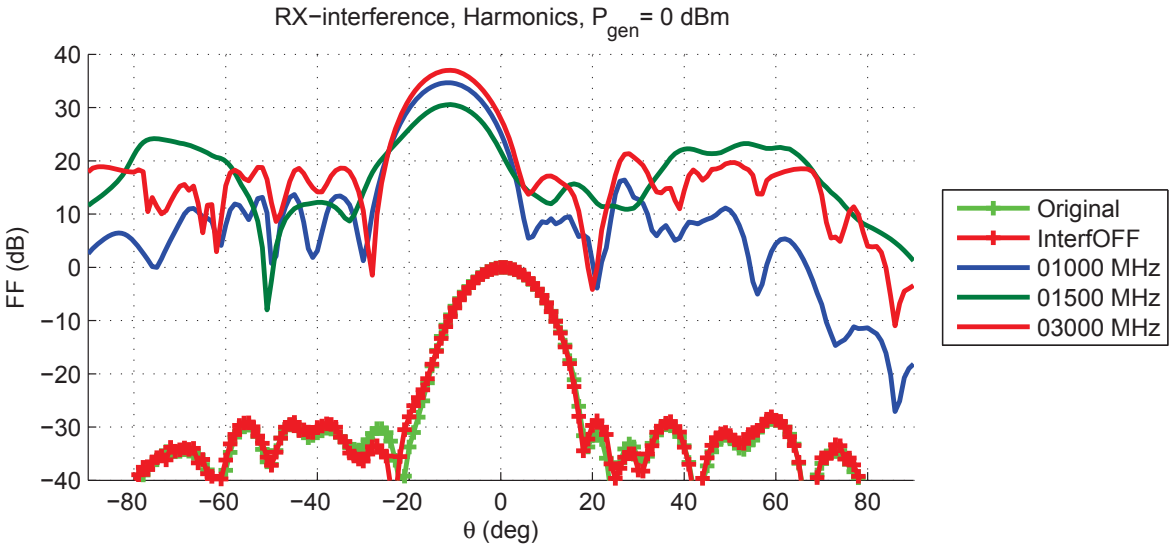


Figure 6.5: Radiation patterns in RX-mode demonstrating the excitation of TRM-ICC harmonics. For better comparison, the original pattern with and without the second illumination in the chamber are depicted in green (*Original*) and red (*InterfOFF*), respectively.

Transmit mode

The effects of CW interference in the transmit mode are negligible, as it can be observed in the measurement results depicted in Fig. 6.6. These are expected results, since the received power levels of the interference signals are 50 to 60 dB lower than the T/R-module's transmit power level. At some frequencies there are slight variations of the SLL, that can be explained from the mutual coupling between the two illuminations.

In addition, as mentioned above, the transmit chain of the T/R-module architecture allows to offer a significantly high reflection coefficient to any incoming wave, which is consequently producing the back-scattering, or rejection, of interferences without distortion into the T/R-module's operation. Moreover, the transmission from the PAs to the RF feeding port through the TRM-ICC is very low, which provides a high isolation from the antenna towards the feeding network. Besides, the antenna port of the module and the TRM-ICC are isolated with about 33 dB. Therefore, the measurement results are consequent with the designed behaviour of the AESA antenna architecture.

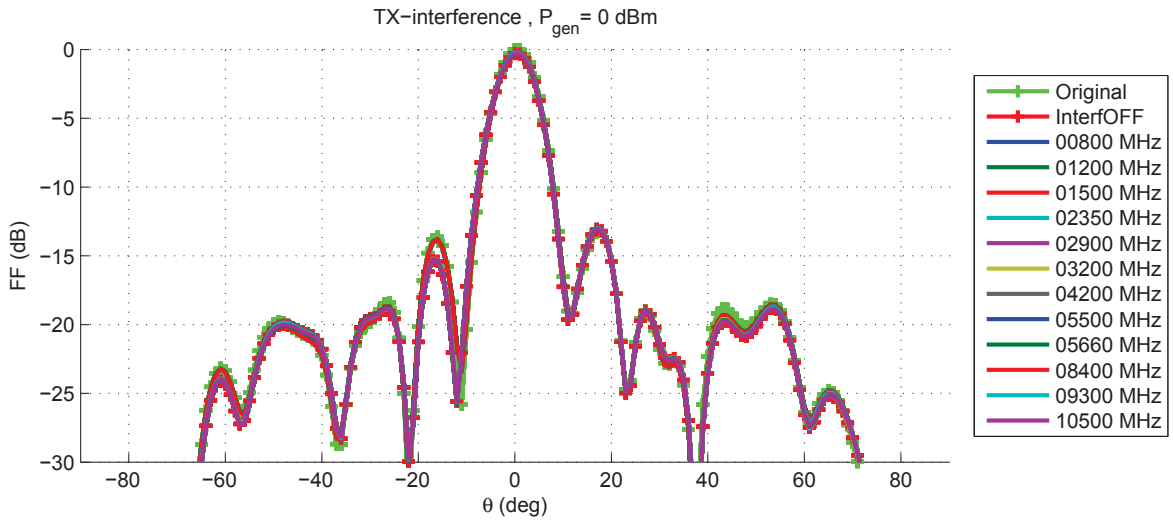


Figure 6.6: Radiation patterns in TX-mode showing no influence of the interferences, demonstrating the immunity of the front-end in transmit mode. For better comparison, the original radiation patterns with and without the second illumination in the chamber are depicted in green (*Original*) and red (*InterfOFF*), respectively.

6.3 State-of-the-Art receiver protectors

The analysis presented in the previous paragraph is carried out as an exploratory (qualitative) task, that can help in the decisions to be made in the receiver protector design. It has been possible to determine a set of frequencies which clearly affect the antenna performance in receive mode, and at the same time, validate the interference immunity of the front-end in transmit mode. The necessary compromise between permanent damage protection, overall front-end performance preservation, costs and the protector design approach are discussed in the following paragraphs.

The most common receiver protector techniques that can be found in literature are transmit-receive tubes (TR-tubes) or TR-limiters [96], [97], as well as solid-state based protectors [98–101]. The protective solution choice can be difficult, due to the broad spectrum of technologies, but unfortunately, due to the overall cost restrictions of the system, the protection techniques that can actually be used are very limited.

The cost issues reduce the technological choices to only two protection techniques: planar limiters based on PIN diodes [102] and band pass filters (BPF). Furthermore, these two techniques are to be combined, since a BPF

provides protection for out-of-band frequencies, and a planar limiter can be optimized for in-band frequencies [99,100,103,104]. Applying these concepts, it is possible to guarantee system survival as far as the interferer is not capable to damage the first stage of the protector.

The highest inconvenience of PIN diodes is the widely extended bond wire montage, which represents a high fabrication cost. Alternatively, surface mount packaged PIN diode based limiters can allow to lower the fabrication cost [101,102,105,106]. In the opposite way, the components costs itself make the approach *un-practical* for this S-band AESA antenna concept. However, PIN-diode power limiters are the most suited State-of-the-Art approach for this application. Furthermore, recent investigations on III-Nitride based limiters fabrication techniques can enable this technology for cost-restricted applications [107]. Unfortunately, the technique is still immature, and its benefits and drawbacks are undetermined.

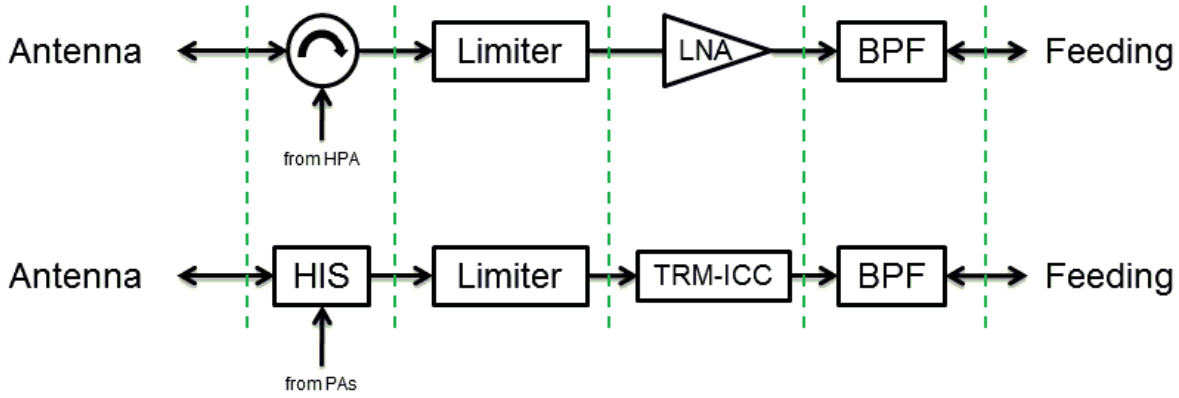


Figure 6.7: Basic receiver path, including the proposed elemental receiver protection. On the top for a generic case, at the bottom for the considered S-band AESA antenna.

In Fig. 6.7, the T/R-module receiver chains of a general case and the particular AESA antenna considered here are compared, in the path from the antenna aperture to the feeding network port. The first element that should be placed to protect the TRM-ICC is a *keep-alive* power limiter. Nevertheless, performance degradation due to low power signals (as observed in Fig. 6.4 and Fig. 6.5) cannot be avoided with this technique.

The following element, immediately after the TRM-ICC, should be a BPF. This way, signals (harmonic or fundamental components) excited in the TRM-ICC outside of the front-end's operation band (2.90 GHz to 3.10 GHz) will be filtered-out or highly mitigated. Moreover, since the losses introduced

by the filter are placed after the relatively high amplification of the TRM-ICC, the effects on the receiver's noise-figure are negligible.

The main disadvantage of this protection architecture is that the excitation of harmonics at the operation band, around 3.0 GHz, will not be reduced. The main advantage of the configuration is that the survival of the receiver chain is guaranteed, with a minimum impact in the module's noise-figure. However, this configuration can be enhanced with plain RF principles, which allow to present an innovative receiver protection mechanism.

6.4 Novel receiver protector

As mentioned above, the BPF should be placed after the TRM-ICC, since the noise-figure of the receiver needs to be preserved. Here, it is proposed a novel solution to preserve the noise-figure of the receiver chain, while avoiding system damage and improving the frequency selectivity of the receiver path. In the following two paragraphs the proposed solution is explained and discussed.

6.4.1 Protector concept

In this paragraph, a novel and inexpensive protection mechanism is explained in four steps. This approach can allow to develop radar receivers without expensive power limiting/protection stages, which in the case of AESA antennas translates into a high reduction of costs, since every active element (T/R-module) is to be equipped with its own individual receiver protection.

First step

Firstly, an elementary solution to improve the frequency selectivity of the receive path is presented. This can be achieved by introducing a $\lambda_g/4$ short-circuited shunt-stub in the input line going towards the T/R-module. An sketch of this configuration is shown in Fig. 6.8.

Out of the narrow band where the shunt-stub offers an electrical open to the input line, incoming waves encounter a high mismatch. Besides, most of the energy is reflected back to the input port. Furthermore, the effect on the transmission at the desired frequency band is negligible. Therefore, this circuit allows to obtain a low order band pass filter behaviour, with

the introduction of very low losses. At the same time, it is avoided the introduction of intricate and/or lossy structures.

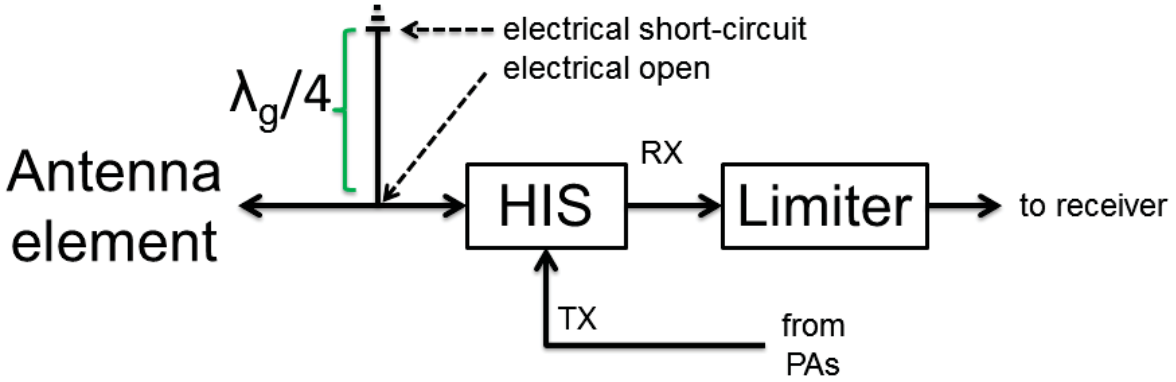


Figure 6.8: Receiver path with elemental receiver protection and a shunt-stub in the input port, immediately in front of the switch. The short-circuit at the end of the shunt-stub is translated into an open at the feeding point, in the RF input line. Therefore, the effect of the shunt-stub is negligible at the adjusted frequency.

Second step

Secondly, the application of plain RF concepts can further enhanced the configuration shown above. Here, it is proposed to use the concept shown by the circuital sketch in Fig. 6.9.

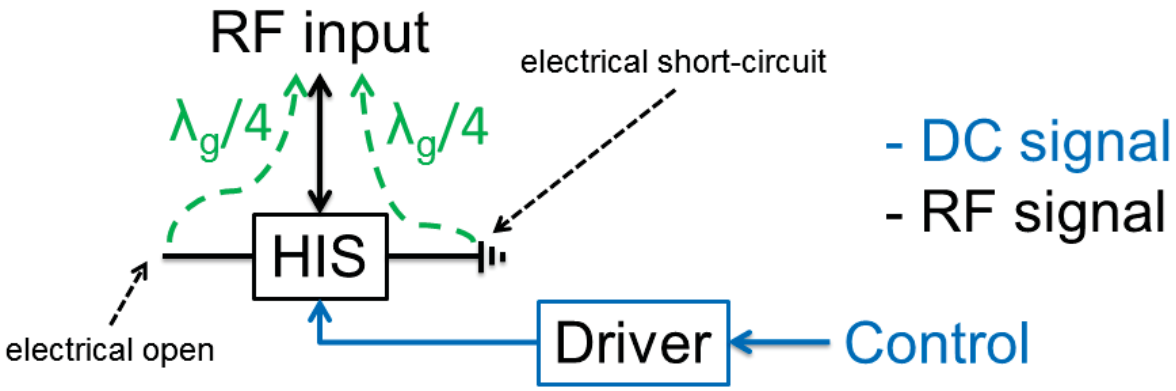


Figure 6.9: High isolation switch offering an electrical open or an electrical short, depending on the control signal.

A high isolation switch (like the one replacing a circulator in the T/R-module) is connected to an electrical open in one port, and to an electrical

short-circuit in the other port. Therefore, only RF signals can be fed at the common port of the switch (*RF Input* in Fig. 6.9). The switch's state is controlled with an external DC signal. The length of the RF lines can be carefully tuned, in such a way that, depending on the state of the switch, the input port offers either an electrical open or an electrical short-circuit.

Third step

Thirdly, the control signal of the switch shown in Fig. 6.9 can be triggered accordingly to the power received by a Schottky detector diode [108], as shown in Fig. 6.10. This way, depending on the power detected by the Schottky diode, it can be offered an electrical open or an electrical short-circuit at the switch's input port.

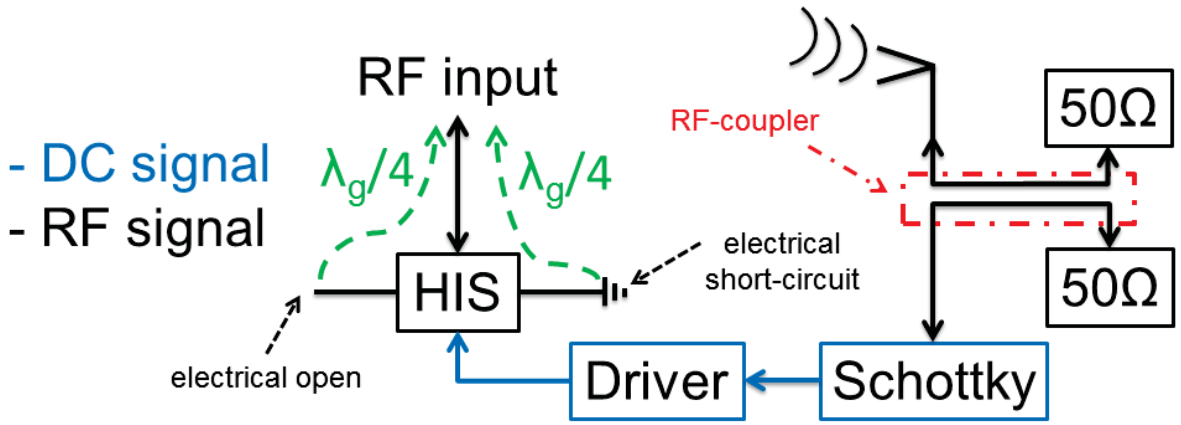


Figure 6.10: High isolation switch offering an electrical open or an electrical short, depending on the power detected by a Schottky detector diode.

Final step

Finally, the first circuit presented can be recalled (Fig. 6.8). In that sketch, it is proposed that a shunt-stub is introduced at the RF line connecting the antenna element and the T/R-module, in such a way that an open circuit is offered only at the frequency of interest. The shunt-stub, terminated in a RF electrical short-circuit can be replaced by the last circuitry, as shown in the receiver chain of Fig. 6.11.

This set-up allows to short-circuit the input line of the T/R-module when the driver circuit is triggered by an external RF signal. The RF coupler and

the detector diode can be adjusted, so it is possible to reject signals with previously fixed power levels, that would trigger the switch in order to offer nearly total reflection to the incoming wave. Furthermore, if the external RF signal power is not sufficient to trigger the driver, the T/R-module input line will be loaded with an open, resulting in a negligible effect into the receiver path.

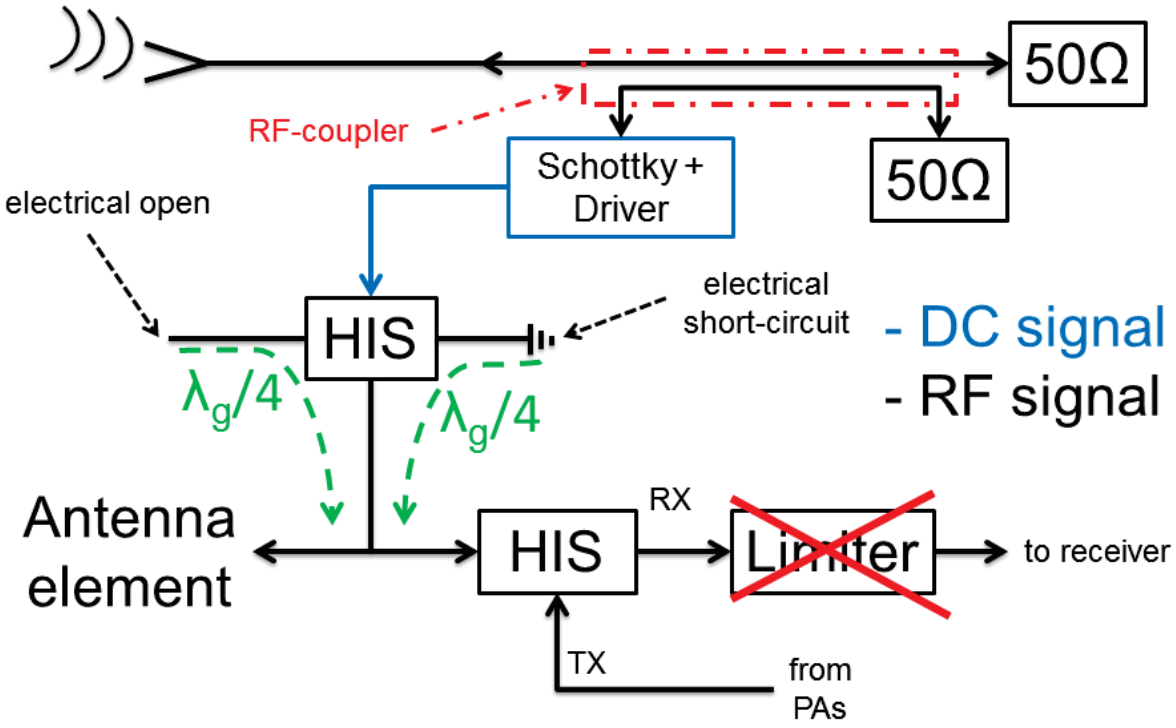


Figure 6.11: Receiver path with a novel active interference rejection mechanism. The implementation uses exclusively SMD COTS components and printed circuits.

6.4.2 Protector performance

In the previous paragraph a novel interference protection mechanism has been presented. There are no experimental results which can allow to analyse the protector performance. However, the most relevant issues are discussed in the following paragraphs.

The power at the diode detector (see Fig. 6.11) can be coupled from any of the dummy elements which are typically placed in the sides of phased-array antennas. This way, once the signal is converted by the driver to a digital standard (TTL, VCMOS, etc.), it can be easily routed to the rest of elements

in the array antenna. Furthermore, instead of routing the protector's control signal from the dummy elements, with the subsequent implementation effort, the output of the driver can be directly given to the main AESA antenna controller, which can then include this additional control signal in the logic of the T/R-module's command and control signals.

Another relevant topic is the reaction time of the receiver protector. The reaction time of a Schottky detector diode is typically in the order of $5 - 9$ ns. In addition, the presented switch is capable of changing its state in approximately 24 ns [71], which in combination with the (required) driver shown in Fig.6.11, gives a total reaction time in the range of $40 - 50$ ns. The main disadvantage of an active/quasi-active protection approaches is the overall reaction time, while, a passive technique such as a PIN-diode based limiter, gives its flat-leakage power in a few nanoseconds.

One option to improve the time response of this approach can be the integration of the power detector and the driver into the custom-made TRM-ICC, but this can improve the overall time marginally. Therefore, the feasibility of this novel protector is restricted to the maximum peak power supported by the switch in use, as well as the maximum survival (average and peak) power of the following stage (typically, an LNA), for an extension of time in the range of the protector's reaction time.

There are several reasons that motivate the use of the proposed protection circuit. The most relevant advantages are listed:

- Exclusively COTS components are used
- Full compatibility with standard planar and printed fabrication techniques
- Characterization of non-linear devices needs to be done only for the Schottky detector diode
- Extremely low leakage power
- The losses introduced in the receiver path are negligible
- Potential substitution of PIN-diode based limiters

Furthermore, in the case of highly interfered scenarios (such as in a harbour), the reaction and recovery time of the protector can be an advantage, since there are no electronics which are saturating. This means that the

recovery time of the circuitry depends exclusively on the reaction time of the circuit, without further effects, once the interference is vanished. Consequently, in the presence of several interfering sources, it can be expected a better performance in comparison to PIN-diode based solutions.

Finally, it can be argued that the overall circuit functionality is similar to the techniques that can be found in (e.g.) [96], [97], [98]. However, this receiver protector approach represents a novel contribution: the principle of operation and the implementation can be a breakthrough in protection techniques, since exclusively printed circuits, COTS and SMD components are involved in the design.

Chapter 7

Conclusions

This dissertation approached a series of scientific and technical challenges in fields related to phased-array antennas. The motivation and indirect goal of the work was to develop a functional S-band AESA antenna demonstrator, whose antenna ports are highly coupled, due to a novel RF feeding network with non-isolated ports. The solutions to be adopted required a compromise between functionality and costs by means of existing standard technologies, since the front-end is intended for civil radar applications. This combination of factors presents several issues, which have been solved in the frame of this thesis.

In the following sections, a summary and critical review of the thesis is given. In addition, an outlook of the next steps towards a fully functional S-band radar system are presented, together with the use of this novel phased-array architecture in other applications.

7.1 The novel AESA antenna concept

The novel AESA antenna architecture has been described with detail, and a representative demonstrator shows how the special feeding network, whose ports are non-isolated (resulting in highly coupled antenna ports), represent a significant contribution in the field of AESA antennas.

It can be of interest to study the behaviour of such a front-end with system simulation tools. However, it was chosen a more practical approach, since the theoretical results were very promising. This decision allowed to successfully solve the technical and scientific challenges, by means of the

manufactured demonstrator itself. In addition, the implementation of the front-end demonstrator was necessary, since the only manner to obtain scientific evidence of the functionality of such a challenging AESA antenna is by means of a demonstrator.

The development of some parts of the demonstrator were at moments complicated tasks, which require prolonged efforts. As an example, the most important part of the T/R-module (the SiGe core-circuit) is completely experimental, while, in order to keep the module's cost as low as possible, exclusively COTS components and standard existing technologies were used in the remaining parts of the module. This required an extra development effort, which lead to a plain and inexpensive T/R-module, when compared to existing modules of other AESA antennas. In addition, the inexpensive and plain module presented features with the sufficient performance for the intended application, and once a suitable receiver protector is included, it is perfectly suited for the use in a radar system. Similarly, the antenna aperture and the feeding network are realized by plain and inexpensive solutions, resulting in a front-end whose capabilities allow to improve civil navigation radar systems.

Furthermore, this special AESA antenna required an innovative solution for the implementation process. Every module has a different transition on the feeding network side. As a result of the feeding network design, the electrical range of the probe lengths is larger than a wave-length inside the network itself. This issue is addressed by means of a hollow-waveguide structure, which allows to test every T/R-module prior to its deployment into the front-end, with a minimum of manipulation. The same test-bed is used for every module, independently of the length of the probe of the feeding network transition.

7.2 Diagram synthesis

In the case of this demonstrator, the far-field radiation pattern can be measured easily, since its far-field distance is not very large. However, for the final functional S-band AESA antenna (with about 100 elements and more than six meters of length) the electrical size of the antenna makes infeasible to measure its radiation pattern in an anechoic chamber. For this reason, a near-field diagram synthesis is necessary.

The near-field diagram synthesis technique presented here introduces some advantages by means of a novel approach, since similar techniques in

an antenna with highly coupled ports and the particular aperture configuration have never been developed, to the author's knowledge. Following the method presented, electrically large antennas whose *very* near-field is difficult to measure can be calibrated in an easy manner.

In addition, a far-field beam-forming technique has been conducted. From a general point of view, the far-field diagram synthesis uses a rather common and plain principle. However, in order to use *regular* synthesis techniques, the calibration of the antenna is a key aspect. In this particular front-end, the antenna ports are highly coupled. This means that, the behaviour of every individual antenna element cannot be characterized (calibrated) without a strong influence of the other antenna elements. One approach can be to model this coupling, which can become a complicated task. Here, it has been presented a method which is based on the measurement of the four lowest gain states of the every active element in both antenna modes, transmit and receive.

The near-field based technique shown required a significant measurement time to complete the beam-forming, since it is performing an on-line optimization of the antenna, which relays on several measurements of the antenna's near-field. This is necessary because the calibration implemented was not sufficiently addressing the issues derived from the highly coupled antenna ports. However, the far-field approach developed can successfully counteract the effects of the non-isolated feeding network ports in the calibration process. Consequently, the antenna's radiation pattern needs to be measured only once. The modifications necessary to accommodate the far-field approach into the near-field calibration are plain, and the results can be expected to be very similar.

The excellent beam-forming results presented proof these synthesis and calibration approaches, which in addition is supported by ideal radiation pattern simulations, showing that the measured radiation patterns are almost reaching the ideal response of the antenna.

7.3 Receiver protection

It has been shown that the resented AESA antenna is rather sensitive to interferences. Several State-of-the-Art techniques can be considered, in order to give the necessary protection with a minimum impact in performance. Most of the solutions will increase marginally a *regular* phased-array's costs, since

the T/R-modules are worth, typically, several hundreds of euro. Consequently, typically T/R-modules dominate the front-end costs but the impact of the protection technique into the fabrication is negligible.

An interference sensitivity analysis of the manufactured antenna allowed to determine the protection techniques to be adopted. In the case of choosing State-of-the-Art solutions, the T/R-module cost are to be increased at least by a tenth, which makes the system infeasible for civil radar applications (as mentioned above, the modules represent a significant cost into a phased-array). This problem might be overcome with the novel solution proposed, since a qualitative performance analysis is very promising. However, the technique has not been practically demonstrated, and it has to be experimentally shown that it can be of use for the manufactured T/R-module.

7.4 Main achievements

The previous paragraphs presented a critical view of this thesis, including its weaknesses and its strongest points. Finally, the achievements of this work are summarized:

Achievement no. 1: The T/R-module solution developed is based on commercial-off-the-shelf components and in an inexpensive and highly integrated SiGe chip-set, dramatically decreasing the module costs and complexity, in comparison to State-of-the-Art circuitry

Achievement no. 2: A novel T/R-module test-bed has been developed. This task is particularly challenging, since the transitions on the feeding network side cover a large electrical range, but a structure with almost identical electrical properties needs to be used to perform the module evaluation. The test-bed presented allows to conduct the module test before its deployment in the array with minimum of manipulation and almost the same electrical properties, independently of the feeding network transition

Achievement no. 3: Innovative near-field and far-field calibration techniques have been developed in order to overcome the issues due to the electrical size, the radiating part configuration and the highly coupled ports of the AESA antenna

Achievement no. 4: The beam-forming results presented are almost reaching the best achievable antenna response (at the edge of the physical limits of the aperture), which is proven by means of comparison to ideal radiation pattern models

Achievement no. 5: In order to maintain the system costs low, State-of-the-Art receiver protection techniques cannot be used. An innovative protection mechanism concept is presented, which can allow to mitigate interferences effects using exclusively commercial-off-the-shelf components and inexpensive RF circuitry

Overall goal: Summarizing, this work proves the feasibility of an inexpensive, plain and compact AESA antenna, by means of innovative technological and scientific solutions, using current existing standard technologies.

7.5 Future work

The general point of view of this thesis is the approach to several scientific challenges, which are addressing the most relevant aspects of the implementation of an AESA antenna with highly coupled antenna ports. In particular, this work has been motivated by the need for a *low-cost* phased-array antenna, which can be use in a civil maritime navigation radar.

However, in order to allow the use of this active antenna in a navigation radar there are still several (scientific and technical) issues to be approached. The most significant ones are:

1. **Receiver protection:** A T/R-module receiver protection mechanism has been presented. It is necessary to conduct experimental measurements, in order to validate the proposed solution

2. **Installed performance of the AESA antenna:** Typically, the placement of antenna front-ends differs very much from the anechoic spaces were its radiation patterns are measured. For this reason, an strategy to guarantee the performance of the antenna once it is deployed is necessary. In the particular antenna architecture presented in this work, due to the special feeding network and the plain T/R-module, it is proposed to evaluate the installed performance of the antenna by measuring the coupling of the active elements with dummy elements, placed at the edges of the aperture. Such a technique may bring a novel performance evaluation of AESA antennas, whose consequence would be the reduction of the feeding network and T/R-module complexity

3. **Beam-forming:** It is shown that the SLL of the radiation pattern in receive mode cannot go below certain limits, due to the use of aperture

taper in such a small array. In addition, the beam-forming has been conducted at a single-frequency, since the performance is expected to be very similar within the S-band slot dedicated to maritime navigation. Further experiments with an AESA antenna formed by more elements may allow to verify these assumptions

4. **Signal integrity:** The manufactured demonstrator proves the beam-forming capabilities of the antenna, however, it is still necessary to evaluate parameters such as the performance of system operated by pulsed signals, the switching time (blind-distance) of the overall front-end or the immunity against other systems operating into the same frequency band. These are key aspects of navigation radar systems, and they need to be experimentally validated

In addition to the aspects closely related to a navigation radar, it can be also explored if the features of the front-end can be enhanced, which may allow the use of this antenna in different applications.

The first challenge that this architecture presents is the beam-forming instantaneous bandwidth, which is about 15 MHz. The bandwidth limitations of this AESA antenna concept are mostly consequence of the T/R-module and the series feeding network. It can be of interest to investigate AESA antenna operation techniques, which can deal with the special feeding network and increase the current beam-forming bandwidth. This may also require further work on the SiGe chip-set, in order to add more features to the current digital and analogue functionality. For instances, these investigations may allow to use this innovative phased-array architecture in airborne SAR systems.

Furthermore, the front-end channels are restricted to one, since the special feeding network operation forces the coherent sum of all antenna elements (simultaneously) at the common port of the network. However, by using similar concepts as in the calibration approach presented, it can be evaluated if the operation of individual or groups of elements is feasible. This can allow the use of this novel front-end concept in, e.g., MIMO systems.

The performance of this AESA antenna architecture is sufficient for navigation radar, but, there is still room to enhance the front-end capabilities while keeping a minimum architecture complexity. Therefore, this dissertation is not only a significant contribution to the application of phased-array antennas in civil navigation radar, but it also contributes to expand the use of phased-array technology to new fields.

List of Figures

1.1 Photograph of a Mammut radar station. The main-beam steering was performed with mechanical phase shifters. Source: http://www.radartutorial.eu, Creative-Commons license. . . . 2

1.2 Left: sketch of PESA antenna architecture. Right: AESA antenna architecture sketch with an exemplary T/R-module concept. 3

1.3 Example of X-band mechanically steered array antenna. Significant resource are dedicated to the installation. Source: Wikimedia Commons. 4

2.1 Generic AESA antenna scheme with a T/R-module example. . 14

2.2 Sketch of the proposed AESA antenna. The architecture concept allows to manufacture a compact, plain and inexpensive front-end. 15

2.3 Functional sketch of the proposed AESA antenna, showing the main signal paths in transmit and receive mode. 16

2.4 Generic front-end schematics. Taper realized by attenuators (left), and by attenuators and amplifiers (right). All the magnitudes are defined in power. The power contribution of every antenna branch to the common port is weighted by $1/M$. For the sake of clarity, the phase shifters are omitted in both sketches. 18

2.5 Dynamice range simulation results, for several SLLs (Taylor taper) and Q values. The results are normalized with respect to the absolute maximum (top) and the relative maximum of the SLL-row (bottom). 24

2.6 Radiation pattern simulation results. In transmit mode the SLL is −13 dB (top). In receive mode, aperture taper is applied in order to obtain a SLL of −30 dB (middle). The two-way radiation pattern meets the radiation pattern constraints (bottom). 27

3.1 Not-to-scale front-end cross-section. It can be seen the horn configuration, the feeding network and the location of the T/R-modules. 36

3.2 Representation of the far-field radiation planes. The E-plane is contained in $\theta = 0°$, $\Phi = [-90°, +90°]$. 37

3.3 Measured reflection coefficient of the active element no. 5, including transmission to successive neighbouring elements. The antenna demonstrator is formed by 10 radiating elements and 3 dummy elements on each side. 39

3.4 Calculated ARC of the active element no. 5 with respect to frequency and beam-scanning angle. The antenna demonstrator is formed by 10 radiating elements and 3 dummy elements on each side. 40

3.5 Full-wave simulation model of the realized feeding network. Port number one (right) refers to the common port. The element spacing is the same as determined in Chapter 2, which allows to full-fill the azimuth radiation constraints. 42

3.6 Measured taper coefficients against reference square-root of Taylor values. Maximum values are normalized to 1 (linear). . 43

3.7 T/R-module functional block diagram. DC-supply has been omitted. The TRM-ICC works as a common-leg structure with a variable gain LNA. 44

3.8 Top view photograph of the double-layer T/R-module PCB. All the RF lines are implemented in CPW or shielded microstrip. Apart from the TRM-ICC and the HIS, all the remaining elements are COTS components. 46

3.9 Measured T/R-module PGM at 3.0 GHz. In receive-mode (left) the linearity is preserved, while in the transmit-mode (right) saturation is present. 47

3.10 Snapshot of the initial transition (axial cut). The monopole's length is the same as in the real antenna. The distance to the short-circuit (upper wall on the image) is the same as in the PPW of the antenna demonstrator. 48

3.11 Photograph of the hollow waveguide test-bed interior, showing the aperture transition (left) and the TE_{10} steerer (right). . . 49

3.12 Photograph of the hollow waveguide test-bed interior, showing the feeding transition (left) and the TE_{10} steerer (right). . . . 50

3.13 Photograph of the hollow waveguide test-bed with the first T/R-module prototype installed. The T/R-module is interfaced with a HDMI cable. 51

3.14 Photographs of the back/left-side (top) and the front/left-side (bottom) of the manufactured ten element S-band AESA antenna. The antenna's power supply and the digital control unit of the modules are enclosed in the metallic space below the antenna. 55

4.1 Left: schematic of the near-field measurement set-up, side-view. The motor on the image moves the probe in perpendicular direction to the image plane. Right: photograph of the antenna demonstrator is shown. The FPGA which controls the antenna, the main power supply and the PCBs for signal distribution are enclosed in the box integrated below the front-end. 60

4.2 Sketch of the near-field calibration problem. It can be observed different magnitudes and parameters, which are used to establish a relation between the antenna weights and the near-field at the measurement plane. 63

4.3 Comparison of far-field radiation pattern in transmit (top) and receive (bottom), obtained by the implemented NF/FF transformation and from the full-wave solver direct solutions. . 68

4.4 Determination of best α' for the desired main-beam angle, based on the near-field antenna radiation model. 69

4.5 Comparison of normalized far-fields predicted by the near-field model and from measured near-fields, in transmit (top) and receive (bottom), for some exemplary angles. The model is not predicting properly the SLL, specially in the receive case, where more than 10 dB of deviation can be observed. However, successful predictions are obtained for the main-beam angle and the HPBW. 70

4.6 Sketch of the near-field measurement. The probe moves along the horizontal axis (x), measuring the vertical E-field contribution at each position. 73

4.7 Measured near-field amplitude distributions for different main-beam angles. 74

4.8 Required sampling line length depending on the main-beam angle and the maximum SLL error, transmit mode. 74

4.9 Prediction of far-field radiation based on extrapolated near-fields, receive-mode. On the left, the extrapolated near-fields are simulated. On the right, the near-field distributions are directly measured. In both cases, the far-fields are obtained by the shown NF/FF transformation. 78

4.10 Near-field calibration process concept. This measurement routine allows to obtain the relation of the near-field produced at the aperture and any arbitrary antenna excitation. 79

4.11 Representation of undesired effects on the calibration, due to the highly coupled RF ports of the feeding network, in receive mode. In this case, the input signal is at port number 2. Multiple interactions are not considered. 80

4.12 Simulated transmissions to the common port for several different *passivated* T/R-modules' reflection coefficients. The ideal values are shown for a better comparison (*Orig*). 82

4.13 Simulated transmissions to the common port for several different *passivated* T/R-modules' residual gains. The ideal values are shown for a better comparison (*Orig*). 83

5.1 Optimization routine to enhance the LMS antenna weights obtained by the near-field antenna model. Some steps are omitted for the sake of simplicity. 87

5.2 Predicted transmit (top) and receive (bottom) far-field radiation patterns, for main-beam directions of $-10°$ and $+20°$ with respect to broad side, respectively. Antenna weights obtained by LMS and after post-optimization. 88
5.3 Photograph of the AESA antenna mounted on the turning table. The reference antenna is static (not shown). The array of monopoles can be observed inside the aperture. Only three cables are necessary to interface the front-end: power supply, RS-232 and RF. 89
5.4 Measured transmit (top) and receive (bottom) far-field radiation patterns, for main-beam directions of $+20°$ and $0°$ with respect to broad side, respectively. The far-field predicted by the NF/FF transformation is included for better comparison. Post-optimized antenna weights. 90
5.5 Far-field calibration process based on far-field measurements. . 92
5.6 Directly measured embedded element patterns, receive mode. It is not expected such an asymmetric behaviour. 92
5.7 Measured passive pattern in receive mode while the active antenna is *passivated*. This is an expected result, but not the order of magnitude, which is comparable to the single element patterns. 93
5.8 Compensated embedded element patterns, receive mode. The far-field of the element patterns are smother, and the behaviour is in general more symmetric. The edge effects of such an small array can justify the observed results. 94
5.9 Beam-forming method based on far-field measurements. 96
5.10 Directly measured transmit (top) and receive (bottom) radiation patterns for several main-beam angles. Original antenna weights (non-optimized). 96
5.11 Far field off-line optimization sketch. 97
5.12 Directly measured transmit (top) and receive (bottom) radiation patterns for several main-beam angles. Antenna weights optimized off-line. 99
5.13 Comparison of measured and simulated radiation patterns for different main-beam angles. The SLLs of the measured far-fields are comparable to the reference patterns. 101
5.14 Antenna model, based on concatenation of scattering parameters (left) and back-propagated waves (right). 104

5.15 Comparison of simulated and measured radiation patterns, showing the influence of the T/R-module's reflection coefficient on the SLL. 107

6.1 Scheme of the interference sensitivity experiment, showing the CW interferer concept (left), and the complete experimental set-up (top view, right). The interferer is placed at approximately 10° to the left of the AESA antenna. 112

6.2 Photograph of the interference experimental set-up. The three main elements of the experiment can be seen: the main illumination, the interferer and the S-band AESA demonstrator. . 113

6.3 Simulation results of the estimated RF power received by every T/R-module, Prx_{module}. The power of the generator, P_{gen}, is set to 0 dBm. The gain of the demonstrator's antenna element is obtained from full-wave simulations, $G_{element}$. The response of the rest of the components is obtained from either datasheets or measurements. 113

6.4 Radiation patterns in RX-mode showing the degradation on the main-lobe and the SLL (middle and bottom), depending on the frequency of the CW interference. For better comparison, the original pattern with and without the second illumination in the chamber are depicted in green (*Original*) and red (*InterfOFF*), respectively. 116

6.5 Radiation patterns in RX-mode demonstrating the excitation of TRM-ICC harmonics. For better comparison, the original pattern with and without the second illumination in the chamber are depicted in green (*Original*) and red (*InterfOFF*), respectively. 117

6.6 Radiation patterns in TX-mode showing no influence of the interferences, demonstrating the immunity of the front-end in transmit mode. For better comparison, the original radiation patterns with and without the second illumination in the chamber are depicted in green (*Original*) and red (*InterfOFF*), respectively. 118

6.7 Basic receiver path, including the proposed elemental receiver protection. On the top for a generic case, at the bottom for the considered S-band AESA antenna. 119

6.8 Receiver path with elemental receiver protection and a shunt-stub in the input port, immediately in front of the switch. The short-circuit at the end of the shunt-stub is translated into an open at the feeding point, in the RF input line. Therefore, the effect of the shunt-stub is negligible at the adjusted frequency. 121
6.9 High isolation switch offering an electrical open or an electrical short, depending on the control signal. 121
6.10 High isolation switch offering an electrical open or an electrical short, depending on the power detected by a Schottky detector diode. 122
6.11 Receiver path with a novel active interference rejection mechanism. The implementation uses exclusively SMD COTS components and printed circuits. 123

List of Tables

2.1 Front-end parameters 23
2.2 Antenna radiation pattern constraints 26
2.3 Noise figure parameters, F_T 30
2.4 Front-end losses (L_f) 30
2.5 System parameters 31

3.1 Test-bed validation with passive PCBs, f_c=3.0 GHz 52

6.1 Selected interference frequencies 111

Bibliography

[1] H. Hertz, *"Electric Waves"*. New York: Dover Publications, 1893.

[2] O. E. Dunlap, *"Marconi: the man and his wireless"*. Newcastle: Cambridge Scholars Publishing, 2010.

[3] S. Uda, "High angle radiation of short electric waves," in *Proceedings of the IRE*, vol. 15, May 1927, pp. 377–385.

[4] D. T. Emerson, "The work of Jagadis Chandra Bose: 100 years of MM-wave research," in *IEEE MTT-S International Microwave Symposium Digest*, vol. 2, Denver, CO, USA, 1997, pp. 553–556.

[5] R. C. Hansen, *"Microwave Scanning Antenna, Volume I Apertures"*. New York: Academic Press, Inc., 1964.

[6] ——, *"Microwave Scanning Antenna, Volume II Array Theory and Practice"*. New York: Academic Press, Inc., 1966.

[7] ——, *"Microwave Scanning Antenna, Volume III Array Systems"*. New York: Academic Press, Inc., 1966.

[8] S. S. Swords, *"Technical History of the Beginnings of Radar"*. London: Peter Peregrinus, 1996.

[9] A. Agrawal, R. Clark and J. Komiak, "T/R module Architecture Tradeoffs for Phased Array Antennas," in *IEEE MTT-S International Symposium*, San Francisco, CA, USA, Jan. 1996, pp. 995–998.

[10] L. Stark, "Microwave Theory of Phased-Array Antennas - A Review," in *Proceedings of the IEEE*, vol. 62, December 1974, pp. 1661–1701.

[11] L. I. Parad and R. L. Moynihan, "Split Tee Power Divider," *IEEE Transactions on Microwave Theory and Techniques*, vol. 13, pp. 91–95, Jan. 1965.

[12] E. J. Wilkinson, "An N-Way Hybrid Power Divider," *IRE Transactions on Microwave Theory and Techniques*, vol. 8, pp. 116–118, Jan. 1960.

[13] B. Lax, K. J. Button and L. M. Roth, "Ferrite Phase Shifters in Rectangular Wave Guide," *Journal of Applied Physics*, vol. 25, pp. 1413–1421, Nov. 1954.

[14] F. Reggia and G. Spencer, "A New Technique in Ferrite Phase Shifting for Beam Scanning of Microwave Antennas," in *Proceeding of the IRE*, vol. 45, November 1957, pp. 1510–1517.

[15] J. F. Whiter, "High Power, p-i-n Diode Controlled, Microwave Transmission Phase Shifters," *IEEE Transactions on Microwave Theory and Techniques*, vol. 13, pp. 233–242, March 1965.

[16] R. V. Garver, "Broad-Band Diode Phase Shifters," *IEEE Transactions on Microwave Theory and Techniques*, vol. 20, pp. 314–323, May 1972.

[17] C. A. Baird and G. G. Rassweiler, "Adaptive Sidelobe Nulling Using Digitally Controlled Phase-Shifters," *IEEE Transactions on Antennas and Propagation*, vol. 24, pp. 638–649, Sept. 1976.

[18] L. G. Josefsson, "Adaptive Sidelobe Nulling Using Digitally Controlled Phase-Shifters," in *2nd European Microwave Conference*, Aug. 1971, pp. 1–4.

[19] N. Goto and D. Cheng, "Sidelobe-reduction techniques for phased arrays using digital phase shifters," *IEE Proceedings on Communications, Radar and Signal Processing*, vol. 18, pp. 769 – 773, Nov. 1970.

[20] P. Barton, "Digital beam forming for radar," *IEE Proceedings on Communications, Radar and Signal Processing*, vol. 127, pp. 266–277, Aug. 1980.

[21] D. Borgmann, "An experimental array-antenna with digital beamforming for advanced radar applications," in *Antennas and Propagation Society International Symposium*, May 1982, pp. 431–434.

[22] K. W. Chang, G. S. Dow, H. Wang, T. N. Chen, K. Tan, B. Allen, I. Berenz, J. Wehling and R. Lin, "A W-band single-chip transceiver for FMCW radar," in *Microwave and Millimeter-Wave Monolithic Circuits Symposium Digest*, Atlanta, GA, USA, June 1993, pp. 41–44.

[23] M. D. Pollman, P. Katzin, B. Bedard, V. Aparin, W. Grammer and R. Orgusaar, "A MMIC radar chip for use in air-to-air missile fuzing applications," in *IEEE MTT-S International Microwave Symposium Digest*, San Francisco, GC, USA, June 1996, pp. 185–188.

[24] B. A. Kopp, M. Borkowski and G. Jerinic, "Transmit/Receive Modules," *IEEE Transactions on Microwave Theory and Techniques*, vol. 50, pp. 827–834, March 2002.

[25] Y. Mancuso, P. Gremilleta and P. Lacomme, "T/R-Modules Technological and Technical Trends for Phased Array Antennas," in *IEEE MTT-S International Microwave Symposium Digest*, San Francisco, CA, USA, June 2006, pp. 614–617.

[26] T. Boles, D. J. Carlson and C. Weigand, "MMIC Based Phased Array Radar T/R Modules," in *IEEE International Conference on Microwaves, Communications, Antennas and Electronics Systems (COMCAS)*, Nov. 2011, pp. 1–4.

[27] T. Dinc, S. Zihir and Y. Gurbuz, "SiGe Building Blocks for On-Chip X-Band T/R Modules," in *IEEE 12th Tropical Meeting on Silicon Monolithic Integrated Circuits in RF Systems (SiRF)*, Santa Clara, CA, Jan. 2012, pp. 57–60.

[28] M. I. Skolnik, *"Radar Handbook"*. New York: McGrawll-Hill, 2008.

[29] International Electrotechnical Commission, "IEC 62388 Ed. 1: Maritime navigation and radio-communication equipment and systems – shipborne radar – performance requirements, methods of testing and required test results," 2007.

[30] BONN Elektronik GmbH, "Solid-state RF power amplifiers," 2013.

[31] B. Wade, "SharpEye A New Technology marine radar," in *IET International Conference on Radar Systems*, Edinburgh, UK, Oct. 2007, pp. 1–5.

[32] R. J. Mailloux, *"Phased Array Antenna Handbook"*. Norwood: Artech House, Inc., 1994.

[33] C. Loecker, M. Pamies, T. Bertuch, P. Knott, H. Erkens, R. Wunderlich and S. Heinen, "Antenna front-end concepts of a low-cost coherent radar demonstrator for S-band application," in *Proceedings of the Fourth European Conference on Antennas and Propagation (EuCAP)*, Barcelona, Spain, April 2010, pp. 1–5.

[34] T. Bertuch, M. Pamies, C. Loecker, P. Knott, H. Erkens, R. Wunderlich and S. Heinen, "System aspects of a low-cost coherent radar system with AESA antenna for maritime applications," in *International Kharkov Symposium on Physics and Engineering of Microwaves, Millimeter and Submillimeter Waves (MSMW)*, Kharkiv, Ukraine, June 2010, pp. 1–6.

[35] F. E. van Vliet and A. de Boer, "Fully-integrated core chip for X-band phased array T/R-modules," in *IEEE MTT-S International Microwave Symposium Digest*, vol. 3, June 2004, pp. 1753–1756.

[36] M. van Heijningen, A. de Boer, J. A. Hoogland, M. van Wanum, A. P. de Hek, F. E. van Vliet and H. Brouzes, "Multi Function and High Power Amplifier Chipset for X-Band Phased Array Frontends," in *The 1st European Microwave Integrated Circuits Conference*, Manchester, UK, Sept. 2006, pp. 237–240.

[37] H. Erkens, R. Wunderlich and S. Heinen, "A low-cost, high resolution, 360° Phase/gain shifter in SiGe BiCMOS," in *IEEE Topical Meeting on Silicon Monolithic Integrated Circuits in RF Systems*, Jan. 2009, pp. 1–4.

[38] ——, "A Novel SiGe RFIC Approach Towards Low-Cost S-Band Transmit/Receive Modules," in *IEEE Radar Conference*, Pasadena, USA, May 2009, pp. 1–4.

[39] ——, "A Double Balanced Power Amplifier for S-Band Phased Arrays in SiGe BiCMOS," in *European Solid State Circuits Conference*, Athens, Greece, Sept. 2009, pp. 180–183.

[40] H. Erkens, *"Analysis and Design of SiGe BiCMOS Integrated Circuits for Commercial Maritime Phased Array Radar Systems"*. Munich: Dr. Hut, 2010.

[41] S. Zihir, T. Dinc and Y. Gurbuz, "Compact X-band SiGe power amplifier for single-chip phased array radar applications," *IET Microwaves, Antennas and Propagation*, vol. 6, pp. 956–961, March 2012.

[42] R. J. Mailloux, "Antenna Array Architecture," in *Proceedings of the IEEE*, vol. 80, Jan. 1992, pp. 163–172.

[43] A. K. Agrawal and E. L. Hozman, "Beamformer Architectures for Active Phased-Array Radar Antennas," *IEEE Transactions on Antennas and Propagation*, vol. 47, pp. 432–442, March 1999.

[44] D. Parker and D. C. Zimmermann, "Phased Arrays - Part I: Theory and Architectures," *IEEE Transactions on Antennas and Propagation*, vol. 50, pp. 678–687, March 2002.

[45] ——, "Phased Arrays - Part II: Implementations, applications and future trends," *IEEE Transactions on Antennas and Propagation*, vol. 50, pp. 688–698, March 2002.

[46] R. S. Elliot, *"Antenna Theory and Design"*. New Jersey: Prentice Hall, Inc., 2003.

[47] T. Bertuch, "Patent. DE102007037252," Aug. 2007.

[48] H. J. Visser, *"Array and Phased Array Antenna Basics"*. New Jersey: John Wiley and Sons, Ltd., 2005.

[49] N. Amitay, V. Galindo and C. P. Wu, *Theory and Analysis of Phased Array Antennas*. New York: Wiley-Interscience, 1972.

[50] C. Mertzianidis, I. Diamandi, J. N. Sahalos, "A voltage-matching method for feeding antenna arrays," *IEEE Transactions on Broadcasting*, vol. 38, pp. 27–32, March 1992.

[51] N. E. Stabolidis, E. E. Vafiadis, J. N. Sahalos, "A study of the isolation of two different feed networks for antenna arrays," *IEEE Transactions on Antennas and Propagation*, vol. 41, pp. 83–88, June 1995.

[52] J. L. Volakis, *"Antenna Engineering Handbook"*. New York: McGraw-Hill, 2007.

[53] E. L. Holzman and Ashok K. Agrawal, "A comparison of active phased array, corporate beamforming architectures," in *IEEE International Symposium on Phased Array Systems and Technology*, Oct. 1996, pp. 429–434.

[54] R. V. Gatti, M. Dionigi and R. Sorrentino, "Computation of Gain, Noise Figure, and Third-Order Intercept of Active Array Antennas," *IEEE Transactions on Antennas and Propagation*, vol. 52, pp. 3139–3143, Nov. 2004.

[55] D. M. Pozar, *"Microwave Engineering"*. Boston: Addison-Wesley, 1990.

[56] T. T. Taylor, "Design of line-source antennas for narrow beamwidth and low side lobes," *Transactions of the IRE Professional Group on Antennas and Propagation*, vol. 3, pp. 16–28, Jan. 1955.

[57] D. M. Pozar, "The Active Element Pattern," *IEEE Transactions on Antennas and Propagation*, vol. 42, pp. 1176–1178, Aug. 1994.

[58] Y. T. Lo and S. W. Lee, *Antenna Handbook. Vol. II.* New York: Van Nostrand Reinhold, 2005.

[59] M. I. Skolnik, *"Introduction to Radar Systems"*. New York: McGraw-Hill, 1980.

[60] G. G. Guerrero-Guerra, "System Design of Novel Navigation Radar Demonstrator Back-end," Fraunhofer FHR, 2011.

[61] E. Brookner, *"Practical Phased-Array Antenna Systems"*. Norwood: Artech House, 1991.

[62] C. A. Balanis, *"Antena Theory, Analysis and Design"*. New Jersey: Wiley-Interscience, 2005.

[63] L. K. Lam, W. S. Gregorwich and S. A. Horn, "S-band electronically scanned active phased array antenna," in *IEEE Aerospace Conference Proceedings*, vol. 5, Big Sky, MT, USA, March 2000, pp. 67–72.

[64] J. Cholewa, B. Stachowski, A. Czwartacka, K. Szustak, D. Startek, M. Andrzejewski, R. Sender and T. Lorens, "An active antenna demonstrator for future AESA-systems," in *IEEE International Radar Conference*, May 2005, pp. 226–231.

[65] ——, "Demonstrator of S band active antenna with T/R-modules," in *11th International Radar Symposium (IRS)*, Vilnius, Lithuania, June 2010, pp. 1–4.

[66] B. Tomasic and A. Hessel, "Linear Array of Coaxially Fed Monopole Elements in a Parallel Plate Waveguide-Part I: Theroy," *IEEE Transactions on Antennas and Propagation*, vol. 36, pp. 449–462, April 1988.

[67] ——, "Linear Array of Coaxially Fed Monopole Elements in a Parallel Plate Waveguide-Part II: Experiment," *IEEE Transactions on Antennas and Propagation*, vol. 36, pp. 463–467, April 1988.

[68] P. W. Hannan, "The Element-Gain Paradox for a Phased-Array Antenna," *IEEE Transactions on Antennas and Propagation*, vol. 12, pp. 423–433, July 1964.

[69] D. M. Pozar, "A Relation Between the Active Input Impedance and the Active Element Pattern of a Phased Array," *IEEE Transactions on Antennas and Propagation*, vol. 51, pp. 2486–2489, Sept. 2003.

[70] W. L. Stutzman and G. A. Thiele, *Antenna Theroy and Design.* New York: John Wiley and Sons Inc., 1998.

[71] *SPDT High Isolation Terminated Switch 0.5 - 3.0 GHz, MASWSS0121*, M/A-COM Technology Solutions Inc.

[72] *RF Amplifier 802.11G PA, TQP777002*, TriQuint Semiconductor, Inc.

[73] *RF Driver Amplifier, 250 - 4000 MHz, MAAM-009286*, M/A-COM Technology Solutions Inc.

[74] *400 MHz to 4000 MHz 1/2 Watt RF Driver Amplifier*, Analog Devices, Inc.

[75] *1/2 W High Linearity InGaP HBT Amplifier, AH125*, TriQuint Semiconductor, Inc.

[76] W. W. Mumford, "The Optimum Piston Position for Wide-Band Coaxial-to-Waveguide Transducers," in *Proceedings of the IRE*, vol. 41, February 1953, pp. 256–261.

[77] M. Jäger, "Personal communication," Fraunhofer FHR, 2011.

[78] R. Shavit and S. Levy, "Improved Orchard-Elliott pattern synthesis algorithm by pseudo inverse and LMS," in *21st convention of the electrical and electronic engineers*, Israel, Tel-Aviv, 2000.

[79] P. H. Knott, *"Antenna Modelling and Pattern Synthesis Method for Conformal Array System Analysis"*. Aachen: RWTH-Aachen, 2002.

[80] J. E. Hudson, *"Adaptive array principles, IEE Electromagnetic Waves Series"*. London: Peter Peregrinus Ltd., 1981.

[81] R. A. Monzingo and T. W. Miller, *"Introduction to Adaptive Arrays"*. New Jersey: John Wiley and Sons, Inc., 1980.

[82] *Captor-E AESA radar*, Eurofighter Jagdflugzeug GmbH.

[83] S. Gregson, J. McCormick and C. Parini, *"Principles of Planar Near-Field Antenna Measurements"*. Stevenage: The Institution of Engineering and Technology, 2007.

[84] W. M. Leach, Jr., E. B. Joy and D. T. Paris, "Probe compensated Near-Field measurements: basic theory, numerical techniques, accuracy," in *IEEE Antennas and Propagation Society International Symposium*, June 1974, pp. 155–157.

[85] T. B. Hansen and D. Yaghjian, "Formulation of probe-corrected planar Near-Field scanning in the time domain," *IEEE Transactions on Antennas and Propagation*, vol. 43, pp. 569–584, June 1995.

[86] ——, "Planar Near-Field Scanning in the Time Domain, Part 1: Formulation," *IEEE Transactions on Antennas and Propagation*, vol. 42, pp. 1280–1291, Sept. 1994.

[87] ——, "Planar Near-Field Scanning in the Time Domain, Part 2: Sampling Theorems and Computation Schemes," *IEEE Transactions on Antennas and Propagation*, vol. 42, pp. 1292–1300, Sept. 1994.

[88] T. B. Hansen and A. D. Yaghjian, "Formulation of time-domain planar near-field measurements without probe correction," Rome Laboratory, Air Force Materiel Command, Griffiss Air Force Base, New York, 1993.

[89] D. M. Kerns, "Plane-Wave Scattering-Matrix Theory of Antennas and Antenna-Antenna Interactions: Formulation and Applications," *Journal of Research of the National Bureau of Standards - B. Mathematical Sciences*, vol. 80B, pp. 5–51, January- March 1976.

[90] T.B. Hansen and A.D. Yaghjian, *"Plane-Wave Theory of Time-Domain Fields. Near-Field Scanning applications.* New York: Institute of Electrical and Electronics Engineers, Inc., 1999.

[91] O. M. Bucci, G. D'Elta, G. Mazzarella and G. Panariello, "Antenna Pattern Synthesis: A New General Approach." in *Proceedings of the IEEE*, vol. 82, March 1994, pp. 358–371.

[92] T. Bertuch, P. Knott, H. Wilden and O. Peters, "Wide-Band Radar Front-End Calibration for Imaging SAR experiments with Conformal Antenna Array," in *Proceedings of the 5th European Conference on Antennas and Propagation (EUCAP)*, Rome, Italy, April 2011, pp. 2610–2614.

[93] M. S. Smith and Y. C. Guo, "A comparison of methods for randomizing phase quantization errors in phased arrays," *IEEE Transactions on Antennas and Propagation*, vol. 31, pp. 821–828, Nov. 1983.

[94] U.S. Department of Commerce, "National telecommunications and information administration office of spectrum management," 2003.

[95] H. Erkens, "Personal communication," RWTH-Aachen, 2010.

[96] B. K. Sarkar, "Comparison of Degradations in Radar System Sensitivities Due to TW Tube and TR Limiter ," *IEEE Transactions on Electronic Devices*, vol. 29, pp. 931–932, May 1982.

[97] Subcommittee on TR and ATR Tubes, "IRE Standards on Electron Tubes: TR and ATR Tube Definitions," in *Proceedings of the IRE*, vol. 41, Aug. 1956, pp. 1037–1039.

[98] B. M. Coaker, D. M. Dowthwaite and N. E. Priestley, "High-Power Multi-Function Radar Receiver Protection," in *3rd European Radar Conference*, Manchester, UK, Sept. 2006, pp. 253–256.

[99] N. J. Brown, "Design Concepts for High-Power PIN Diode Limiting," *IEEE Transactions on Microwave Theory and Techniques*, vol. 15, pp. 732–742, December 1967.

[100] E. C. Niehenke, P. A. Stenger, and J. E. Degenford, "A GaAs MMIC PIN diode receiver protector with switchable attenuator," in *IEEE MTT-S International Symposium*, San Francisco, CA, USA, June 1996, pp. 1589–1592.

[101] S. Yang, T. Kim, D. Kong, S. Kim, and K. Yeom, "A Novel Analysis of a Ku -Band Planar p-i-n Diode Limiter," *IEEE Transactions on Microwave Theory and Techniques*, vol. 57, pp. 1447–1460, June 2009.

[102] B. M. Coaker and D. M. Dowthwaite, "Planar limiters and receiver protectors," in *European Radar Conference*, Munich, Germany, Oct. 2007, pp. 405–408.

[103] G. Morris, V. Higgins, G. Hall, Y. Anand, R. Bilotta and F. Jellison, "Self activated, 20 kW X-Band Bulk Effect Semiconductor Limiter," in *IEEE MTT-S International Symposium*, Orlando, FL, USA, April-May 1979, pp. 243–248.

[104] R. Keenan and E. Higham, "X-band receiver protector using glass technology," in *IEEE MTT-S International Symposium*, Orlando, FL, USA, May 1995, pp. 1103–1106.

[105] D. Strack and F. Harris, "Low cost microwave receiver protectors/AGC's using surface mount components," in *IEEE MTT-S International Symposium*, Denver, CO, USA, June 1997, pp. 531–534.

[106] *Packaged PIN Diodes*, M/A-COM Technology Solutions Inc.

[107] D. Davies, "Shifting boundaries," *Electronics Letters*, vol. 48, p. 1439, November 2012.

[108] *Schottky Detector Diodes*, M/A-COM Technology Solutions Inc.

The objective of this work is the development of an Active Electronically Scanned Array (AESA) antenna demonstrator for civil maritime radar. AESA technology has been applied in a wide range of fields; however, it has been restricted to high-end and military markets, mostly because of its high overall costs.

This research aims to fulfil regulatory requirements of civil maritime radar at reduced cost. An AESA antenna whose single active antenna element supports mixed signal operation (analogue and digital) allows to solve the additional challenges imposed by this regulation. Moreover, an innovative RF feeding network operation and a plain antenna aperture concept are proposed.

The array can be produced with an inexpensive extrusion process, resembling existing navigation radar antennas. The RF feeding network lacks any isolation between its ports.

The similarity between simulated beam-forming and the measured patterns show that ideal performance is almost achieved. In addition, the pattern sensitivity to interferences is analysed, and inexpensive protection solutions are proposed.

In summary, this work shows how phased-array technology can be open to further fields of applications.

ISBN 978-3-8396-1219-4

